Innovations in Fixed-Target Serial X-ray Crystallography

By

DEEPSHIKA SHAMRAJ GILBILE
DISSERTATION

Submitted in partial satisfaction of the requirements for the degree of

DOCTOR OF PHILOSOPHY

in

Chemical Engineering

in the

OFFICE OF GRADUATE STUDIES

of the

UNIVERSITY OF CALIFORNIA

DAVIS

Approved:

_____

Prof. Tonya L. Kuhl, Chair

_____

Prof. Marjorie L. Longo

_____

Dr. Matthew A. Coleman

_____

Prof. Volkmar Heinrich

Committee in Charge
2021

This work is dedicated to my loving parents, Mrs. Babita and Mr. Shamraj Gilbile. Without their hard work, sacrifices, and unwavering love and support, I would not be here today.

ACKNOWLEDGEMENTS

First and foremost, I would like to thank Prof. Tonya Kuhl for giving me the opportunity to work on this project. Her scientific expertise, optimistic spirit, and her kind and nurturing mentorship style were invaluable to me during my graduate studies. I would like to thank my collaborators Dr. Megan Shelby, Dr. Matthew Coleman, and Dr. Matthias Frank who I worked with closely over the years, for their guidance and support on the XFEL project. I would also like to thank Prof. Marjorie Longo and Prof. Volkmar Heinrich for helpful conversations through the years and for serving on my dissertation committee. I had a great experience learning from all the professors in the Chemical Engineering department at UC Davis. Additionally, participating in the DEB program allowed me to explore more areas of research within Biotechnology, both through coursework and an industry internship. Thank you, Dr. Judy Kjelstrom and Dr. Denneal Jamison-McClung for accepting me into the DEB program.

Next, I would like to acknowledge all my friends and colleagues in the Kuhl lab, Dr. Amanda Dang, Michael Bull, Tanner Finney, Evan Haning, Ryan Edmonds, and Zhongrui Liu, for creating an inclusive and fun work environment. Moving to a new country to pursue graduate studies was a huge life change, and I found it quite difficult to adjust in the beginning. Thanks to Amanda and Mike it got a lot easier once I joined the Kuhl lab. I'm also grateful for the love and support of all the friends I made in Davis over the last five years, especially Dr. Shivani Bansal, Dr. Sukriti Gakhar, Saheli Chatterjee, Nitin Sai Beesabathuni, Meghna Jha, and Swati Sundar. All of you are awesome people and scientists who continue to inspire me. I'm also thankful for my long-distance friends, my best friend Nikitha Reddy for making the Bay Area a home away from home, Veena Vallem for always being my hype-girl and cheerleader, and Chandrahas Tanguturi for always making time for me despite being in the opposite time zone.

This graduate journey would not have been possible if not for the unconditional love and support of my parents, Babita and Shamraj Gilbile, and my brother Shreyansh Gilbile. A special thank you to my aunt, Meenakshi Goti for being a loving third parent throughout my life. Thank you all for allowing me to pursue my dreams even if that meant sending me to the opposite side of the planet, for always believing in me, and for encouraging me to aim for the best.

Last but not the least, I want to thank my partner, Sumedh Parab. You have been my rock for the last six years of my life, from the point when I was just considering applying to grad school to now when I am close to graduating with a doctorate. You inspire me, motivate me, and believe in me more than I do myself, and for that I will always be grateful.

DISSERTATION ABSTRACT

Innovations in Fixed-Target Serial X-ray Crystallography

Over the last decade, brilliant, coherent femtosecond X-ray free-electron lasers (XFELs) have revolutionized structural biology by enabling ultrafast, room-temperature (RT) protein structure and dynamics studies. Using a diffract-before-destroy approach, even weakly-diffracting micro or nanocrystals of hard-to-crystallize proteins can be studied using multi-crystal or "serial" data collection. But challenges exist in efficiently delivering hundreds to thousands of crystals to the X-ray beam while maintaining crystal integrity and maximizing signal-to-noise in ambient or vacuum environments. Microfabricated fixed-target supports are an exciting alternative to widely used liquid jet-based technologies as they offer distinct advantages like clog-free delivery, significantly lower sample consumption, control over sample distribution, and the ability to incorporate stimuli like ligands, caged reactants, or electric fields "on-chip" for dynamic time-resolved experiments.

The works compiled in this dissertation focus on the development of two fixed-target sample delivery devices, (1) silicon micropatterned grids with ultra-thin graphene-polymer enclosing layers for structural characterization of weakly-diffracting, two-dimensional (2D) nanocrystals, or three-dimensional (3D) microcrystals where background scatter from the device can limit diffraction resolution attained, and (2) polymer microfluidic chips that enable direct on-chip crystallization and stable, long-term storage, for plug-and-play *in situ* diffraction measurements. Experiments on model proteins were used to benchmark the performance of these devices to demonstrate high-resolution data collection, paving the way for reliable, user-friendly protein structure studies on more scientifically interesting targets in the future.

TABLE OF CONTENTS

CHAPTER 1:INTRODUCTION

1.1 Macromolecular X-ray Crystallography: Challenges and Opportunities

X-ray crystallography is the workhorse of structural biology, accounting for more than 85% of all macromolecular structures deposited in the Protein Data Bank (www.rcsb.org, October 2021).[1] The requirement for large, well-ordered crystals, however, remains a major bottleneck in the field, with most proteins screened for crystallization conditions producing only microcrystals (< 10 μm, in one or more dimensions), if they crystallize at all.[2,3] Laborious optimization of crystallization conditions can sometimes yield larger crystals, but most proteins prove intractable, making handling and characterization using traditional cryogenic single crystal measurements impossible. This challenge has motivated the development of new microfocus X-ray beamlines with orders of magnitude higher brilliance (photon flux), capable of characterizing ever smaller crystals.[4,5] The last decade has seen the emergence of X-ray free electron lasers (XFELs), capable of producing femtosecond X-ray pulses at high-repetition rates (120 Hz – 1 MHz) that can outrun radiation damage to collect diffraction patterns from crystals <1-3 μm in size, paving the way for room-temperature (RT) protein structure and dynamics studies.[6–11]

The high intensity of these beamlines, fast onset of radiation damage at RT, and the use of microcrystals limit the number of high-resolution diffraction frames that can be collected from a single crystal. To address this limitation, serial crystallography (SX) can be used, where data from multiple crystals (hundreds to thousands) is combined to produce a structure.[12–15] This method requires a much larger amount of crystalline material than conventional crystallography, necessitating the development of specialized crystal delivery methods which are continuous, robust, and keep the crystals hydrated over the course of the measurement.

The works compiled in this dissertation focus on the development of fixed-target devices or solid supports which can be translated and/or tilted orthogonal to the X-ray beam to collect diffraction data from multiple crystals.[16,17] These offer an exciting alternative to widely-adopted liquid jet-based methods because they (1) require very low sample volumes, (2) are compatible with *in situ* crystal growth which eliminates crystal handling, (3) enable tuning of crystal densities and sizes to achieve high hit rates and high-quality diffraction images, (4) allow for the use of non-jetable crystal morphologies, like needles or plates, or crystals of heterogeneous size, and (5) can also be used to facilitate dynamic experiments using stimuli like electric fields gradients, temperature jumps, pH gradients, ligand exchange and photo-activation.

Chapter 2 focuses on developing methods to encapsulate biological samples using polymer thin films and graphene on micropatterned silicon grids to maintain sample hydration in vacuum conditions, towards our goal of enabling low-background measurements on weakly diffracting samples. This approach is benchmarked using microcrystals of radiation-sensitive 24 kDa rapid encystment protein (REP24) and tested for the characterization of nanoscale (5-10 nm thick) 2-D protein crystals in model lipid membranes, taking a step towards membrane protein structure characterization in native-like lipid environments. Given the challenges of working with expensive and fragile silicon and graphene-based methods, Chapter 3 focuses on the development of low-cost, user-friendly, polymer-based microfluidic chips that enable on-chip protein crystallization, monitoring, long-term storage, and direct *in situ* X-ray diffraction measurements. The modular chip design enables precise control of materials in the X-ray cross section by tuning enclosing films and flow layers thicknesses to maximize stability against evaporation, minimize background scatter, while retaining an easy-to-use/modify flow chip design that can be adapted to match different sample and beamline requirements. Furthermore, methods to functionalize and pattern

the chip to control crystal nucleation and growth on the chip using surface charge interactions were explored to improve sample hit rates. Additional content on the tuning fundamental properties like surface charge of supported lipid bilayers (SLBs) and lipid vesicles is provided in Chapter 4.

Looking forward, our development of these enclosed fixed-target chips, understanding of the effects of polymer surface charge on protein crystallization, and insights gained from fundamental measurements of surface charge of lipid assemblies, could be used together to enable technologies for integral membrane protein (IMP) crystallization. We envision two ways in which favorable electrostatic interactions could be used to facilitate IMP crystallization, shown in **Figure 1**. Charged detergent- or lipid-solubilized IMPs could be concentrated on-chip on polyelectrolyte brushes bearing varying degree of positive or negative charge, either directly to produce 3D crystals, or on polyelectrolyte-cushioned SLBs to produce 2D crystals. Both the presence of a native-like lipid environment and favorable contacts between the brushes and charged amino acid residues on the intracellular or extracellular parts of the IMP will likely aid in stabilizing the protein. These approaches, if successful could pave the way for a generalized tool for IMP crystallization and on-chip structure characterization.

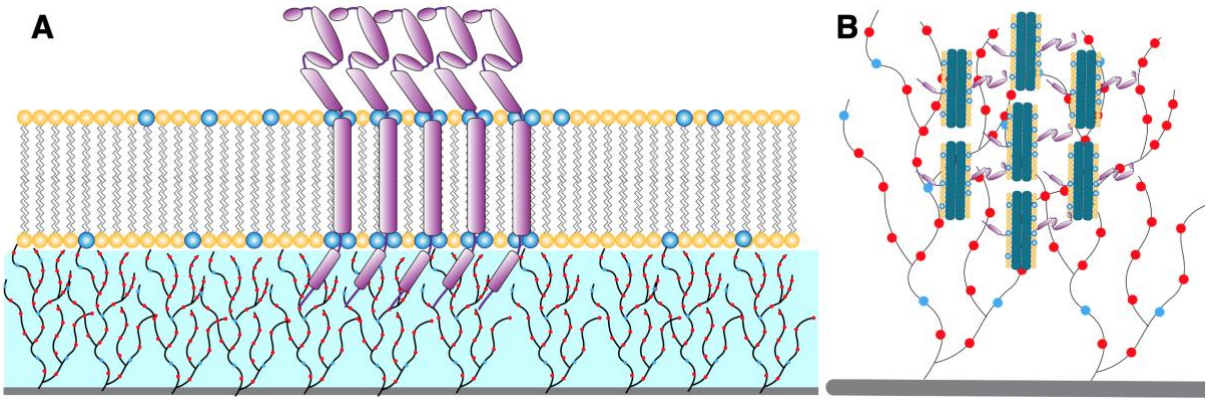

Figure 1: A schematic of (a) 2-D crystallization of IMPs in SLBs deposted on charged polyelectrolyte cushions, and (b) 3-D crystallization of IMPs solublized in lipid particles, driven by surface charge interactions.

1.2 References

1. Berman, H. M. The Protein Data Bank. *Nucleic Acids Res.* 28, 235–242 (2000).
2. Giegé, R. A historical perspective on protein crystallization from 1840 to the present day. *FEBS J.* 280, 6456–6497 (2013).
3. Lin, Y. What's happened over the last five years with high-throughput protein crystallization screening? *Expert Opin. Drug Discov.* 13, 691–695 (2018).
4. Cusack, S. *et al.* Small is beautiful: protein micro-crystallography. *Nat. Struct. Biol.* 5, 634–637 (1998).
5. Smith, J. L., Fischetti, R. F. & Yamamoto, M. Micro-crystallography comes of age. *Curr. Opin. Struct. Biol.* 22, 602–612 (2012).
6. Chapman, H. N. *et al.* Femtosecond X-ray protein nanocrystallography. *Nature* 470, 73–77 (2011).
7. Schlichting, I. & Miao, J. Emerging opportunities in structural biology with X-ray free-electron lasers. *Curr. Opin. Struct. Biol.* 22, 613–626 (2012).
8. Hirata, K. *et al.* Determination of damage-free crystal structure of an X-ray–sensitive protein using an XFEL. *Nat. Methods* 11, 734–736 (2014).
9. Grünbein, M. L. *et al.* Megahertz data collection from protein microcrystals at an X-ray free-electron laser. *Nat. Commun.* 9, 3487 (2018).
10. Orville, A. M. Recent results in time resolved serial femtosecond crystallography at XFELs. *Curr. Opin. Struct. Biol.* 65, 193–208 (2020).
11. Fischer, M. Macromolecular room temperature crystallography. *Q. Rev. Biophys.* 54, e1 (2021).
12. Boutet, S. *et al.* High-Resolution Protein Structure Determination by Serial Femtosecond Crystallography. *Science* 337, 362–364 (2012).
13. Wierman, J. L. *et al.* Fixed-target serial oscillation crystallography at room temperature. *IUCrJ* 6, 305–316 (2019).
14. Lyubimov, A. Y. *et al.* Capture and X-ray diffraction studies of protein microcrystals in a microfluidic trap array. *Acta Crystallogr. D Biol. Crystallogr.* 71, 928–940 (2015).
15. Martiel, I., Müller-Werkmeister, H. M. & Cohen, A. E. Strategies for sample delivery for femtosecond crystallography. *Acta Crystallogr. Sect. Struct. Biol.* 75, 160–177 (2019).
16. Zarrine-Afsar, A. *et al.* Crystallography on a chip. *Acta Crystallogr. D Biol. Crystallogr.* 68, 321–323 (2012).
17. Hunter, M. S. *et al.* Fixed-target protein serial microcrystallography with an x-ray free electron laser. *Sci. Rep.* 4, 6026 (2015).

CHAPTER 2: A FIXED-TARGET PLATFORM FOR SERIAL FEMTOSECOND CRYSTALLOGRAPHY IN A HYDRATED ENVIRONMENT

Shelby, M.L.,[1*] Gilbile, D.,[2*] Grant, T.D.,[3] Seuring, C.,[4] Segelke, B.W.,[1] He W.,[1] Evans A.C.,[1] Pakendorf, T.,[4] Fischer, P.,[4] Hunter, M.S.,[5] Batyuk, A.,[5] Barthelmess M.,[4] Meents, A.,[4] Coleman, M.A.,[1,2] Kuhl, T.L.,[2] and Frank, M.[1,2]

1. Lawrence Livermore National Laboratory, Livermore, CA, USA. 2.University of California at Davis, CA, USA. 3.Hauptman-Woodward Institute, Department of Structural Biology, Jacobs School of Medicine and Biomedical Sciences, SUNY University at Buffalo, Buffalo, NY, USA. 4. Center for Free-Electron Laser Science, Hamburg, Germany. 5. Linac Coherent Light Source, SLAC National Accelerator Laboratory, Menlo Park, California, USA.

Author Contributions:

*These authors contributed equally

Conceptualization, D.G., M.L.S., T.L.K., M.F., M.A.C.; enclosed fixed target design and preparation, D.G.; sample preparation and crystallization, D.G., M.L.S., B.W.S., W.H., A.C.E.; data evaluation, M.L.S., T.D.G.; roadrunner and Si chip design/operation, P.F., T.P., M.B., A.M.; instrument operation for SFX experiments, M.S.H., A.B.; writing, M.L.S., D.G., M.F., M.A.C., T.L.K. All authors have read and agreed to the published version of the manuscript.

Status: Published in IUCrJ, January 2020. DOI: https://doi.org/10.1107/S2052252519014003

Keywords: Serial crystallography; sample delivery; XFELs; in-vacuum studies; fixed-target platforms; graphene; polymers; thin films; microcrystals; sample hydration.

Abstract:

For serial femtosecond crystallography (SFX) at X-ray Free Electron Lasers (XFELs), which entails collection of single-pulse diffraction patterns from a constantly refreshed supply of microcrystalline sample, delivery of the sample into the X-ray beam path while maintaining low background remains a technical challenge for some experiments, especially where this methodology is applied to relatively low-ordered samples or those difficult to purify and crystallize in large quantities. This work demonstrates a scheme to encapsulate biological samples using polymer thin films and graphene to maintain sample hydration in vacuum conditions. The encapsulated sample is delivered into the X-ray beam on fixed targets for rapid scanning using the Roadrunner fixed target system towards a long-term goal of low-background measurements on weakly diffracting samples. As a proof of principle, we used microcrystals of the 24 kDa Rapid encystment protein (REP24) to provide a benchmark for polymer/graphene sandwich performance. The REP24 microcrystal unit cell obtained from our sandwiched in-vacuum sample was consistent with previously established unit cell parameters and with those measured by us without encapsulation in humidified helium, indicating the platform is robust against evaporative losses. While significant scattering from water was observed due to the sample deposition method, the polymer/graphene sandwich itself was shown to contribute minimally to background scattering.

2.1 Introduction

The advent of hard X-ray Free Electron Lasers (XFELs), including the Linac Coherent Light Source (LCLS) at SLAC National Accelerator Laboratory in 2009, has opened up exciting new opportunities for structural biology[1-4]. The ultrafast, high brightness pulses from XFELs allow the collection of nominally damage-free[5] single-pulse diffraction images from biological micro- and

nano-objects at room temperature, including protein microcrystals[6,7], individual virus particles[8,9], or even weaker diffracting nano-objects, such as 2-dimensional protein crystals[10-12] or protein fibrils[13]. High-resolution, three-dimensional structures of a protein can be derived from a large collection of individual diffraction patterns (typically thousands for a full diffraction data set) obtained sequentially from individual microcrystals in random orientations that are replenished in between X-ray pulses[14-16]. This Serial Femtosecond Crystallography (SFX) approach is becoming an increasingly routine method for macromolecular structure determination[17-21], but challenges remain for the application of this approach for more weakly diffracting samples.

A major challenge in biological imaging with XFELs is the requirement to continuously inject sample to the XFEL focus 1) at a rate that matches the pulse repetition rate of the XFEL (120 Hz in the case of LCLS), 2) in vacuum to minimize background scattering from air especially in the case of small or weakly diffracting objects and, 3) in such a way that sample hydration is maintained to prevent degradation. Various types of continuous sample delivery systems have been developed [22] and liquid jet injectors that utilize gas dynamic virtual nozzles (GVDNs) to inject hydrated microcrystals and lipidic cubic phase (LCP) injectors[23,24], are workhorses for sample injection for SFX. However, high consumption (~20 µL/min and milligrams of protein for a full SFX diffraction data set for liquid jets, ~100 µg for LCP jets) and the X-ray scatter background from the water and buffer components are drawbacks. Tape drives mitigate challenges related to sample consumption by synchronizing drop arrival to the X-ray pulse timing[25,26], but similarly suffer from background contributions from the relatively large aqueous droplet and the tape material that supports the drop. Aerodynamic lens-based aerosol injectors[27,28] have very low scattering background for imaging but the probability of an X-ray shot resulting in a measurable diffraction pattern, or hit rate, is low.

An alternative to is to introduce the sample via sample supports which are scanned through the X-ray beam such that fresh sample is introduced for each X-ray shot. This "fixed-target" approach can drastically reduce the amount of sample required for obtaining a full diffraction data set. Hit rate can be maximized by increasing sample deposition density. The fixed target approach also poses several practical experimental challenges including X-ray scatter background from the sample support, relatively slow speed of data acquisition due to mechanical stepping or scanning of the sample, and the need to maintain sample hydration when exposed to vacuum.

Various fixed-target approaches for biological imaging at XFELs and at synchrotrons, where serial crystallography approaches with similar challenges are increasingly being implemented, have been investigated over the last decade to address these challenges. A number of sample supports have been developed for serial fixed-target femtosecond crystallography (FT-SFX) and serial synchrotron crystallography (SSX) including microgrids based on silicon[29] or polymers[30,31], silicon or polymer chips with silicon nitride membranes[11,32,33], and micropatterned silicon chips[34]. Various schemes for mitigating sample dehydration have been employed to maintain a functional species at room temperature, including enclosing microgrids with polymer films[35-40], surrounding microcrystal samples with protective oil, such as Paratone N[32] or grease[41], embedding 2D crystal samples in sugar[11], or providing a humidified air or helium atmosphere[34,42,43]. While early FT-SFX experiments at LCLS and other XFELs were performed at fairly low scanning speeds (~10 Hz) the "Roadrunner" fast scanning stage system that was developed by the Centre for Free-Electron Laser Science (CFEL) utilizes fast stages that are synchronized with the X-ray pulse repetition rate such that X-rays shots hit through the micropores of a micropatterned silicon chip[43]. The sample can be supported in humidified helium with adjustable relative humidity, allowing for bare crystals to be measured on the chip[34]. Roadrunner

has also been implemented in ultra-high vacuum, but without adaptation of the supporting chip to mitigate sample dehydration.

To utilize this fast-scanning platform for small crystals, nano-objects, and ordered films, compatible strategies to provide a continuous supporting substrate with minimal X-ray scattering background must be developed. In recent years, single-layer graphene, an ultra-thin material with excellent mechanical, thermal and barrier properties[44,45], has been used at synchrotron sources for mounting protein crystals in a cryoloop to minimize background and prevent sample dehydration[46], as a water-barrier film over windows in graphene-based microfluidics[47] and as a low-background support material to align amyloid fibrils[13]. Given its ultra-thin nature, stand-alone graphene is difficult to handle and produce without cracks resulting from the etching steps.[48-50] These cracks can severely affect the barrier properties of graphene for in-vacuum studies.

Therefore, our strategy towards background minimization for weakly diffracting samples was to explore the use of large-area few-layer graphene (FLG) in conjunction with polymer thin-films, which would impart mechanical robustness, flexibility, and allow for easy handling while adding minimally to the X-ray scatter background. We used these hybrid films as enclosing layers to maintain sample hydration for room temperature studies in the Coherent X-ray Imaging (CXI) end station[51] vacuum environment with micropatterned fabricated Si substrates compatible with rapid-scanning approach utilizing Roadrunner. A crystal slurry is deposited and spread by capillary force between these enclosing films, limiting physical stress on the crystals. SFX experiments were performed in both the vacuum environment of CXI and the humidified environment at the Macromolecular Femtosecond Crystallography (MFX) end station[52] without encapsulation. Our initial studies focus on 24 kDa Rapid encystment protein (REP24) to provide a benchmark for polymer-graphene sandwich performance. By performing a comparative study of REP24

diffraction encapsulated in-vacuum and without encapsulation in humidified helium, we determine the device is robust against evaporative losses.

2.2 Materials and methods

Serial diffraction from batch-grown microcrystals of REP24 was measured on pore-patterned Si chips both 1) at CXI, in vacuum with the crystals encapsulated in polymer-graphene hybrid films and 2) at MFX, in a humidified environment on a bare Si chip (without encapsulation, or "sandwiching") to benchmark the performance of the sandwich towards preventing dehydration. The following descriptions of the protein crystallization, chip design, and the performance of the SFX experiments pertain to experiments in both conditions unless otherwise noted.

2.2.1 Preparation of graphene-polymer thin films

Chemical vapor deposited FLG on nickel grown on a 4-inch silicon wafer with a 300 nm silicon oxide layer was purchased from Graphene Supermarket (Calverton, NY, USA) and cut to desired dimensions as required. Graphene grows on nickel in 3-10 μm sized patches with each patch bearing a thickness between 1-7 monolayers (**Figure 1A**). The wafers were rinsed with a 2 vol.% Hellmanex™ III and MilliQ water (18.2 MΩ) thoroughly, and dried with high purity nitrogen prior to use, to remove any silicon particles generated during cutting and handling.

PMMA-assisted transfer of graphene to substrates has been well established in literature[48-50]. 4 wt. % poly (methyl methacrylate) (PMMA) in anisole with a molecular weight 950,000 g/mol (950PMMA A4) was purchased from Microchem (Westborough, MA, USA). The solution was diluted to 0.8 wt.% and spin-coated onto the FLG-wafer at 2500 rpm for 90 s, followed by annealing at 80 °C for 15 min to form a polymer film approximately 40 nm thick as measured by profilometry (Dektak 150).

The PMMA-coated FLG-wafer was subsequently immersed in buffered oxide etchant (Transene Buffer HF Improved) for 30 - 60 min to etch the silicon oxide layer, thereby detaching PMMA/FLG/nickel film from the silicon wafer. The nickel layer was etched by transferring this film to the surface of a ferric chloride bath (Transene CE100) diluted 1:9 in MilliQ water (18.2 MΩ) to allow for slow etching, followed by three rinse cycles in MilliQ water (20 min each) to remove any residual etchant. **Figure 1A** shows the schematic for preparation of PMMA-FLG films. Additional information on graphene film characterization is presented in the supplemental information. (**Figure S1, S2**)

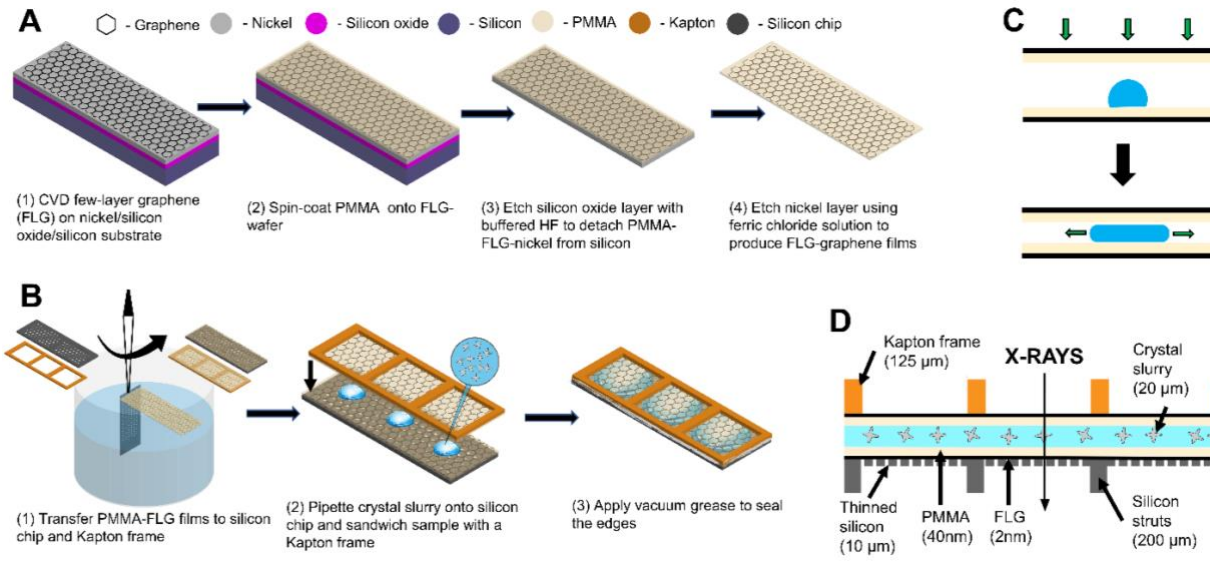

Figure 1: Schematic for A) preparation of PMMA-FLG thin films and B) transfer to substrates and final sample assembly, C) Spreading of sample droplet over chip area by capillary action, D) A cross section of the assembled device.

2.2.2 Preparation of REP24 microcrystals

REP24 (24 kDa; pdb16 code 4P5P), a putative virulence factor protein from the intracellular pathogen *Francisella tularensis*, was expressed recombinantly and purified as described previously[32,53]. Batch crystallization conditions were utilized for the production of the REP24

crystals in bulk. REP24 crystals were grown by mixing a 14.4 mg/mL REP24 sample (in 50 mM NaCl and 10 mM HEPES pH 7.5) with a precipitation solution containing 54% (v/v) PEG-MME 750 and 100 mM Na-acetate pH 4.5 in a 1:1 ratio for final conditions of 7.2 mg/mL REP24, 27% (v/v) PEG-MME 750, 50 mM Na-acetate pH 4.5, in 25 mM NaCl, and 5 mM HEPES pH 7.5. The crystals of REP24 used in the experiment were between 15 μm and 20 μm in length and had the appearance of two, square-based pyramids connected at the peak, with maximum thickness of 10 μm. Crystal concentrations were estimated at 2.2 x 10^6 crystals/ml based on counts done via optical microscopy of a fixed volume.

2.2.3 Chip design and sample assembly

Micro-patterned single crystalline silicon chips were commercially manufactured by Finnlitho (Joensuu, Finland), requiring approximately 30-day turnover time to take advantage of micro-precise patterning capabilities, which were compatible with the Roadrunner fast scanning system and are available directly from the manufacturer. All chips used follow the design principles of second generation Roadrunner chips described previously[54]. Each chip (32.7 mm x 12 mm) was comprised of a 200 μm thick frame with an 18 x 5 array of 1.5 mm x 1.5 mm rectangular areas of Si ("windows") thinned to 10 μm and supported by 100 μm wide struts in between the windows. These windows were patterned with a hexagonal dense pattern of 15 μm pores spaced 50 μm apart, yielding >100,000 pores that could hold crystal samples (**Figure S3**). Chips with a slightly different window configuration (6 x 2 array, 7.5 mm x 4.3 mm) and pores spaced 100 μm apart were used in MFX measurements. Due to the nature of the manufacturing process the chips have a flat polished side and a structured side that features the recessed areas of the membrane with holes and supporting struts. Chips were screened for breakage or surface damage, sonicated in acetone and isopropanol for 10 minutes each and dried with ultra-pure nitrogen gas prior to film

attachment to the polished side. Kapton frames (Dupont™ Kapton® 500HN, 125 µm) of dimensions 32.7 mm × 12 mm, with large (10 mm × 10 mm) holes were prepared using a plotting cutter (Cricut Explore Air 2).

2.2.3.1 Sandwiched sample assembly for CXI

The chips or Kapton frame were lowered into the water under the PMMA-FLG film floating at the air-water interface, and its edge was carefully aligned with the floating film, touched and slowly raised at a 60-90° angle to allow water to recede from under the film as shown in **Figure 1**. The PMMA-FLG coated substrates were allowed to air dry for 15 min followed by annealing at 80 °C for 15 min to evaporate any residual water. A PMMA-FLG coated Finnlitho chip is shown in **Figure S3B**.

The resulting PMMA-FLG coated chips (comprising the bottom layer of a sample sandwich) were mounted film side up to custom-fabricated aluminum frames bearing magnetic mounts for loading onto the goniometer of the fast-scanning Roadrunner systems used for the experiments at LCLS[42,43]. Alignment pins in the aluminum frames allowed for precise alignment of the chips as they were attached to the aluminum frames with nail polish. Approximately 20 µL of the microcrystal slurry was carefully pipetted onto the chip and a PMMA-FLG coated Kapton frame was then carefully aligned with the chip and placed film side down on top of the microcrystal solution. The solution then spread by capillary action to cover a large area of the chip. A schematic of this spreading action is shown in **Figure 1C**. The edges of the chip and film sandwich were sealed by application of a thin layer of vacuum grease to prevent dehydration. A cross section of this assembly is shown in **Figure 1D**. Before the beamtime, the sandwich assembly (using silicon chips with larger 50 µm pores) was tested for vacuum stability using an in-house vacuum chamber. The crystals appeared intact after 30 minutes of vacuum exposure as seen in **Figure S4A** and in

no case did we observe delamination of the assembly. Crystals have no apparent preferred orientation when deposited (**Figure S4B**).

2.2.3.2 Sample preparation for MFX

For humidified environment experiments at MFX, bare Finnlitho silicon chips were loaded with 50 µL of freshly crystallized REP24 microcrystal suspension within a specialized humidified chamber by pipetting and spreading the crystal slurry onto the flat side of the chip and wicking away excess mother liquor from the opposite side to aid in drawing microcrystals into the chip pores[34,42]. The loaded chips were then immediately transferred to the Roadrunner sample chamber, which was constantly flushed with humidified helium (near 100 % humidity).

2.2.4 Serial femtosecond crystallography data collection

SFX experiments took place during two brief 6 hour Protein Crystal Screening beamtimes. They were conducted at LCLS in humidified atmosphere and in vacuum using the humidified helium environment Roadrunner III system at the MFX end station and the newly developed vacuum-compatible Roadrunner IV system in the 0.1 µm *in vacuo* sample environment of the CXI end station, respectively. Roadrunner III and IV systems share main design elements with previous versions of the Roadrunner system which have been demonstrated at LCLS and elsewhere in the past and their capabilities described[26,42,43,55]. These include high precision stepper motor-driven x,y,z translation stages, a brushless motor linear stage for high speed-scanning of chips oriented in the horizontal direction and a high precision goniometer. Development of Roadrunner II and IV is not the focus of this work and will be described in forthcoming publications.

The procedure for sample mounting and data collection is similar for both systems. After mounting chips were scanned through the X-ray focus row-by-row where the x-axis is the fast-

scanning axis. Scanning speed is precisely controlled such that the arrival of each X-ray pulse at the 120 Hz repetition rate of LCLS was coincident with the spatial alignment of a micropore on the chip. The scanning was facilitated by a chip geometry definition file of each chip design that was pre-loaded into the Roadrunner data collection software before the experiments, allowing the software to calculate the necessary acceleration and velocities to synchronize the arrival of a chip window with the LCLS pulse. A high-resolution inline viewing microscope was used to view and align the samples.

For in-vacuum experiments, samples were loaded and exposed to vacuum during the initial 20 min pumpdown of the sample chamber and subsequent 30 min runtime of the chip (including ~20 min data collection time and ~10 min dead time). For experiments in humidified helium, the chips were immediately transferred to the Roadrunner III sample chamber flushed with humidified helium (99 to 100 % humidity) after loading. Humidity at the sample was monitored throughout the course of the experiment to ensure >99% humidity.

SFX experiments were conducted at an X-ray energy of 7.5 keV and 9.5 keV with a beam size at the sample of 120 nm x 170 nm FWHM and 3 µm x 3 µm FWHM for experiments at CXI[56] and MFX (humidified atmosphere), respectively. REP24 samples were measured with between 1 % and 10 % beam transmission and not the full X-ray flux of 4.5 mJ/pulse due to 1) the saturation of detector pixels within Bragg spots at higher flux and 2) concerns regarding damage to the chip resulting from the lower-intensity "wings" of the X-ray beam around the central focus spot (~1 % of the total intensity). All chips were assessed for damage immediately following measurement with optical microscopy. The nominal pulse duration was 40 fs for both experiments. During each sample scan, diffraction images were recorded on a shot-by-shot basis at the full 120 Hz repetition rate of LCLS by a Cornell-SLAC Pixel Array Detector (CSPAD)[57]. As data were collected, X-ray

images were analyzed for estimating hit rate using OnDA for immediate feedback[58]. Images from all X-ray shots were analyzed offline using Cheetah[59] to find crystal hits with the following parameters: minimum peak intensity threshold of 200 ADC, minimum SNR of 6, minimum number of pixels per peak of 2, minimum number of peaks per hit of 10. CrystFEL[60] was used for indexing patterns and to estimate resolution using the MOSFLM indexing algorithm[61].

2.3 Results and Discussion

2.3.1 SFX experiments

In the humidified helium environment at MFX, CSPAD images from ~21,000 shots were recorded with ~8,000 containing hits (38% hit rate) of REP24 microcrystals on the bare chip, of which 5,500 (69 %) were successfully indexed. The indexed unit cell dimensions were a = 45.3 ±0.1Å, b = 45.3 ±0.1 Å, c = 183.9 ±0.2 Å, α = 90.0 ±0.1°, β = 90.0 ±0.1°, γ = 120.1 ±0.1° (**Figure 2**). The maximum per-frame resolution was 1.9 Å while the median resolution was 2.3 Å. During SFX experiments at CXI in vacuum, approximately 60,000 shots were recorded, ~4800 of which contained measurable diffraction data from microcrystals encapsulated in the sandwich and were determined to be hits (8 % hit rate, see section 3.3 for a comparison of the hit rate). Of these hits about 1400 (30 %) were successfully indexed and exhibited unit cell constants of a = 47.0 ± 1.0 Å, b = 47.2 ± 1.2 Å, c = 183.5 ± 1.6°, α = 90.2 ± 0.4 Å, β = 89.9 ± 0.4°, γ = 120.9 ± 1.0°, (**Figure 2**).

The observed unit cell in both cases is consistent within the error of the respective measurements with the unit cell determined for larger REP24 crystals by synchrotron experiments at cryogenic temperature (pdb code 4P5P)[62] a = 44.4, b = 44.4, c = 183.5, α = 90.0°, β = 90.0°, γ = 120.0°. Previous room temperature measurements of REP24 using fixed target SFX also yielded a comparable unit cell as synchrotron single crystal measurements: a = b = 44.4 Å, c = 183.5 Å, α = β = 90°, and γ = 120°, indicating that cryogenic cooling does not significantly impact the unit

cell. These utilized similar micro-crystallization conditions but adopted a very different approach to preventing dehydration in which the microcrystals were suspended in Paratone-N and then spread onto a silicon nitride support, which is not applicable to weakly diffracting samples[32]. The slightly larger average unit cell within the sandwich may indicate that the enclosure of the microcrystals inhibits any loss of hydration due to removal from the mother liquor for mounting or suspension in Paratone-N as was done for the MFX experiment and previous measurements of REP24.

Table 1: Statistics for the reflections collected for REP24 in the PMMA-FLG enclosure.

Resolution (Å)	Number of reflections observed	Number of possible reflections	Completeness of data (%)	Total measured reflections	Redundancy
7.3	3213	3213	100.0	175780	54.7
3.6	3212	3212	100.0	101608	31.6
3.0	3178	3178	100.0	83537	26.3
2.7	3208	3208	100.0	72609	22.6
2.5	3160	3161	100.0	68412	21.6
2.3	3217	3218	100.0	52385	16.3
2.2	3167	3176	99.7	34518	10.9
2.1	3131	3233	96.9	21996	7.0
2.0	2828	3185	88.8	13011	4.6
1.9	1981	3176	62.4	6464	3.3
Total	30295	31960	0.9	630320	20.8

Sandwich encapsulated crystals diffracted to a maximum resolution of 2.2 Å, comparable to previous SFX experiments, and a median resolution of 3.5 Å (**Figure 2**). Neither the diffraction limit distribution nor the mean diffraction limit changed significantly during the measurement time. The unit cell volume distribution was also constant throughout the experiment (**Figure S5**),

indicating that the graphene/polymer sandwich afforded a high degree of protection against dehydration to the microcrystals during the experiment and prevented degradation of diffraction quality. Insufficient data were collected for full structure determination for in-vacuum experiments as determined by the R_{split} figure of merit (75.0 % for the entire dataset)[60]. Statistics for the reflections collected according to resolution shell are tabulated in **Table 1**.

It is notable that the maximum and mean resolution of REP24 measured in humidified helium showed some improvement over those measured in-vacuum within the sandwich, primarily in that the distribution of maximum frame resolution was much wider at CXI, with a standard deviation of 1.1 Å in vacuum vs 0.3 Å in humidified helium. There is also a much larger variance in the unit cell dimensions for the CXI dataset, which is evident in the histograms of indexing solutions (**Figure 2**), although this is partially due to the lower number of indexed hits during the in-vacuum experiment. The source of this heterogeneity and whether it originates from 1) interactions between the microcrystals and the graphene or polymer surface, 2) partial drying of the sample, or 3) crystallization of a more non-uniform crystal slurry due to differences in purified protein batch or crystallization conditions is not currently clear. One would expect drying to result in a time-dependent shrinkage or a general decrease of the unit cell volume compared to the experiment in humidified helium, which does not appear to be the case. While interactions between the microcrystals and the graphene or polymer surface are not ruled out, one might expect this to manifest in more of a bimodal distribution with a population that strongly interacts with the surface and one that does not. Batch crystallization during the CXI beamtime resulted in a more varied distribution of crystal sizes according to optical images taken before measurement, which provides some indication that 3) is the most likely explanation of this phenomenon.

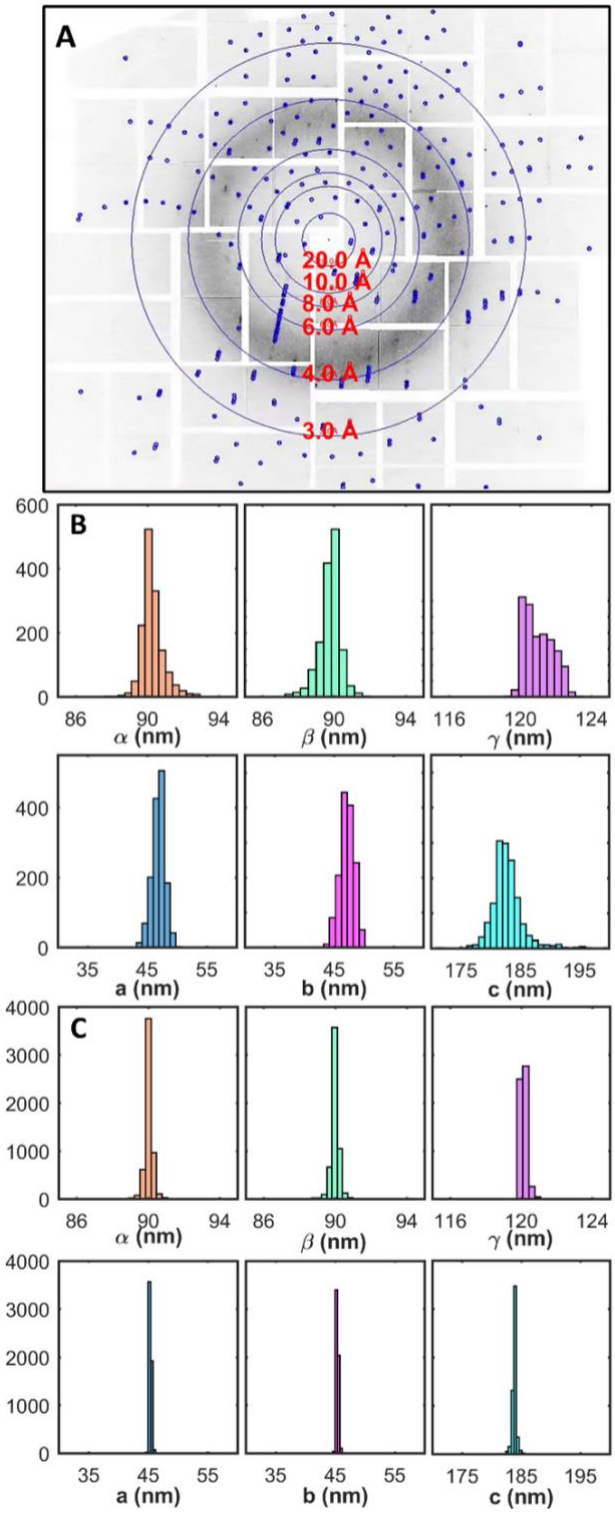

Figure. 2: A) REP24 microcrystals diffract up to ~2.3 Å. No degradation of resolution was observed as exposure time to vacuum increased. B) Histograms of unit cell parameters from ~1,400 indexed patterns in vacuum. C) ~5,500 indexed patterns in humidified helium.

2.3.2 Polymer-graphene sandwich performance

The relatively low hit rate for the in-vacuum experiment compared to the humidified helium experiment (~8 % vs 38 %) can be explained by the difference in crystal deposition methods for each experiment. The sample was unsupported in humidified helium and excess liquid was removed by wicking on the opposite side of the chip to deposition, eliciting a focusing effect where crystals are drawn into pores by the wicking process. The sandwiching method employed in-vacuum relies on capillary action to spread the solution applied to the first polymer/graphene film when the enclosing graphene/polymer layer is applied. While the hit-rate reported for the in-vacuum experiment was relatively low compared to both the MFX experiment and the ideal hit rate (for randomly distributed crystals and Poissonian statistics, the maximum single crystal hit rate of ~37 % is achieved at a total hit rate of ~63 %), higher hit rates can easily be achieved by concentrating the microcrystal slurry by centrifugation before application to the chip to be sandwiched. The crystal density across the chip is not uniform due to this process of spreading and this was observed as an unevenness in the hit rate as the chips were scanned in these studies (**Figure 3C**).

Though preparation of the polymer/graphene hybrid films was somewhat labor intensive due to multiple etching and washing steps, we found the prepared films could be transported to the beamline on mica and transferred to the silicon chip and Kapton frame components shortly before beamtime. The actual sandwich assembly was done on the fly throughout the beamtime and sandwiched microcrystal slurries were stable for several hours at room temperature and atmospheric pressure while they awaited measurement. The thinness of the enclosed water layer inhibited any redistribution of the crystals during this waiting period and no gravity-related pooling of crystals to the bottom of the chip was observed during measurement.

Intact microcrystals were observed in areas of the chip between pores (and therefore not exposed to X-rays) after measurement, suggesting that hydration is locally maintained despite physical damage to the chip and the membrane substrates. Currently, damage to both the graphene/polymer films and the Si membrane itself as a result of beam exposure makes the assembly one-time-use under these measurement conditions. While in the case of REP24 permissible X-ray flux on the chip was limited to avoid detector saturation within Bragg spots, the Si chip itself imposes a limit to incident flux. While the nominal beam sizes (FWHM) for both experiments are well within the pore sizes used, there are spatially broad "wings" that are still sufficiently intense to cause significant damage to the chips themselves. This becomes problematic if this damage either causes melting of the Si substrate and thus significant amorphous Si scatter signal or if this damage causes cracks to propagate down a row of pores, resulting in physical deformation of the chip. While strong single crystal Si Bragg reflections are at higher angles than typically observed for macromolecular crystals, rotation of the Si membrane due to this physical damage may result in these potentially damaging reflections appearing on the detector. This bolsters the case for development of amorphous polymer chip materials both to prevent unintended exposure of the detector to strong reflections resulting from damage and to reduce manufacturing costs.

The unit cell of REP24 found by analysis of diffraction data derived from in-vacuum and humidified atmosphere experiments were in good agreement and indicate that the presented method of sample enclosure with graphene and polymer films is robust against evaporative losses. To our knowledge, other methods utilizing polymer films and/or graphene as supporting or enclosing substrates for XFEL or synchrotron studies either used much thicker polymer films (micrometers thick) alone[35-38,40,63], to support graphene[64,65], or did not provide continuous coverage over the entire area of the chip due to the difficulties with handling large areas of

unsupported graphene[13]. Thicker films do provide a more robust barrier to evaporation but require larger microcrystals to compensate for increased X-ray scatter background. For relatively low-order and poorly diffracting objects, it will be critical to minimize the background contribution of the sample enclosure, while maintaining sample hydration and crystal integrity and, therefore, the sandwiching approach presented here is expected to be beneficial compared to some of the other approaches.

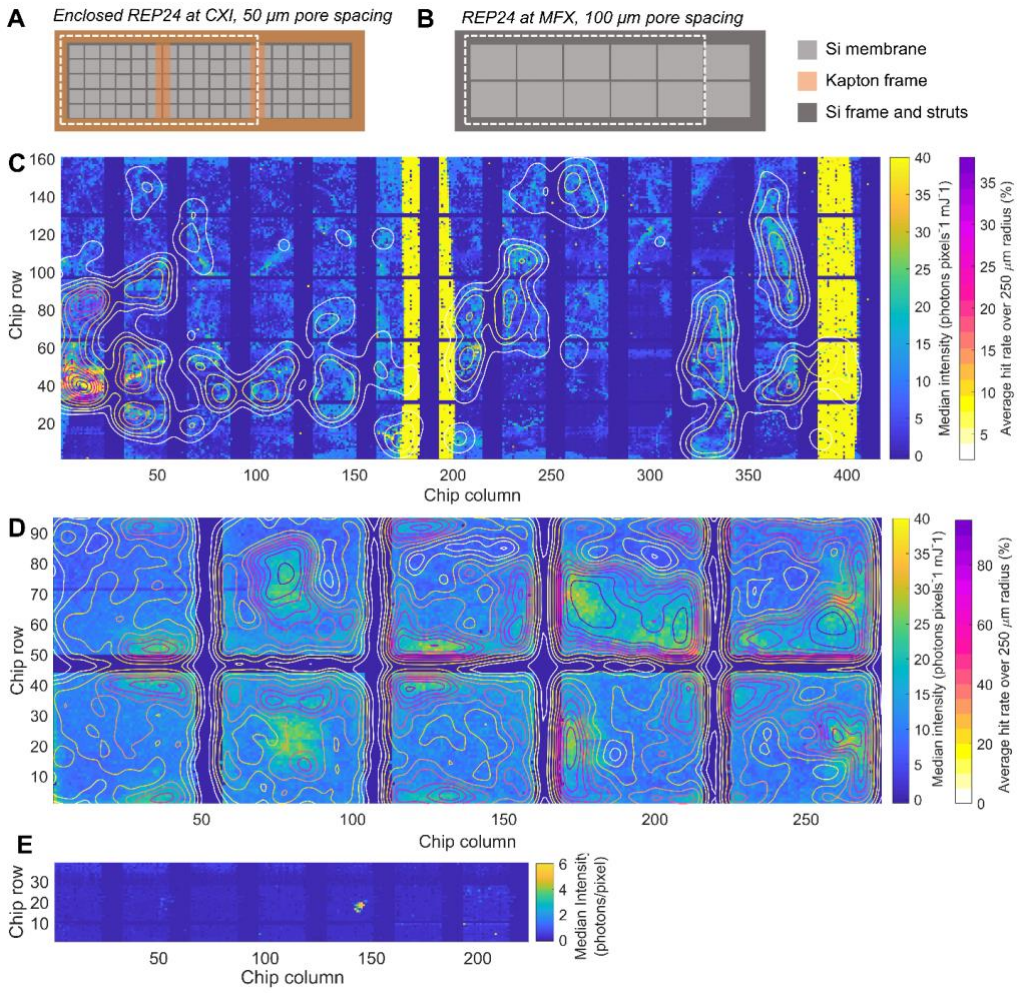

Figure 3: Areas of chips measured for REP24 at A) CXI and B) MFX represented by the median intensity heat maps below. Heat maps of median intensity overlaid with contour plots of hit rate for C) the enclosed REP24 sample at CXI, D) the REP24 sample at MFX, and E) the thin film/ PMMA-FLG sample at CXI.

2.3.3 Origin of contributions to background scattering

In an effort to understand the contributions to the background of the enclosed sample, device, and sample environment, median scattering intensities were calculated for REP24 within the PMMA-FLG sandwich and a PMMA-FLG sandwich containing a non-crystalline thin film (~ 5-10 nm) sample consisting of protein and lipid and deposited onto the chip without water, and on the bare Si chip in humidified He at MFX. These median intensities were arranged to spatially represent variations in background across the chip. Radial averages of each detector frame for both MFX and CXI experiments were calculated, normalized according to the incident pulse energy and degree of beam attenuation, and converted to photons/pixel by identifying the detector response corresponding to the single photon peak in a histogram of single-pixel detector response for the whole detector. The median photons/pixel was calculated per-shot for each scattering profile to exclude sharp peaks resulting from Bragg reflections. This intensity was sorted by time stamp and the chip row number recorded by the Roadrunner translation software (**Figure 3C-E**).

In general, the chip with sandwiched REP24 contains three populations, very high intensity shots above 40 photons/pixel, very low intensity shots below 5 photons/pixel, and a population with variable intensity between about 10 and 35 photons/pixel (**Figure 3C**). The majority of the high intensity shots correspond to the location of the Kapton frame used to support the second enclosing layer of polymer-FLG film. The shots of moderate intensity are not uniformly distributed across the rest of the chip but are clustered in regions. Representative radial scattering profiles for shots distributed through these regions **(Figure 4A)** indicate that the dominant component of this varying signal is a broad peak, which corresponds to liquid water[66]. A contour plot overlay representing hit rate over a 250 μm diameter indicates that the hits are localized in areas with relatively high water background (**Figure 3C**). The localization of hits around pockets of thicker water layers is

likely due to the manual method of deposition that relies on the capillary force of the buffer to spread the sample. To optimize sample density and hit rate while minimizing water film thickness, methods could be imagined that deposit many more concentrated drops over the sample area before encapsulation, redesign the chip to allow controlled wicking for water removal, or employ surface functionalization to fix crystals to the film surface before water removal.

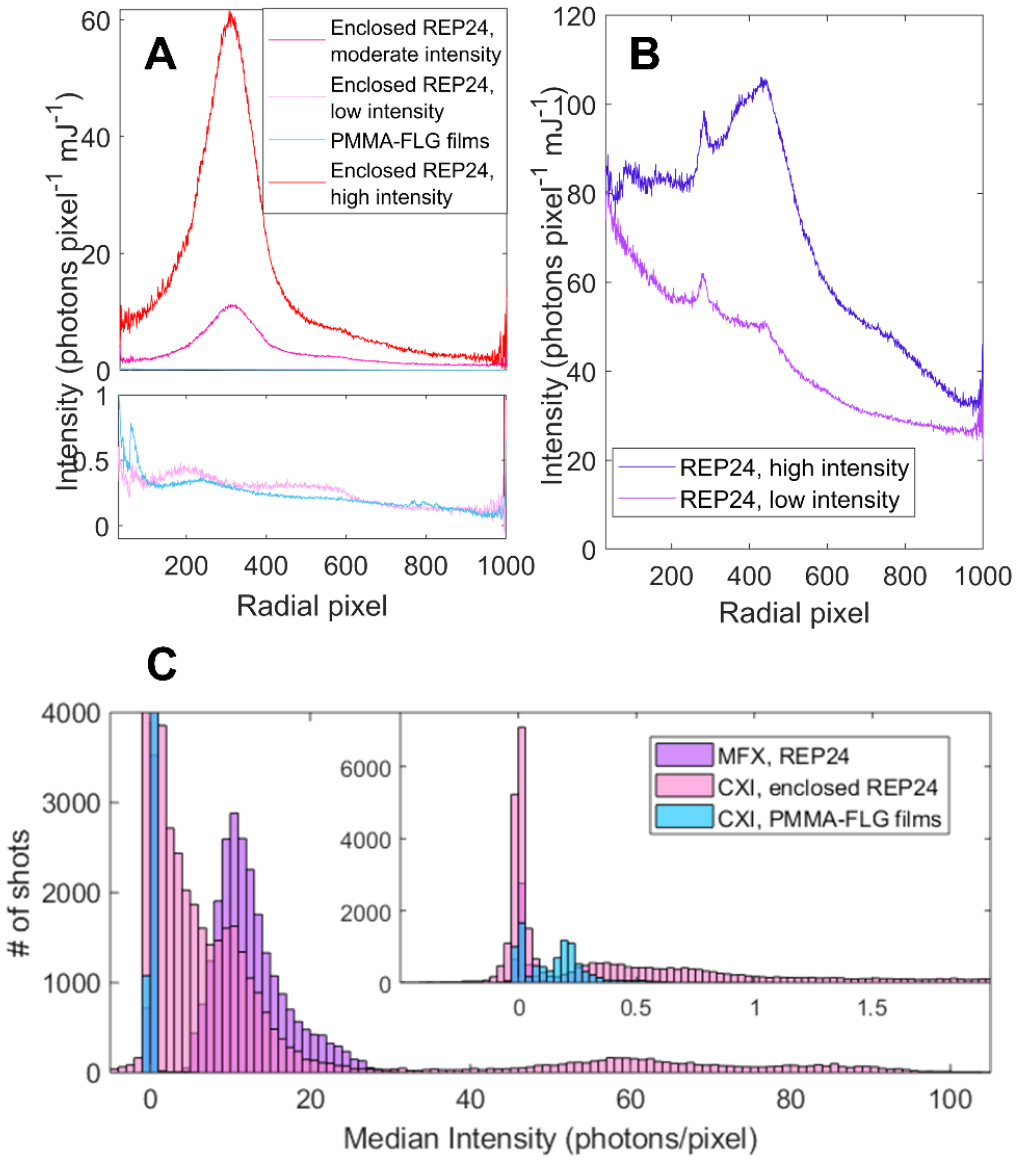

Figure 4: Representative radial scattering profiles from A) CXI and B) MFX experiments. C) Histograms of median intensities, (inset) low intensities populations zoomed in.

The PPMA-FLG sandwich containing the thin film sample at CXI is extremely uniform and the vast majority of shots have median intensities of less than one photon/pixel (**Figure 3E**). These shots are similar to the low-intensity population of shots for the sandwiched REP24 chip, both in their median intensities and in their radial scattering profiles (**Figure 4A**). The median intensities of the chip measured at MFX have a higher floor and the areas of highest intensity are also clustered in certain regions of the chip that mostly correspond to higher hit rate (**Figure 3D**). Scattering profiles of shots at relatively low intensity and high intensity have a broad sloping background that is likely due to scattering from the humidified He environment. High intensity shots also have a broad peak at that is likely due to residual water (**Figure 4B**)

As a point of comparison to our experimental results, the total number of photons scattered (N_{scat}) onto the CSPAD for each component of the enclosure, PMMA, FLG, and water, was modeled based on the following formula:

$$N_{scat} = \frac{N}{A_b} M\sigma$$

where N is the number of incident photons, A_b is the area of the beam, M is the number of atoms or molecules in the beam, and σ is the atomic or molecular Rayleigh scattering cross section (from the xraylib library, [67]. Calculated scattered photons are tabulated for the components relevant to our study and other films used for microcrystal encapsulation in **Table 2**. For two PMMA-FLG films consisting of four layers of graphene and 40 nm of PMMA, modeled graphene and PMMA scatter 1.0 $x10^5$ and $1.8x10^6$ photons respectively per 1mJ incident pulse energy at 7.5 keV. A 1 μm film of water scatters 7.8 $x10^6$ photons, and we anticipate the water thickness surrounding the crystals to be the same dimension as the crystal size, about 20 μm, thus the total contribution from water is about 1.6 $x10^8$ photons. This is consistent with our observation that the water signal

dominates the background for our encapsulated sample. While more water is removed from the chip at MFX and water scatters less at 9.5 keV (6.6 $x10^6$ photons for 1 μm) the contribution from water vapor for He at 100 % humidity at room temperature is likely to be significant (2.6 $x10^8$ photons per cm). By contrast, Mylar films used to sandwich microcrystals in[63], where the water layer is reported to be a similar thickness, would scatter 1.4 $x10^8$ photons per 1mJ incident pulse energy at 7.5 keV for two 2.5 μm films.

Table 2: Computed scattered photons under measurement conditions for various device components and other potential sources of background scattering.

Material	Thickness	Energy (keV)	Total scattered photons at 1mJ/pulse
Graphene	8 layers	7.5	1.0E+05
PMMA	80 nm	7.5	1.8E+06
Water	1 μm	7.5	7.8E+06
	20 μm	7.5	1.6E+08
	1 μm	9.5	6.6E+06
Water vapor at 100% humidity at 20°C in He	1 cm	9.5	2.6E+08
He at 20°C	1 cm	9.5	7.2E+05
Mylar	5 μm	7.5	1.4E+08

The very low background intensities across the chip for the thin film sample and the nature of the varying background for the enclosed sample indicates that the vast majority of the enclosed sample background originates from an encapsulated water layer of varying thickness. The polymer, graphene, and Si components of the device together contribute on average less than one photon/pixel to the background, which is ideal for measurement of weakly diffracting objects.

While the thickness of the water layer prevented a truly low background measurement in this case, the manual deposition process can be optimized to reduce or remove excess water enclosed. While the wicking of excess buffer from the bare chip at MFX appears to have reduced the liquid water background, this effect is largely counteracted by the broad background from humidified He. As can be seen from the distribution of shot intensities (**Figure 4C**), the enclosed sample in vacuum shows most images have low background below 10 photons/pixel with no effective lower limit, whereas the MFX sample in humidified He shows most images contain above 10 photons/pixel, with a lower limit of 5 photons/pixel. These results demonstrate that the background scattering of the enclosed chip in vacuum can be significantly less compared to the background scattering of the humidified He environment.

2.4 Outlook

New fast-scanning systems have made fixed target data acquisition at the 120 Hz repetition rate of LCLS possible, drastically reducing measurement time for fixed target SFX experiments and making studies of low-order samples feasible in a relatively short time frame. Recently, even higher scanning rates up to 1 kHz have been demonstrated using a Roadrunner system together with Jungfrau 1 M detector at the ESRF synchrotron where precise alignment with pores is not a concern[68]. While some of the other delivery methods also have the benefit of low sample consumption, for instance LCP and high-viscosity jets, background reduction is critical for both small micro- (or nano-) crystals and samples exhibiting poor diffraction or diffuse features. The reported method enables low-background, high-repetition rate measurements of such samples while maintaining a near native hydrated environment to make SFX more accessible to new kinds of biological studies.

The next generation of high repetition-rate XFELs, including the newly opened European XFEL and LCLS-II, currently under construction, will provide potentially much higher rates of data acquisition but also introduce new challenges to sample delivery for SFX. Delivery schemes that minimize down time (for instance due to injector clogging or fixed-target sample exchange) and provide a modular, well controlled sample environment will be better adapted to take advantage of the faster rate of data acquisition. To this end we are currently adapting this sample support enclosure approach to include low-cost polymer frames that can maintain sample hydration over long periods of time and substrate functionalization and patterning to control sample deposition and location. This could include patterning to control wetting during deposition or on-chip in situ crystallization where nucleation sites are patterned over pores to conserve sample and increase hit rate. Higher repetition rate XFELs also provide compelling motivation for future fixed targets to employ a more slot-like window design that requires less accurate spatial synchronization with the X-ray pulse, much like the frameless approach recently demonstrated[63]. This also provides more potential sample area and therefore more possible shots per chip. Advances in analysis methodology to interpret data from multiple-crystal hits will further facilitate high sample loading[69]. Future iterations of chip design would ideally include implementation of microfluidics and/or electrodes for time resolved experiments using mixing or an applied electric field pulse to trigger interesting biological processes. Substrate patterning could also ensure sample/surface adhesion to facilitate future applications for time-resolved mixing experiments.

2.5 Acknowledgements and Funding Information

The authors would like to thank Rick Kurian (Arizona State University) for invaluable help with X-ray scattering calculations. This work was performed, in part, under the auspices of the U.S. Department of Energy by Lawrence Livermore National Laboratory under Contract DE-AC52-

07NA27344. The authors would like to thank the scientific staff at the MFX and CXI end stations of the Linac Coherent Light Source. The LCLS is a national user facility operated by Stanford University on behalf of the US Department of Energy and supported by the US Department of Energy Office of Science, Office of Basic Energy Sciences under Contract No. DE-AC02-76SF00515.

M.L.S., D.G., M.A.C. and M.F. were supported by the NIH grant 1R01GM117342-01. Support was also provided through the NSF-STC "BioXFEL" through award STC-1231306.

2.6 References

1 Spence John, C. H. & Chapman Henry, N. The birth of a new field†. *Philosophical Transactions of the Royal Society B: Biological Sciences* **369**, 20130309, doi:10.1098/rstb.2013.0309 (2014).

2 Feld, G. K. & Frank, M. Enabling membrane protein structure and dynamics with X-ray free electron lasers. *Current Opinion in Structural Biology* **27**, 69-78, doi:10.1016/j.sbi.2014.05.002 (2014).

3 Schlichting, I. Serial femtosecond crystallography: the first five years. *IUCrJ* **2**, 246-255, doi:10.1107/S205225251402702X (2015).

4 Johansson, L. C., Stauch, B., Ishchenko, A. & Cherezov, V. A Bright Future for Serial Femtosecond Crystallography with XFELs. *Trends in Biochemical Sciences* **42**, 749-762, doi:10.1016/j.tibs.2017.06.007 (2017).

5 Neutze, R., Wouts, R., Spoel, D. v. d., Weckert, E. & Hajdu, J. Potential for biomolecular imaging with femtosecond X-ray pulses. *Nature* **406**, 752, doi:10.1038/35021099 (2000).

6 Chapman, H. N. *et al.* Femtosecond X-ray protein nanocrystallography. *Nature* **470**, 73-77, doi:10.1038/nature09750 (2011).

7 Boutet, S. *et al.* High-Resolution Protein Structure Determination by Serial Femtosecond Crystallography. *Science* **337**, 362-364, doi:10.1126/science.1217737 (2012).

8 Seibert, M. M. *et al.* Single mimivirus particles intercepted and imaged with an X-ray laser. *Nature* **470**, 78-81, doi:10.1038/nature09748 (2011).

9 Sun, Z., Fan, J., Li, H. & Jiang, H. Current Status of Single Particle Imaging with X-ray Lasers. *Applied Sciences* **8**, 132, doi:10.3390/app8010132 (2018).

10 Pedrini, B. *et al.* 7 Å resolution in protein two-dimensional-crystal X-ray diffraction at Linac Coherent Light Source. *Phil. Trans. R. Soc. B* **369**, 20130500, doi:10.1098/rstb.2013.0500 (2014).

11 Frank, M. *et al.* Femtosecond X-ray diffraction from two-dimensional protein crystals. *IUCrJ* **1**, 95-100, doi:10.1107/S2052252514001444 (2014).

12 Casadei, C. M. *et al.* Resolution extension by image summing in serial femtosecond crystallography of two-dimensional membrane-protein crystals. *IUCrJ* **5**, 103-117, doi:10.1107/S2052252517017043 (2018).

13 Seuring, C. *et al.* Femtosecond X-ray coherent diffraction of aligned amyloid fibrils on low background graphene. *Nature communications* **9**, 1836 (2018).
14 Kirian, R. A. *et al.* Femtosecond protein nanocrystallography—data analysis methods. *Optics Express* **18**, 5713-5723, doi:10.1364/OE.18.005713 (2010).
15 Chavas, L. M. G., Gumprecht, L. & Chapman, H. N. Possibilities for serial femtosecond crystallography sample delivery at future light sources. *Structural Dynamics* **2**, 041709, doi:10.1063/1.4921220 (2015).
16 White, T. A. *et al.* Recent developments in CrystFEL. *Journal of Applied Crystallography* **49**, 680-689, doi:10.1107/S1600576716004751 (2016).
17 Yun, J.-H. *et al.* Non-cryogenic structure of a chloride pump provides crucial clues to temperature-dependent channel transport efficiency. *Journal of Biological Chemistry* **294**, 794-804, doi:10.1074/jbc.RA118.004038 (2019).
18 O'Sullivan, M. E. *et al.* Aminoglycoside ribosome interactions reveal novel conformational states at ambient temperature. *Nucleic Acids Research* **46**, 9793-9804, doi:10.1093/nar/gky693 (2018).
19 Audet, M. *et al.* Crystal structure of misoprostol bound to the labor inducer prostaglandin E 2 receptor. *Nature Chemical Biology* **15**, 11, doi:10.1038/s41589-018-0160-y (2019).
20 Dao, E. H. *et al.* Structure of the 30S ribosomal decoding complex at ambient temperature. *RNA* **24**, 1667-1676, doi:10.1261/rna.067660.118 (2018).
21 Stauch, B. *et al.* Structural basis of ligand recognition at the human MT 1 melatonin receptor. *Nature* **569**, 284, doi:10.1038/s41586-019-1141-3 (2019).
22 Martiel, I., Müller-Werkmeister, H. M. & Cohen, A. E. Strategies for sample delivery for femtosecond crystallography. *Acta Crystallographica Section D: Structural Biology* **75**, 160-177, doi:10.1107/S2059798318017953 (2019).
23 Weierstall, U. *et al.* Lipidic cubic phase injector facilitates membrane protein serial femtosecond crystallography. *Nature Communications* **5**, 3309, doi:10.1038/ncomms4309 (2014).
24 Nogly, P. *et al.* Lipidic cubic phase injector is a viable crystal delivery system for time-resolved serial crystallography. *Nature Communications* **7**, 12314, doi:10.1038/ncomms12314 (2016).
25 Fuller, F. D. *et al.* Drop-on-demand sample delivery for studying biocatalysts in action at X-ray free-electron lasers. *Nature Methods* **14**, 443-449, doi:10.1038/nmeth.4195 (2017).
26 Beyerlein, K. R. *et al.* Mix-and-diffuse serial synchrotron crystallography. *IUCrJ* **4**, 769-777, doi:10.1107/S2052252517013124 (2017).
27 Bogan, M. J. *et al.* Single Particle X-ray Diffractive Imaging. *Nano Letters* **8**, 310-316, doi:10.1021/nl072728k (2008).
28 Hantke, M. F. *et al.* High-throughput imaging of heterogeneous cell organelles with an X-ray laser. *Nature Photonics* **8**, 943-949, doi:10.1038/nphoton.2014.270 (2014).
29 Zarrine-Afsar, A. *et al.* Crystallography on a chip. *Acta Crystallographica Section D: Biological Crystallography* **68**, 321-323, doi:10.1107/S0907444911055296 (2012).
30 Feld, G. K. *et al.* Low-Z polymer sample supports for fixed-target serial femtosecond X-ray crystallography. *Journal of Applied Crystallography* **48**, 1072-1079, doi:10.1107/S1600576715010493 (2015).
31 Baxter, E. L. *et al.* High-density grids for efficient data collection from multiple crystals. *Acta Crystallographica Section D: Structural Biology* **72**, 2-11, doi:10.1107/S2059798315020847 (2016).

32 Hunter, M. S. *et al.* Fixed-target protein serial microcrystallography with an x-ray free electron laser. *Scientific Reports* **4**, 6026, doi:10.1038/srep06026 (2014).

33 Murray, T. D. *et al.* A high-transparency, micro-patternable chip for X-ray diffraction analysis of microcrystals under native growth conditions. *Acta Crystallographica. Section D, Biological Crystallography* **71**, 1987-1997, doi:10.1107/S1399004715015011 (2015).

34 Roedig, P. *et al.* A micro-patterned silicon chip as sample holder for macromolecular crystallography experiments with minimal background scattering. *Scientific reports* **5**, 10451 (2015).

35 Mueller, C. *et al.* Fixed target matrix for femtosecond time-resolved and in situ serial micro-crystallography. *Structural Dynamics* **2**, doi:10.1063/1.4928706 (2015).

36 Owen, R. L. *et al.* Low-dose fixed-target serial synchrotron crystallography. *Acta Crystallographica. Section D, Structural Biology* **73**, 373-378, doi:10.1107/S2059798317002996 (2017).

37 Oghbaey, S. *et al.* Fixed target combined with spectral mapping: approaching 100% hit rates for serial crystallography. *Acta Crystallographica Section D: Structural Biology* **72**, 944-955, doi:10.1107/S2059798316010834 (2016).

38 Ebrahim, A. *et al.* Dose-resolved serial synchrotron and XFEL structures of radiation-sensitive metalloproteins. *IUCrJ* **6**, 543-551, doi:10.1107/S2052252519003956 (2019).

39 Schulz, E. C. *et al.* The hit-and-return system enables efficient time-resolved serial synchrotron crystallography. *Nature Methods* **15**, 901-904, doi:10.1038/s41592-018-0180-2 (2018).

40 Sherrell, D. A. *et al.* A modular and compact portable mini-endstation for high-precision, high-speed fixed target serial crystallography at FEL and synchrotron sources. *Journal of Synchrotron Radiation* **22**, 1372-1378, doi:10.1107/S1600577515016938 (2015).

41 Sugahara, M. *et al.* Grease matrix as a versatile carrier of proteins for serial crystallography. *Nature Methods* **12**, 61-63, doi:10.1038/nmeth.3172 (2015).

42 Roedig, P. *et al.* Room-temperature macromolecular crystallography using a micro-patterned silicon chip with minimal background scattering. *Journal of Applied Crystallography* **49**, 968-975, doi:10.1107/S1600576716006348 (2016).

43 Roedig, P. *et al.* High-speed fixed-target serial virus crystallography. *Nature Methods* **advance online publication**, doi:10.1038/nmeth.4335 (2017).

44 Geim, A. K. & Novoselov, K. S. in *Nanoscience and Technology: A Collection of Reviews from Nature Journals* 11-19 (World Scientific, 2010).

45 Novoselov, K. S. *et al.* A roadmap for graphene. *nature* **490**, 192 (2012).

46 Wierman, J. L., Alden, J. S., Kim, C. U., McEuen, P. L. & Gruner, S. M. Graphene as a protein crystal mounting material to reduce background scatter. *Journal of Applied Crystallography* **46**, 1501-1507, doi:doi:10.1107/S002188981301786X (2013).

47 Sui, S. *et al.* Graphene-based microfluidics for serial crystallography. *Lab on a Chip* **16**, 3082-3096 (2016).

48 Li, X. *et al.* Transfer of Large-Area Graphene Films for High-Performance Transparent Conductive Electrodes. *Nano Letters* **9**, 4359-4363, doi:10.1021/nl902623y (2009).

49 Liang, X. *et al.* Toward clean and crackless transfer of graphene. *ACS nano* **5**, 9144-9153 (2011).

50 Barin, G. B. *et al.* Optimized graphene transfer: Influence of polymethylmethacrylate (PMMA) layer concentration and baking time on graphene final performance. *Carbon* **84**, 82-90 (2015).

51 Liang, M. *et al.* The Coherent X-ray Imaging instrument at the Linac Coherent Light Source. *Journal of Synchrotron Radiation* **22**, 514-519, doi:10.1107/S160057751500449X (2015).

52 Sierra, R. G. *et al.* The Macromolecular Femtosecond Crystallography Instrument at the Linac Coherent Light Source. *Journal of Synchrotron Radiation* **26**, 346-357, doi:10.1107/S1600577519001577 (2019).

53 Feld, G. K. *et al.* Structure and function of REP34 implicates carboxypeptidase activity in Francisella tularensis host cell invasion. *The Journal of Biological Chemistry* **289**, 30668-30679, doi:10.1074/jbc.M114.599381 (2014).

54 Lieske, J. *et al.* On-chip crystallization for serial crystallography experiments and on-chip ligand-binding studies. *IUCrJ* **6**, 714-728, doi:10.1107/S2052252519007395 (2019).

55 Roedig, P. *et al.* A micro-patterned silicon chip as sample holder for macromolecular crystallography experiments with minimal background scattering. *Scientific Reports* **5**, 10451, doi:10.1038/srep10451 (2015).

56 Schropp, A. *et al.* Full spatial characterization of a nanofocused x-ray free-electron laser beam by ptychographic imaging. *Scientific Reports* **3**, doi:10.1038/srep01633 (2013).

57 Blaj, G. *et al.* X-ray detectors at the Linac Coherent Light Source. *Journal of Synchrotron Radiation* **22**, 577-583, doi:10.1107/S1600577515005317 (2015).

58 Mariani, V. *et al.* OnDA: online data analysis and feedback for serial X-ray imaging. *Journal of Applied Crystallography* **49**, 1073-1080, doi:10.1107/S1600576716007469 (2016).

59 Barty, A. *et al.* Cheetah: software for high-throughput reduction and analysis of serial femtosecond X-ray diffraction data. *Journal of Applied Crystallography* **47**, 1118-1131, doi:10.1107/S1600576714007626 (2014).

60 White, T. A. *et al.* CrystFEL: a software suite for snapshot serial crystallography. *Journal of Applied Crystallography* **45**, 335-341, doi:10.1107/S0021889812002312 (2012).

61 Battye, T. G. G., Kontogiannis, L., Johnson, O., Powell, H. R. & Leslie, A. G. W. iMOSFLM: a new graphical interface for diffraction-image processing with MOSFLM. *Acta Crystallographica Section D: Biological Crystallography* **67**, 271-281, doi:10.1107/S0907444910048675 (2011).

62 Segelke, B. W., Feld, G.K., Corzett, M.H., Omattage, N.S., Rasley, A. X-ray structure of Francisella tularensis Rapid Encystment Protein 24 KDa (REP24), gene product of FTN_0841 FAU. *RCSb Protein Data Bank* (2014).

63 Doak, R. B. *et al.* Crystallography on a chip – without the chip: sheet-on-sheet sandwich. *Acta Crystallographica Section D: Structural Biology* **74**, 1000-1007, doi:10.1107/S2059798318011634 (2018).

64 Sui, S., Wang, Y., Dimitrakopoulos, C. & Perry, S. L. A Graphene-Based Microfluidic Platform for Electrocrystallization and In Situ X-ray Diffraction. *Crystals* **8**, 76, doi:10.3390/cryst8020076 (2018).

65 Sui, S. *et al.* Graphene-based microfluidics for serial crystallography. **16**, 3082-3096, doi:10.1039/C6LC00451B (2016).

66 Hura, G. *et al.* Water structure as a function of temperature from X-ray scattering experiments and ab initio molecular dynamics. *Physical Chemistry Chemical Physics* **5**, 1981-1991, doi:10.1039/B301481A (2003).

67 Schoonjans, T. *et al.* The xraylib library for X-ray–matter interactions. Recent developments. *Spectrochimica Acta Part B: Atomic Spectroscopy* **66**, 776-784, doi:10.1016/j.sab.2011.09.011 (2011).
68 Tolstikova, A. *et al.* 1 kHz fixed-target serial crystallography using a multilayer monochromator and an integrating pixel detector. *IUCrJ* **6**, 927-937, doi:10.1107/S205225251900914X (2019).
69 Beyerlein, K. R. *et al.* FELIX: an algorithm for indexing multiple crystallites in X-ray free-electron laser snapshot diffraction images. *Journal of Applied Crystallography* **50**, 1075-1083, doi:10.1107/S1600576717007506 (2017).

2.7 Supporting Information

Graphene film characterization using SEM-EDX

Scanning Electron Microscopy using Hitachi S-4100T FE-SEM and Energy Dispersive X-ray Spectroscopy using Oxford INCA Energy EDS were performed on a graphene film transferred to a silicon wafer to characterize film cleanliness, particularly to test for the complete removal of Nickel metal layer from the etching steps. EDX images confirm absence of any residual metal contamination as no peaks corresponding to Nickel are observed. (**Figure S1, S2**).

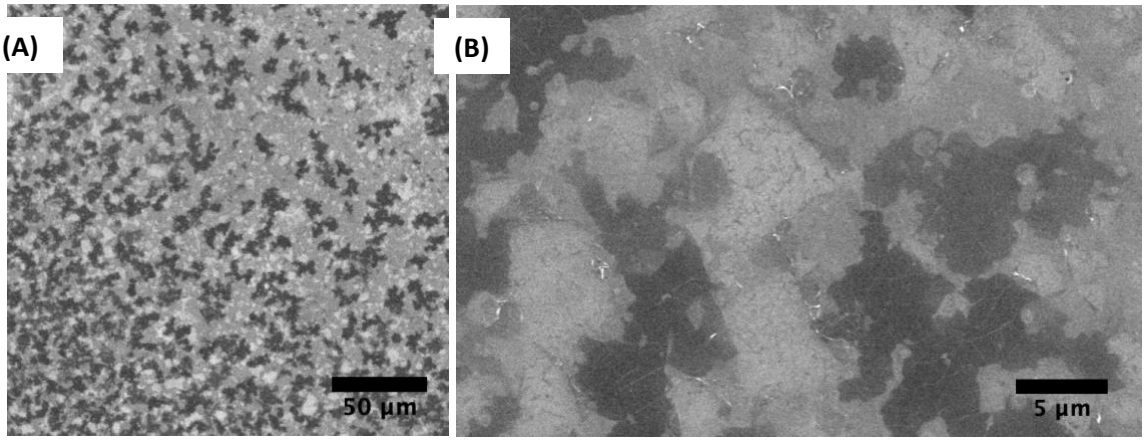

Figure S1: Scanning electron microscopy (SEM) images of few-layer graphene (FLG) transferred to a silicon wafer showing graphene domains with varying thickness at (A) 300X and (B) 3000X magnification.

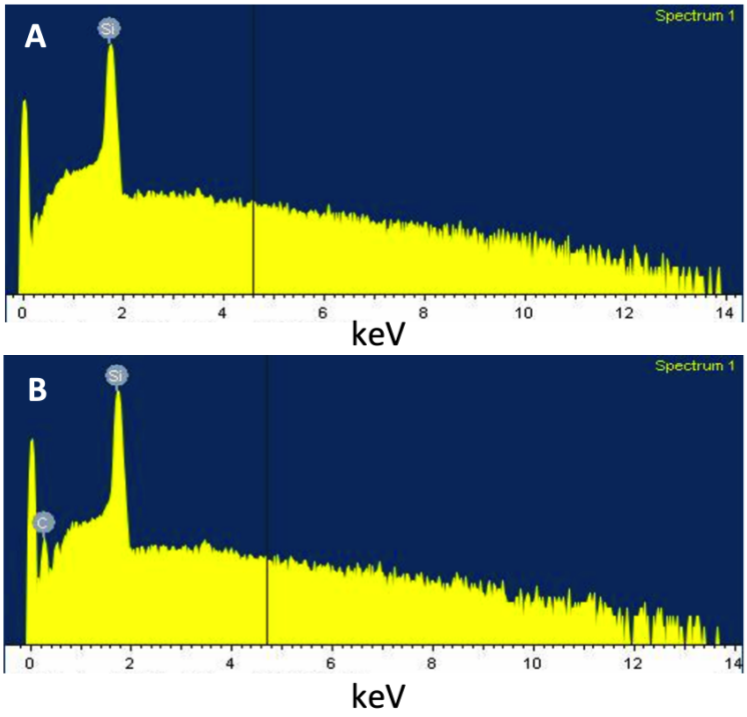

Element	Weight%
Si	100.00
Total	100.00

Element	Weight%
C	7.32
Si	92.68
Total	100.00

Figure S2: Energy dispersive x-ray spectroscopy (EDS) comparison of a (A) bare silicon wafer and (B) few-layer graphene coated silicon wafer confirms the absence of metal contaminants on the graphene surface from the etching steps.

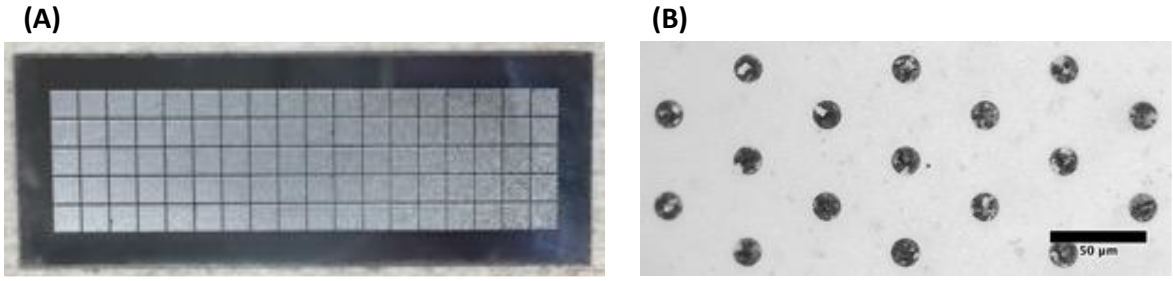

Figure S3: (A) Design of the micropatterned Finnlitho silicon chip with dimensions 32.7 mm x 12 mm. Lighter regions (5 x 18 array) correspond to thinned silicon bearing the hexagonal pore pattern. (B) Optical microscopy image showing the hexagonal pore pattern in a Finnlitho chip covered with a FLG-PMMA film. The graphene films consist of multilayer grains of varying thickness, thicker grains with 6-7 layers of graphene appear as irregular blotches.

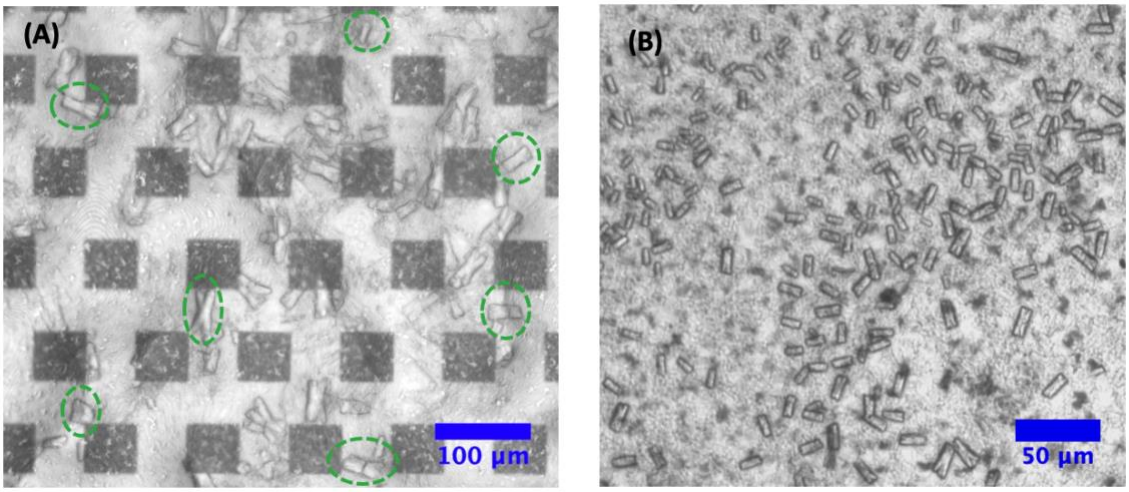

Figure S4: REP24 crystals (A) sandwiched between two few-layer graphene-PMMA hybrid films after 30 minutes in a benchtop vacuum oven at room temperature and (B) deposited on a graphene surface, showing randomly oriented crystal configurations.

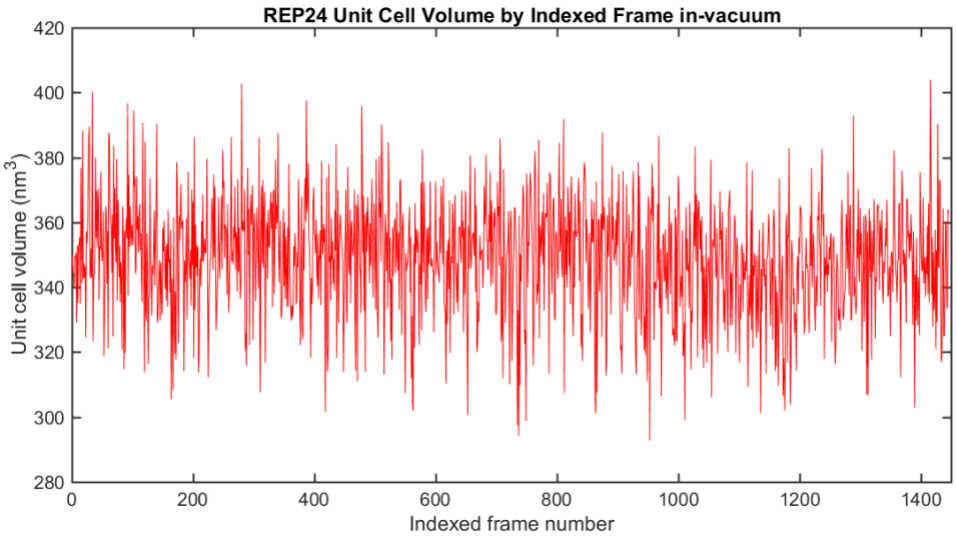

Figure S5: Unit cell volume calculated from unit cell parameters generated by frame-by-frame indexing of REP24 SFX data. These data were collected on REP24 microcrystals encapsulated within the polymer/graphene sandwich and measured in-vacuum over approximately 20 minutes.

2.8 Appendix

2.8.1 Model lipid membrane assemblies for membrane protein crystallography at XFELs

Project background

Integral membrane proteins (IMPs) account for approximately 25% of all proteins in a cell.[1] Embedded in the cell membrane, these play an important role in molecular recognition, material transport, signal transduction, and cell adhesion to mention a few. Due to their amphipathic structure, a cell membrane-mimetic environment is essential for proper structure and function retention, making these proteins notoriously difficult to crystallize (<1% of all PDB structures). IMPs are more likely to form 2D crystals rather than 3D crystals, which limits the possibility of obtaining their molecular structures using the standard methods of protein crystallography.[2] While cryo-electron microscopy has traditionally been used to obtain static structures of IMPs[3,4], XFELs open up avenues to study room-temperature structures and dynamics using micro-focused X-ray beams with brilliant, femtosecond pulses.[5] The goal of this work was to evaluate the feasibility of high-resolution diffraction data collection from these weakly-diffracting 2D objects (Z-height <10 nm) using XFELs.

Lipid monolayers at the air-water interface and solid supported lipid bilayers can be used to incorporate IMPs into a native-like lipid environment for subsequent 2D crystallization, paving the way for a generalized tool for IMP crystallography.[6–8] In this work, we produced high density 2D crystals of soluble proteins streptavidin (SA) and cholera toxin (CT) using lipid monolayers and bilayers containing biotinylated lipids and ganglioside GM_1 respectively, to serve as a model for IMP crystals, schematic shown in **Figure A1(a)**. In the form of 2D crystals, SA could be a very useful tool for templating any other protein (in biotinylated form) in an ordered array for structural studies.[9–11] The 2D nature of these crystals necessitated the use of fixed-target sample delivery methods. Ultra-low background PMMA-FLG supports or sandwiched enclosures on silicon fixed-targets were used to keep the samples stable/hydrated during XFEL measurements in the CXI vacuum environment (LCLS). The unique feature of having a single molecular layer of the protein

makes the opposing side free for interaction. The milieu around proteins in a 2D crystals can be changed and varied more freely than in a 3D crystal, albeit with very strict conditions for its integrity. Thus, 2D protein crystallography provides an important avenue for obtaining dynamic structural information by allowing visualization of rapid conformational change.

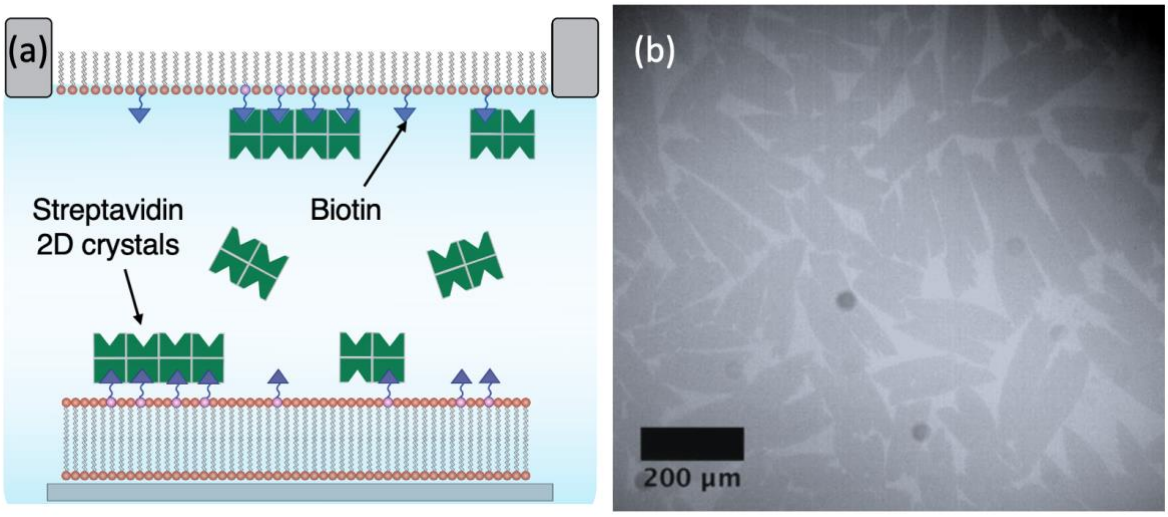

Figure A1: (a) A schematic of 2D streptavidin crystallization at lipid monolayers or bilayer with biotinylated lipids. (b) Fluorescence microscopy images of streptavidin 2D crystals grown at the air-water interface.

Sample preparation and characterization

Crystallization at the air-water interface

Delrin wells (35mm x 15mm x 4mm, with inlet holes) were machined to match the dimensions of the silicon fixed-target Roadrunner chips and filled with ~1.6 mL of crystallization buffer.

Streptavidin (SA): SA homo-tetramers have an extraordinarily high affinity for biotin, a very small (244 Da) highly specific ligand for SA. Following previous work on crystallization using lipid monolayers[12–16], we optimized our crystallization procedure to maximize the area of crystal coverage. Briefly, a Langmuir monolayer was formed by depositing 9-10 µL of 0.1 mg/mL lipid mixture (1:10 w/w Biotin-X-DHPE: DOPC in 1:1 chloroform: hexane) at the air-water interface

over the crystallization buffer subphase (10mM HEPES, 250mM NaCl, 10mM EDTA, pH 7.8) to produce a surface pressure of ~25-30 mN/m. The SA protein solution was injected into the subphase to a final concentration of ~20 µg/mL. 200-300 µm crystals first appeared after an incubation period of ~ 4 hours and grew to confluence after 12 hours. **Figure 1(b)** shows fluorescence microscopy images of X/H shaped 2D crystals of streptavidin at the air-water interface, 5 mol% FITC-Avidin (does not crystallize) was used for visualization of crystals.

Cholera toxin (CT): The cholera toxin is an oligomeric complex made up of six protein subunits: a single copy of the A subunit (part A, enzymatic), and five copies of the B subunit (part B, receptor binding), denoted as AB_5.[17–19] A similar Langmuir-monolayer based approach was used to crystallize CT which has a high binding affinity for GM_1 ganglioside lipid. 10mM Tris, 150 mM NaCl, pH 7.3 was used as the crystallization buffer subphase and 0.1mg/ml 1:9 GM_1:DOPE or DPPE was used as the lipid spreading solution. Crystals appeared after 12-36 hours. CT did not produce crystals large enough to be visualized via fluorescence microscopy.

Transfer of crystals to transmission electron microscopy (TEM) grids and XFEL substrates: Following crystallization, glutaraldehyde was injected into the subphase at 0.5 v/v% for crystal fixation and the samples were incubated for 3-4 hours to provide stability during the transfer process.[20] The Langmuir-Schaffer method[21] was used to transfer 2D crystals to carbon-coated 300-mesh TEM grids and large-area graphene-polymer XFEL fixed target substrates. The substrates were raised crystal-side up through the air-water interface, the excess solution was blotted, and the sample was stained using 2% phosphotungstic acid (PTA) negative stain for 1 min. TEM imaging was carried out using a JEOL 2100F transmission electron microscope. **Figure A2** shows transmission electron micrographs of streptavidin and cholera toxin with a fast Fourier transform (FFT) inset showing Bragg spots indicative of crystalline order.

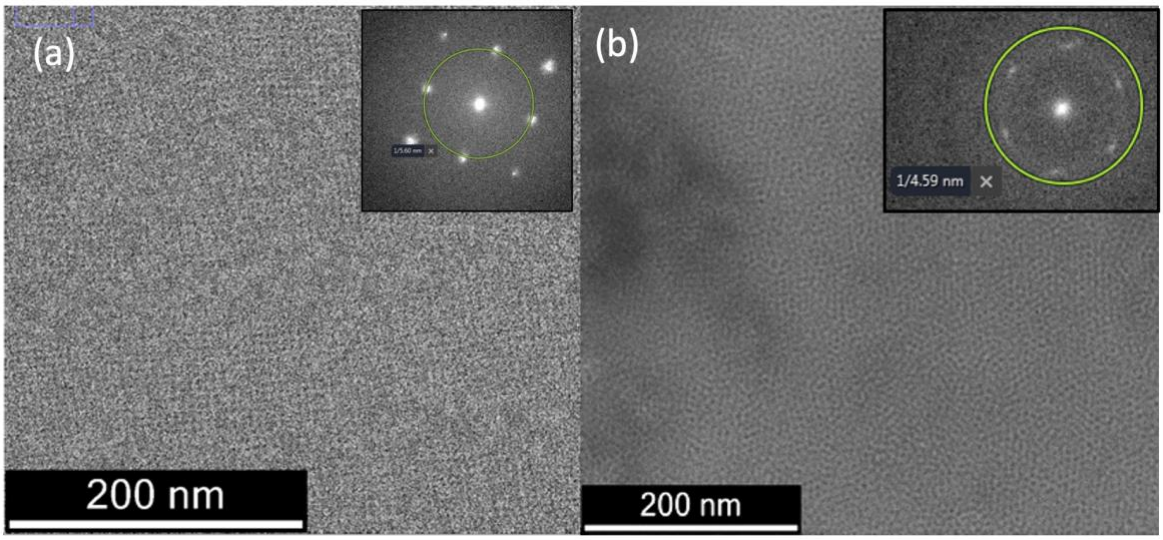

Figure A2: TEM image of crystals transferred to carbon coated TEM grid, (a) streptavidin, inset: Fast Fourier transform (FFT) indicates C222 symmetry lattice of SA crystals; (b) cholera toxin, inset: FFT indicates hexagonal lattice of CT crystals.

Crystals transferred to the fixed-target chip were kept submerged and the Delrin well was transferred to a large crystallization dish filled with buffer. A second graphene-polymer sandwiching film was floated to the air-water interface. The substrate was carefully raised through the interface crystal side up at a 45-degree angle to sandwich the sample with a second graphene-polymer layer to retain a minimal thickness water hydration layer. **Figure A3(a)** shows fluorescence microscopy images of graphene sandwiched 2D SA crystals on fixed-target chips. Samples were used for XFEL characterization within 30 minutes of sample preparation. For XFEL samples that were stained, or sugar embedded, the chip was carefully raised from the crystallization dish at an angle (without sandwiching layer) to remove all water, 2 wt.% PTA stain or glucose solution was applied to the sample.

XFEL characterization

SFX experiments were conducted at an X-ray energy of 7.5 keV with a beam size of 120 nm x170 nm full width half maximum (FWHM) at CXI[22]. During each sample scan, chips were translated

through the beam at the full 120 Hz repetition rate of LCLS (pulse duration ~40 fs) such that the X-ray pulse arrival was synchronized spatially with the patterned micropores, and diffraction images were recorded shot-by-shot by a Cornell-SLAC Pixel Array Detector (CSPAD)[23]. The design and operation of the Roadrunner fast scanning system is described in detail elsewhere[24–26]. The samples were measured with between 3% and 10% beam transmission rather than the full X-ray flux of 4.5 mJ/pulse due to concerns regarding damage to the chip resulting from the lower intensity "wings" of the X-ray beam around the central focus spot (~1% of the total intensity). X-ray images were analyzed in near real-time for an estimation of hit rate using OnDA[27]. Cheetah[28] was used to find crystal hits.

A hit rate of ~30% was obtained with negatively stained SA crystals with typical hits showing Bragg spots to 7-8 Å resolution with diffuse scatter ~ 5 Å, **Figure A3(b).** A significantly lower hit rate of <5 % was obtained with sugar embedded and sandwiched samples with weaker diffraction signal from hits. The 2D nature of these crystals imparts stringing restrictions on the planarity of the sample, with significant loss of crystalline order upon disruption in the Z-direction. Direct crystal growth on lipid bilayers was explored next to mitigate crystal handling steps to minimize stresses on the sample.

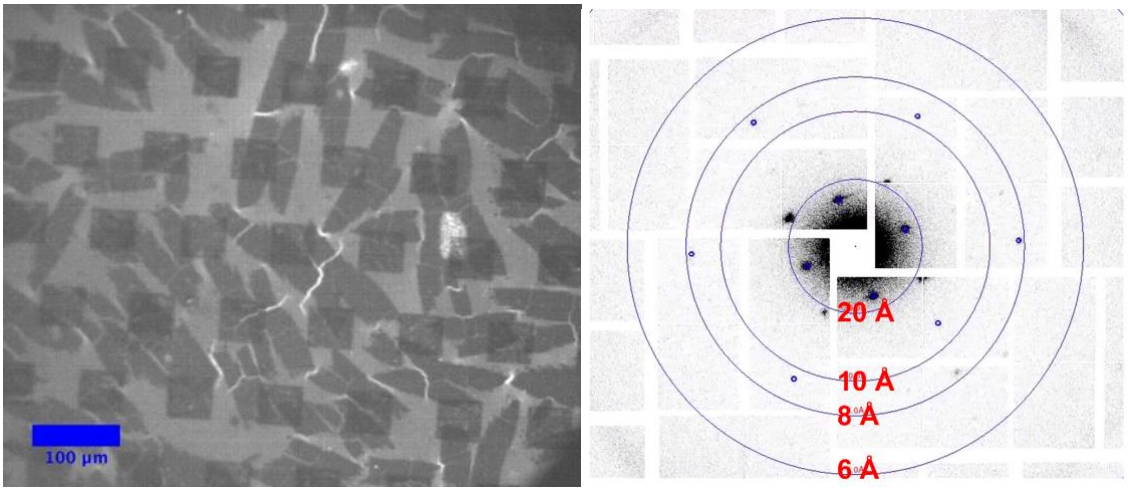

Figure A3: (a) X and H shaped Streptavidin 2D crystals transferred to a graphene-polymer coated silicon fixed-target chip with 50 µm pyramidal pores sandwiched with a second enclosing film. (b) A typical "hit" from a negatively stained SA 2D crystal sample showing diffraction to ~ 8 Å with some diffuse scatter at higher resolutions.

Crystal growth on lipid bilayers

Lipid bilayers: Lipid bilayers were produced using the Langmuir-Blodgett technique[21] on smooth, hydrophilic surfaces (mica/ UV-ozone treated polymer films) using an inner DPPE leaflet (35 mN/m) and an outer leaflet comprising of 2:97.5:0.5 w/w Biotin-X-DHPE: DTPC: Texas Red-DHPE (35 mN/m). The fluorescent dye labelled lipid enabled assessment of membrane fluidity. The bilayers were transferred to a crystallizing dish containing the buffer solution and the solution was spiked with pure DTPC to prevent lipid desorption from the bilayer surface. 1:9 FITC-SA:SA was added at a concentration of 15-20 µg/mL. **Figure A4(a,b)** shows fluorescence microscopy images of the supported lipid bilayer through the Texas Red filter cube (a) before and (b) after SA crystallization. **Figure A4(c)** shows fluorescence microscopy images of the supported lipid bilayer with dendritic SA crystals through the FITC-filter cube, as reported previously[29,30]. Similar attempts at growing 2D crystals on lipid monolayer deposited on hydrophobic polymer surfaces or on lipid bilayers deposited on hydrophilized polymer surfaces did not result in the growth of 2D

crystals suggesting that high degree of surface smoothness was critical for growth of 2D crystals.

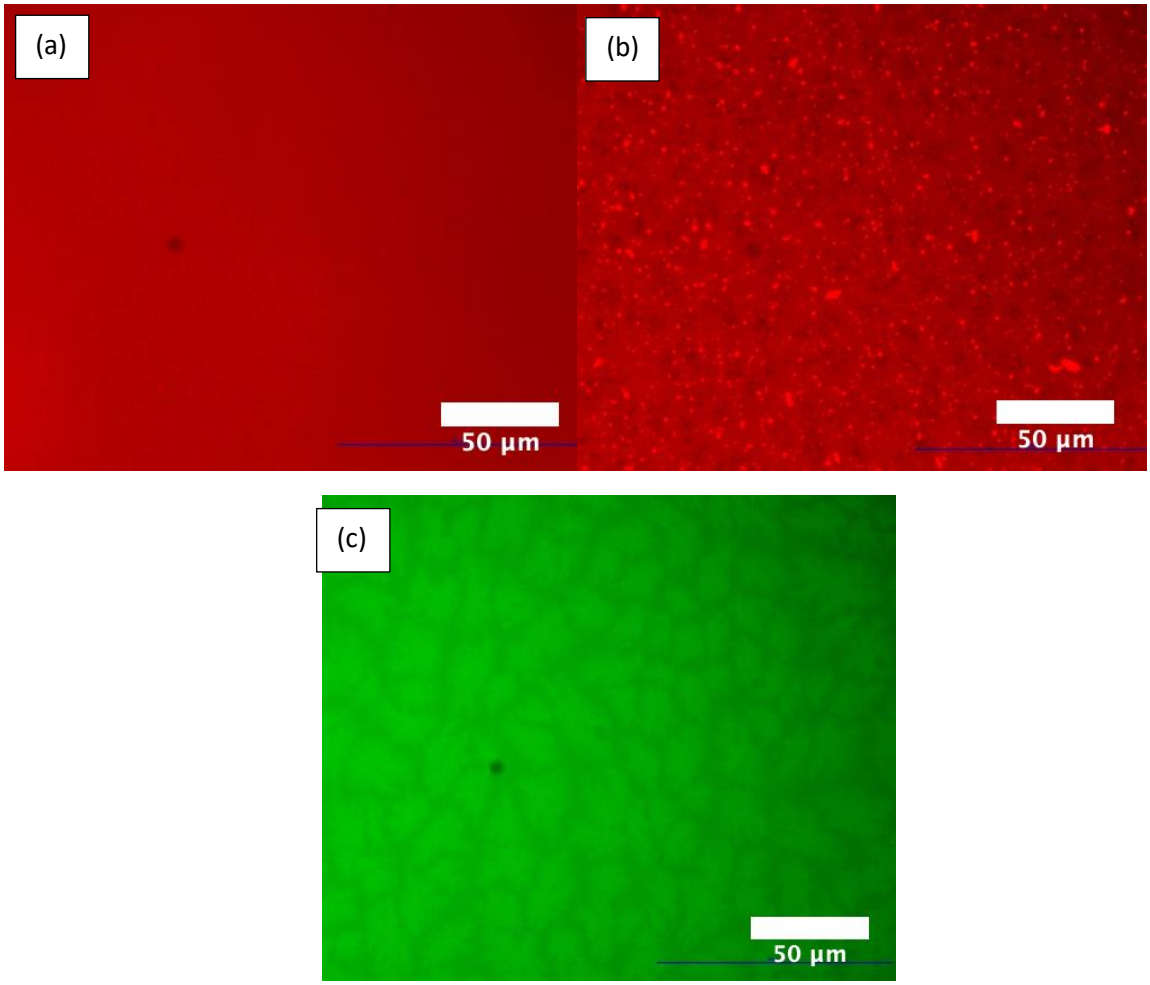

Figure A4: A supported lipid bilayer deposited on mica with an inner and outer leaflet comprising of pure DPPE and 2:97.5:0.5 w/w Biotin-X-DHPE: DTPC: Texas Red-DHPE, respectively. The bilayer viewed through the Texas-Red filter cube (a) before SA crystallization (b) after SA crystallization, viewed through the FITC filter cube (c) after SA crystallization.

SI References

1. Scherer, S., Arheit, M., Kowal, J., Zeng, X. & Stahlberg, H. Single particle 3D reconstruction for 2D crystal images of membrane proteins. *J. Struct. Biol.* **185**, 267–277 (2014).
2. Carpenter, E. P., Beis, K., Cameron, A. D. & Iwata, S. Overcoming the challenges of membrane protein crystallography. *Curr. Opin. Struct. Biol.* **18**, 581–586 (2008).
3. Braun, T. & Engel, A. Two-dimensional Electron Crystallography. in *Encyclopedia of Life Sciences* (ed. John Wiley & Sons, Ltd) a0003044 (John Wiley & Sons, Ltd, 2005). doi:10.1038/npg.els.0003044.

4. Scherer, S. *et al.* 2dx_automator: Implementation of a semiautomatic high-throughput high-resolution cryo-electron crystallography pipeline. *J. Struct. Biol.* **186**, 302–307 (2014).
5. Chapman, H. N. *et al.* Femtosecond X-ray protein nanocrystallography. *Nature* **470**, 73–77 (2011).
6. Czajkowsky, D. M., Sheng, S. & Shao, Z. Staphylococcal α-hemolysin can form hexamers in phospholipid bilayers 1 1Edited by W. Baumeister. *J. Mol. Biol.* **276**, 325–330 (1998).
7. Lévy, D. *et al.* Two-Dimensional Crystallization on Lipid Layer: A Successful Approach for Membrane Proteins. *J. Struct. Biol.* **127**, 44–52 (1999).
8. Dang, A. T., He, W., Ivey, D. B., Coleman, M. A. & Kuhl, T. L. Lipid and Protein Transfer between Nanolipoprotein Particles and Supported Lipid Bilayers. *Langmuir* **35**, 12071–12078 (2019).
9. Crucifix, C., Uhring, M. & Schultz, P. Immobilization of biotinylated DNA on 2-D streptavidin crystals. *J. Struct. Biol.* **146**, 441–451 (2004).
10. Wang, L., Ounjai, P. & Sigworth, F. J. Streptavidin crystals as nanostructured supports and image-calibration references for cryo-EM data collection. *J. Struct. Biol.* **164**, 190–198 (2008).
11. Han, B.-G. *et al.* Long shelf-life streptavidin support-films suitable for electron microscopy of biological macromolecules. *J. Struct. Biol.* **195**, 238–244 (2016).
12. Edwards, T. C. *et al.* Molecular Basis for Ionic Strength Dependence and Crystal Morphology in Two-Dimensional Streptavidin Crystallization. *Langmuir* **14**, 4683–4687 (1998).
13. Schief, W. R. *et al.* Two-dimensional crystallization of streptavidin: in pursuit of the molecular origins of structure, morphology, and thermodynamics. *Biomol. Eng.* **16**, 29–38 (1999).
14. Yatcilla, M. T., Robertson, C. R. & Gast, A. P. Influence of pH on Two-Dimensional Streptavidin Crystals. *Langmuir* **14**, 497–503 (1998).
15. Wang, S.-W., Robertson, C. R. & Gast, A. P. Molecular Arrangement in Two-Dimensional Streptavidin Crystals. *Langmuir* **15**, 1541–1548 (1999).
16. Yamamoto, D., Nagura, N., Omote, S., Taniguchi, M. & Ando, T. Streptavidin 2D Crystal Substrates for Visualizing Biomolecular Processes by Atomic Force Microscopy. *Biophys. J.* **97**, 2358–2367 (2009).
17. Ludwig, D. S., Ribi, H. O., Schoolnik, G. K. & Kornberg, R. D. Two-dimensional crystals of cholera toxin B-subunit-receptor complexes: projected structure at 17-A resolution. *Proc. Natl. Acad. Sci.* **83**, 8585–8588 (1986).
18. Ribi, H. O., Ludwig, D. S., Mercer, K. L., Schoolnik, G. K. & Kornberg, R. D. Three-Dimensional Structure of Cholera Toxin Penetrating a Lipid Membrane. *Science* **239**, 1272–1276 (1988).
19. Mosser, G. & Brisson, A. Structural analysis of two-dimensional arrays of cholera toxin b-subunit. *J. Electron Microsc. Tech.* **18**, 387–394 (1991).
20. Kubalek, E. W., Kornberg, R. D. & Darst, S. A. Improved transfer of two-dimensional crystals from the air/water interface to specimen support grids for high-resolution analysis by electron microscopy. *Ultramicroscopy* **35**, 295–304 (1991).
21. Kurniawan, J., Ventrici de Souza, J. F., Dang, A. T., Liu, G. & Kuhl, T. L. Preparation and Characterization of Solid-Supported Lipid Bilayers Formed by Langmuir–Blodgett Deposition: A Tutorial. *Langmuir* **34**, 15622–15639 (2018).
22. Schropp, A. *et al.* Full spatial characterization of a nanofocused x-ray free-electron laser beam by ptychographic imaging. *Sci. Rep.* **3**, 1633 (2013).
23. Blaj, G. *et al.* X-ray detectors at the Linac Coherent Light Source. *J. Synchrotron Radiat.* **22**, 577–583 (2015).
24. Roedig, P. *et al.* A micro-patterned silicon chip as sample holder for macromolecular crystallography experiments with minimal background scattering. *Sci. Rep.* **5**, 10451 (2015).
25. Roedig, P. *et al.* Room-temperature macromolecular crystallography using a micro-patterned silicon chip with minimal background scattering. *J. Appl. Crystallogr.* **49**, 968–975 (2016).
26. Roedig, P. *et al.* High-speed fixed-target serial virus crystallography. *Nat. Methods* **14**, 805–810 (2017).
27. Mariani, V. *et al. OnDA* : online data analysis and feedback for serial X-ray imaging. *J. Appl. Crystallogr.* **49**, 1073–1080 (2016).

28. Barty, A. *et al. Cheetah* : software for high-throughput reduction and analysis of serial femtosecond X-ray diffraction data. *J. Appl. Crystallogr.* **47**, 1118–1131 (2014).
29. Horton, M. R., Reich, C., Gast, A. P., Rädler, J. O. & Nickel, B. Structure and Dynamics of Crystalline Protein Layers Bound to Supported Lipid Bilayers. *Langmuir* **23**, 6263–6269 (2007).
30. Lou, C., Wang, Z. & Wang, S.-W. Two-Dimensional Protein Crystals on a Solid Substrate: Effect of Surface Ligand Concentration. *Langmuir* **23**, 9752–9759 (2007).

CHAPTER 3: PLUG AND PLAY POLYMER MICROFLUIDIC CHIPS FOR HYDRATED, ROOM-TEMPERATURE FIXED-TARGET SERIAL CRYSTALLOGRAPHY.

Deepshika Gilbile[1], Megan L. Shelby[2], Artem Y. Lyubimov[3], Jennifer L. Wierman[3], Diana C. F. Monteiro[4], Aina E. Cohen[3], Silvia Russi[3], Matthew A. Coleman[2,5], Matthias Frank[2,6], and Tonya L. Kuhl[1].

1. Department of Chemical Engineering, University of California at Davis, Davis, CA 95616, USA; 2. Biosciences and Biotechnology Division, Lawrence Livermore National Laboratory, Livermore, CA 94550, USA; 3. Stanford Synchrotron Radiation Lightsource, SLAC National Accelerator Laboratory, Menlo Park, CA 94025; 4. Hauptman-Woodward Medical Research Institute, 700 Ellicott Street, Buffalo, New York 14203, USA; 5. Department of Radiation Oncology, School of Medicine, University of California at Davis, Sacramento, CA 95817, USA; 6. Department of Biochemistry and Molecular Medicine, School of Medicine, University of California at Davis, Sacramento, CA 95817, USA.

Author Contributions

Conceptualization, D.G., T.L.K., M.L.S., M.F., M.A.C.; polymer microfluidic chip design and preparation, D.G., T.L.K.; sample preparation and crystallization, D.G., M.L.S. D.C.F.M.; data evaluation and analysis, D.G, M.L.S., A.Y.L.; instrument operation for SOX experiments at SSRL, J.L.W., A.E.C., S.R.; writing, D.G., M.L.S., A.Y.L, D.C.F.M., T.L.K., M.A.C., M.F. All authors have read and agreed to the published version of the manuscript.

Status: Submitted, awaiting peer review

Keywords: X-ray crystallography; synchrotrons; sample delivery; fixed-targets; cyclic olefin copolymer (COC); microfluidics; serial crystallography (SX); room temperature.

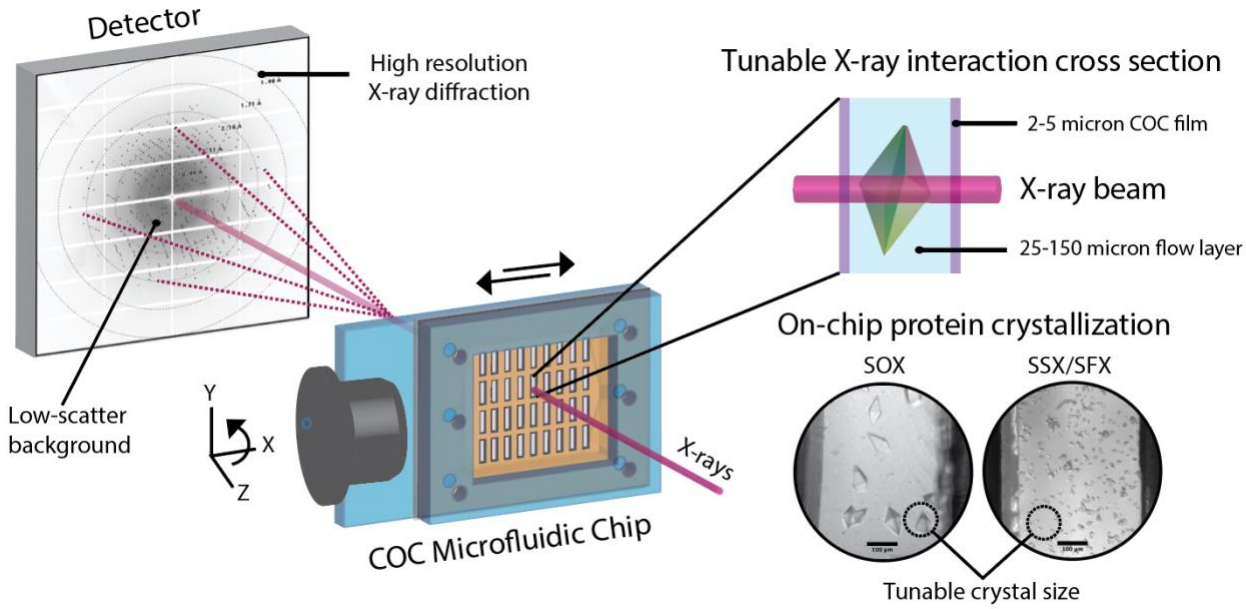

Abstract:

The practice of serial X-ray crystallography (SX) depends on efficient, continuous delivery of hydrated protein crystals while minimizing background scattering. Of the two major types of sample delivery devices, fixed-target devices offer several advantages over widely adopted jet injectors, including: lower sample consumption, clog-free delivery, and the ability to control on-chip crystal density to improve hit rates. Here we present our development of versatile, inexpensive, and robust polymer microfluidic chips for routine and reliable room-temperature serial measurements at both synchrotrons and X-ray free electron lasers (XFELs). Our design includes highly X-ray-transparent enclosing thin film layers tuned to minimize scatter background, adaptable sample flow layers tuned to match crystal size, and a large sample area compatible with both raster scanning and rotation based serial data collection. The optically transparent chips can be used both for *in situ* protein crystallization (to eliminate crystal handling) or crystal slurry

loading, with prepared samples stable for weeks in a humidified environment and for several hours in ambient conditions. Serial oscillation crystallography, using a multi-crystal rotational data collection approach, at a microfocus synchrotron beamline (SSRL, beamline 12-1) was used to benchmark the performance of the chips. High-resolution structures (1.3-2.7 Å) were collected from five different proteins- hen egg white lysozyme, thaumatin, bovine liver catalase, concanavalin-A (type VI), and SARS-CoV-2 nonstructural protein NSP5. Overall, our modular fabrication approach enables precise control over the cross-section of materials in the X-ray beam path and facilitates chip adaption to different sample and beamline requirements for user-friendly, straightforward diffraction measurements at room temperature.

3.1 Introduction

As a result of continued developments in the field of X-ray crystallography, the number of X-ray structures deposited annually in the Protein Data Bank (rcsb.org) has continued to increase rapidly from 135 in 1990 to 11234 in 2020. Alongside the rise of cryo-crystallography[1], these include improvements in crystallization methods[2], approaches to high throughput screening[3], and the emergence of highly brilliant, microfocus synchrotron beamlines enabling the collection of data from ever smaller crystals.[4,5] Meanwhile, the development of femtosecond XFELs has ushered in a new era of structural biology, with radiation damage-free data collection made possible at room temperature (RT) using serial femtosecond crystallography (SFX), due to the diffraction before destruction principle.[6–8] While single crystal cryogenic measurements continue to be the workhorse of macromolecular crystallography, technological development to support XFEL experiments has elicited a resurgence of interest in RT data collection at synchrotron facilities in recent years, with the parallel appearance of serial synchrotron crystallography (SSX) and serial oscillation crystallography (SOX) methods. In contrast with cryo measurements, RT synchrotron

studies are advantageous because they eliminate the need to screen cryoprotectants and freeze samples.[9] Importantly, measurements at RT have opened avenues to study not just static structures but also protein dynamics over a broad time-range, from picosecond to seconds, using time-resolved measurements. This new frontier in capabilities is paving the path for making molecular movies involving ligand binding, photoactivation, and catalysis to better understand dynamic structure-function relationships but requires facile and functional sample delivery.[10–14]

The high intensity of 3rd and 4th generation microfocus X-ray beamlines, fast onset of radiation damage at RT, and the use of microcrystals limit the number of high-resolution diffraction frames that can be collected from a single crystal. To address this limitation, serial crystallography (SX) can be used, where data from multiple crystals is combined.[6,15,16] For SOX, in which small rotation wedges (1-20°) are collected from small crystals (~10s of μm in size), data from tens to hundreds of crystals is typically sufficient.[17] For SSX or SFX, each diffraction volume is exposed only once and diffraction data from thousands of crystals is often required to obtain a complete dataset with high redundancy and good signal-to-noise at high resolution.[15,18] In most cases, these techniques require a much larger amount of crystalline material than conventional crystallography, using crystals that may be too small to successfully mount using conventional cryo-loops. This necessitates the development of specialized crystal delivery methods which are continuous, robust, and keep the crystals hydrated over the course of the measurement. Therefore, an optimal sample delivery platform should: (1) maintain crystal quality and hydration by minimizing sample stresses during sample preparation, characterization, and delivery; (2) minimize scatter contribution from the delivery device and excess buffer surrounding crystals; (3) optimize crystal density and crystal size to the beam and data collection requirements; (4) allow efficient use of beamtime by minimizing down time (e.g. from clogging or sample alignment for

rastering) with fast/automated sample changes (e.g. sample preparation in advance); and (5) allow experiments to probe structural dynamics by allowing different triggering methods.[19,20] Various sample delivery approaches have been proposed and demonstrated including liquid-jets[21–24], droplet-on-demand tape drives[25,26], and fixed-target devices[27–32]. The work presented here focuses on a new fixed-target platform for SOX or SSX/SFX. Fixed-target devices are advantageous compared to other approaches because they require very low sample volumes. Our novel geometries are compatible with *in situ* crystal growth which eliminates crystal handling and enable tuning of crystal densities and sizes to achieve high hit rates and high-quality diffraction images. Furthermore, they allow for the use of non-jetable crystal morphologies, like needles or plates, or crystals of heterogeneous size. They can also be used to facilitate dynamic experiments using stimuli like electric fields gradients, temperature jumps, pH gradients, ligand exchange and photo-activation.

For fixed targets, the choice of construction materials and fabrication strategy are important considerations as they significantly impact the cost, fragility, and stability of the devices. Several materials such as low-Z polymers (COC, PMMA, PDMS, Kapton, Mylar, epoxies), silicon, silicon nitride, glass and quartz have been used to make devices that balance these attributes with the measurement requirements. The two most common design formats are (1) microgrids and (2) microfluidic chips. Microgrids are chips with a 2D array of micropatterned holes for crystal entrapment upon deposition, sometimes used with thin films supports (0.1-10 μm) to improve sample retention and/or protect against dehydration.[17,27–30,33–46] These chips can offer advantages of high hit-rates and ultra-low background if wicking or vacuum application is used to localize crystals into pores and remove excess crystallization solution, but the exposed sample (even with sandwiching thin films) is sensitive to dehydration, requiring sample preparation and assembly

shortly before measurements (< 1-2 hours). Microfluidic chips, on the other hand, are enclosed devices offering precise control over sample volume and thickness, long-term stability against evaporation, and *in situ* crystal growth to eliminate crystal handling. But, the thick flow channels (25-300 μm) and capping layers (25-600 μm) often used to construct these devices contribute significantly to background scatter.[18,47–58] While several such devices have demonstrated high resolution data collection from large, well-ordered protein crystals, for many proteins obtaining large crystals often proves intractable. In the case of these small or weakly-diffracting microcrystals (desired for SX), the X-ray attenuation and scatter background from typical microfluidic chips can limit the resolution attained. Therefore, there is a need for the development of novel fixed targets with the stability and ease-of-use of microfluidic approaches, that are inexpensively fabricated and easily modified to match different sample and beamline requirements, while maintaining the advantages of high hit-rates and low background of microgrid approaches.

In this paper we describe the design of polymer fixed-target chips that address this need, for routine and reliable RT SOX and SSX/SFX experiments. The polymer materials used were selected for low water permeability, high X-ray transparency and high optical transparency (for on-chip imaging and light triggering of structural changes for future time-resolved structural studies). A modular, layered fabrication process enabled control over the cross section of materials in the beam path and easy design modification or adaption to different sample and beamline requirements. The chip is compatible with in situ crystallization using micro-batch and vapor diffusion methods. Pilot X-ray data collection with the chips was performed using SOX. The robustness and versatility of the chips was demonstrated, showing that they allow long-term storage, stability, easy transportation, and straightforward on-chip crystallization to diffraction

measurements. Preliminary results also indicate that the chip is amenable for SFX measurements without further alteration.

3.2 Materials and methods

A layered assembly process was used to construct the polymer microfluidic chip from hot-embossed COC supports, spin-coated COC thin films, laser-cut PMMA frames, and an adhesive sample flow layer. Five proteins (hen egg white lysozyme, thaumatin, bovine liver catalase, concanavalin-A, and SARS-CoV-2 nonstructural protein NSP5) were crystallized *in situ* and diffraction data directly collected on-chip at RT at beamline 12-1 at SSRL. The minimum beam spot size was 55 μm x 5 μm (X-Y, FWHM) and a SOX data collection approach was used to benchmark the performance of the chip.

3.2.1 Microfluidic chip fabrication and assembly

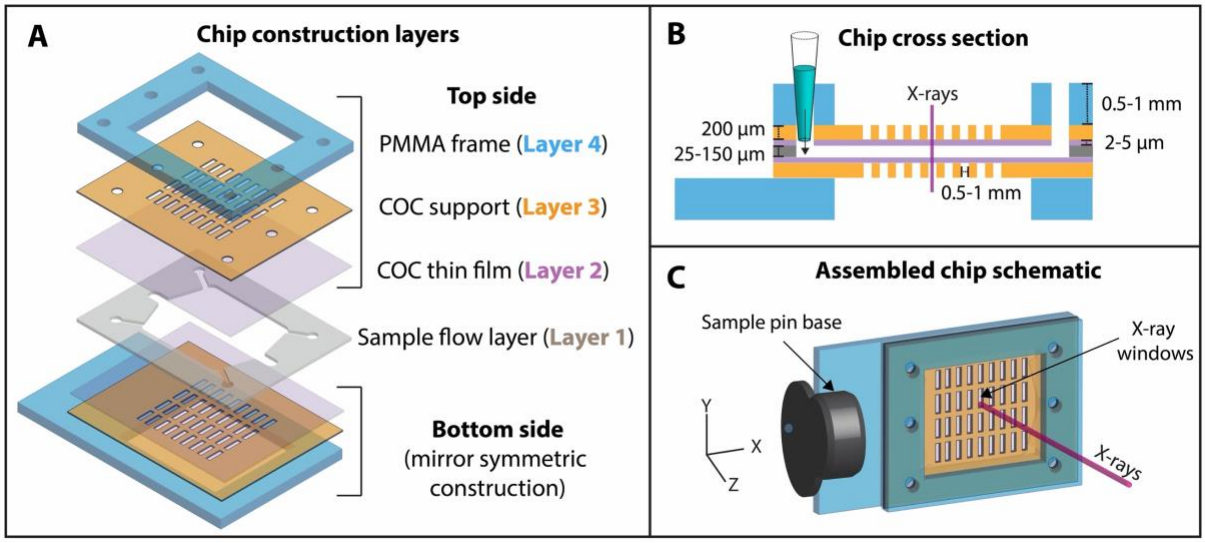

Figure 1: A schematic of (A) the different construction layers used to assemble the polymer microfluidic chip; (B) the cross-section view showing the different layer thicknesses; and (C) the final assembled chip.

A schematic of the chip construction layers, and the final assembled chip are shown in **Figure 1.** The X-ray imaging regions of the chip were made of cyclic olefin copolymer (TOPAS® COC, Grade 8007, Tg = 75 °C). The sample flow layer (layer 1) consisted of a CO_2 laser cut, tunable acrylic or silicone pressure sensitive adhesive (25 μm AR92734 or 48 μm AR 92712, Adhesives Research Inc., Glen Rock, PA, USA) used to bond the two microfabricated sides (top and bottom) together. 2-5 μm COC thin films (layer 2) provided low-background sample enclosing layers. These were prepared by spin-coating solutions of 10-20 wt.% COC dissolved in sec-butylbenzene on UV-ozone treated silicon wafers. Films ranging from 500 nm to 10 μm in thickness could be easily produced by varying the COC concentration and spin speed (**Figure S1).** The 200 μm thick COC supports with windows (layer 3) were hot embossed using molds made of elastic polydimethylsiloxane (PDMS, details of the mold fabrication and hot embossing below). And finally, 0.5 or 1 mm polymethyl methacrylate (PMMA) frames (layer 4) with an adhesive layer (3M™ F9460PC) were produced by CO_2 laser cutting.

The use of hard mold materials like steel, silicon or high-temperature epoxy used to emboss COC in previous works[49,59,50] proved difficult due to feature entanglement and warping issues while demolding the COC sheets (with 200 μm deep through-holes) from the rigid molds. PDMS molds proved successful due to their elasticity and low adhesion to COC. These molds were fabricated by casting a replica of a silicon master mold with an array of 300 μm deep X-ray window features using a 5:1 monomer:curing agent mixture of Dow Sylgard™ 184 (fabrication of Si master and additional process details provided in **SI Section 1**). The PDMS replica was demolded and bonded to a silicon wafer using oxygen plasma treatment (50 W, 25 sccm O_2, 0.79 Torr, 1 minute). Hot embossing was performed using a semi-automated EVG 501 wafer bonder. The PDMS mold was brought into contact with a 240 μm COC sheet (Europlex 0F304, Roehm America LLC,

Sanford, ME, USA) attached to a polyvinyl alcohol (9 wt. % PVA, 1500 rpm, 60 s) coated silicon wafer. The assembly was heated to 120 °C and a force of 12 kN was applied for 15 minutes to emboss window in the supports. The embossed sheet was demolded after cooling below the glass transition temperature of COC. Obtaining perfect through holes with hot embossing was difficult due to the flexibility of the PDMS mold. Instead, the ~20-30 µm residual thin film in the windows features was removed by an oxygen plasma reactive-ion etching process (500 W, 25 sccm O_2, 330 mTorr, 30 minutes) to yield the COC window support with through-holes (layer 3). A schematics of the fabrication steps is shown in **Figure 2A,B.**

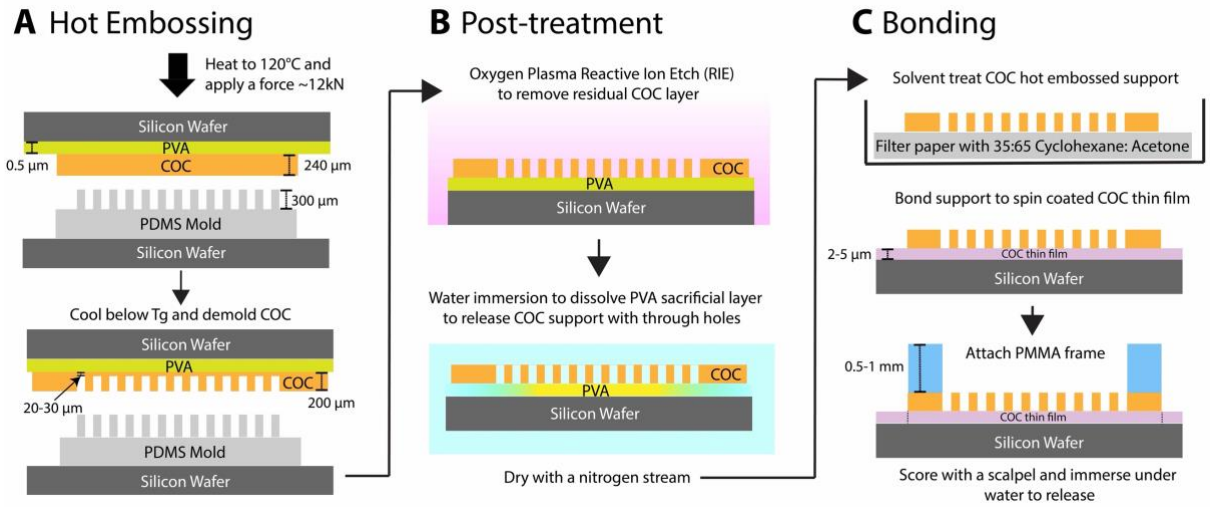

Figure 2: A schematic of the fabrication scheme used to produce the top and bottom sides of the microfluidic chip (as shown in Figure 1). (A) Hot embossing was performed using an elastic PDMS mold to imprint an array of "X-ray window" features in COC sheets (240 µm). (B) The residual thin film (20-30 µm) from the embossing step was removed using oxygen plasma reactive ion etching (RIE) to create COC supports (~200 µm) with through-hole windows. The supports were detached from the silicon wafer by dissolving the PVA sacrificial layer in water. (C) To assemble each side (top and bottom), a COC support was solvent treated to facilitate bonding to COC thin films of desired thicknesses (2-5 µm), followed by attachment of a 0.5-1 mm thick PMMA frame using an adhesive layer to provide rigidity and flatness.

After fabricating the various layers as described above, **Figure 2C** shows a schematic of the processing steps involved in assembling the two symmetric sides of the chip (top and bottom,

Figure 1). First, a COC window support (layer 3) was solvent treated with 35:65 acetone: cyclohexane solution for 1 minute to render the surface tacky[60], dried with a nitrogen stream, and brought into contact with a spin-coated COC thin film (layer 2) on a silicon wafer. This process created a strong room-temperature bond between layers while maintaining the integrity of the thin film (layer 2). The assembly was further reinforced by attaching 0.5 or 1 mm thick PMMA frames (layer 4) on the other side to improve planarity, prevent bowing of the thinner layers, and make the chip easy to handle. At this stage, the assembled layers (layers 2-4) were robust and could be stored until needed. This was advantageous as the flow-layer (layer 1) could be varied in thickness to tailor the chip for a particular protein crystal size/ beamline spot size on demand. Both thin (25-50 μm) or thick (80-150 μm) flow layers could be used depending on sample requirements, e.g., ultra-small protein crystals benefit from thinner flow layers to decrease background from excess crystallization solution, while efficient slurry loading of larger crystals necessitates thicker flow layers. The hydrophobic COC films needed to be rendered hydrophilic prior to final assembly to facilitate fast and complete solution loading into the chip. To do this, assembled top and bottom sides (layers 2-4) were exposed to atmospheric plasma treatment for 3 minutes in a Harrick PDC-32G Basic Plasma Cleaner. Advancing water contact angles using a Ramé-Hart goniometer were $83 \pm 6°$ for the native COC surface, $22 \pm 5°$ after plasma treatment, and recovered to $\sim 60°$ upon storage in ambient conditions for 2-4 weeks (**Figure S2).** To complete the chip fabrication process, the two chip sides were bonded using a laser-cut, double-sided adhesive sample flow layer of the desired thickness. The holes or "window" features (0.5 x 1.75 mm or 1 mm x 1 mm) in the two sides of the chip were aligned by maximizing light transmission through the features using a backlight. The aligned sides were manually pressed together to create an enclosed microfluidic chip. A contact dwell time of 24-72 hours was required to ensure strong adhesion between all the

layers before using the chip. A more detailed protocol on the individual microfabrication steps is provided in the **SI Section S1**.

3.2.2 Water permeability measurements

Water vapor transmission rate as a function of COC film thickness was measured using a slightly modified version wet-cup tests described elsewhere[61]. In brief, free standing COC thin films of different thickness were solvent bonded to a 240 µm COC sheet with a 1 cm diameter hole in the center and affixed to the opening of a 3 mL clear glass vial containing Millipore water using Dow Corning® high vacuum grease. Sample weight loss was monitored over a period of one week from five replicates. Steady-state water vapor transmission rates ($WVTR$) were calculated from the weight loss measurements using $WVTR = \frac{\Delta m}{A \times t}$, where Δm was the weight loss, A is the area of the membrane, and t is the time. The water vapor permeability (WVP) of COC, which is a function of the solubility and diffusivity of water in the material, was calculated by fitting the experimental data to $WVTR = \frac{WVP \times \Delta P}{L}$ where ΔP was the differential pressure of water vapor across the membrane of thickness L. The measurements were carried out in a climate-controlled room with a relative humidity of 20 ± 2% at 23 ± 2 ºC. The relative humidity gradient (ΔRH) was approximately 80% assuming the relative humidity inside the sealed vial enclosure was close to 100%, resulting in $\Delta P = P \times \Delta RH \cong 2.2\ kPa$, using a water vapor saturation pressure of $2.8\ kPa$ at 23 ºC.

3.2.3 Protein expression, purification, and crystallization

SARS-CoV-2 main protease nonstructural protein NSP5 was expressed and purified using modified protocols as previously described[62]. In short, NSP5 was expressed from PGEX-6p-1-NSP5 plasmid (kindly provided by R. Hilgenfeld, University of Lübeck, Germany), from *E. coli* BL21 DE3 Gold cells in 2YT media overnight at 18 ºC. Freshly streaked plates from transformed

glycerol stocks were used for inoculation. The harvested cell pellets were stored at -80 ºC until purification. The pellet was thawed in Buffer A (20 mM Tris pH 7.8, 150 mM NaCl, 5 mM imidazole) and disrupted by sonication at 4 ºC (2 min total) and two passes through a cell disruptor (12-14 kPa). The suspension was clarified by centrifugation (30 kg, 45 min), filtered (0.8 um) and loaded onto a 5 mL HisTrap FF column (Cytiva). The column was washed with 5 CV of Buffer A and the protein eluted in 5mL fractions of Buffer B (20 mM Tris pH 7.8, 150 mM NaCl, 300 mM imidazole). The protein was dialyzed against Buffer C (20 mM Tris pH 7.8, 150 mM NaCl, 0.5 mM TCEP) concurrently with GST tag removal by overnight digestion with 10% w/w HRV3C protease. The protein was loaded into a 5 mL HisTrap FF column and the flow through collected in 12.5 mL fractions. The protein was further purified by size exclusion chromatography (Superdex 200 pg, Cytiva) in Buffer D (20 mM Tris pH 7.8, 150 mM NaCl, 0.5 mM TCEP, 1 mM EDTA). The protein was concentrated to 10 mg/mL and crystallized via vapor diffusion with 100 mM Bis-Tris pH 6.5, 17.5% w/v PEG 3350, 175 mM Li_2SO_4. Seed stock was generated from the resulting large plate clusters using Hampton Research's PTFE seed beads and diluted by a factor of one hundred with crystallization buffer. The vapor diffusion conditions were spiked with 10% 1:100 seed stock and this process was repeated to generate second generation seeds. To crystallize NSP5 on-chip, the same condition used to generate second generation seeds was loaded into a microfluidic chip with 10% second generation seeds (**Table 1**) and crystallized via vapor diffusion as described below.

Chicken egg-white lysozyme (#L6876), thaumatin from *Thaumatococcus daniellii* (#T7638), concanavalin A from *Canavalia ensiformis* (Jack bean) Type VI (#L7647) and catalase from bovine liver (#C40) were purchased from Millipore Sigma (St. Louis, MO, USA) and dissolved in MilliQ water or low ionic strength buffers as listed in **Table 1**. The protein solutions

were gently vortexed for a few seconds until the solution was well-mixed, centrifuged at 10,000 rpm for 5 minutes to remove any insoluble materials, and the supernatant was removed and stored at 4 ºC. All buffers and precipitant solutions were filtered through a 0.22 μm syringe filter prior to use. The crystallization conditions used in this work were adapted from previous literature[63–65] and are also reported in **Table 1**.

Direct crystal slurry loading requires filtration to ensure removal of large crystals which can otherwise clog the inlet channel. While this was tested, this work mainly focusses on demonstration of on-chip crystallization. The microfluidic chips were loaded with a well-mixed 1:1 solution of protein and precipitant solution by pipetting ~8-10 μL into one of the inlet holes in the PMMA frame. Corner vents in the spacer flow layer ensured that the solution filled the wide fluid chamber (~10 mm x 10 mm x 25-50 μm) uniformly while minimizing bubble entrapment. After filling, the inlets and outlets were sealed using Hampton crystal clear sealing tape for micro-batch crystallization or stored unsealed for vapor diffusion crystallization to allow for equilibration with the reservoir chamber. The filled chips were then placed in a Falcon 6-well tissue culture plate either on a microbridge-like pedestal or affixed to a small magnet on the wall of the well plate using magnetic chip holder pin bases (Crystal Positioning Systems, Jamestown, NY, USA). The well was filled with 1.5-2 mL of precipitant solution and the plate was sealed using crystal clear sealing tape to ensure that the chamber remained humidified to prevent sample desiccation during storage over several days to weeks. The optically transparent microfluidic chip and well sealing tape enabled on-chip sample monitoring without disturbing the equilibrated enclosure.

3.2.4 On-chip X-ray diffraction

X-ray diffraction data were collected at RT on the 12-1 beamline at SSRL, equipped with an Eiger X 16M detector (Dectris AG). A magnetic chip holder pin base with a slot and set screw was used

to securely hold the microfluidic chip before magnetically mounting it on the goniometer. Inline high-resolution cameras at ~0° and 90° orientation to the beam were used to position the chip in the beam path, scan through sample regions/windows, and to center the protein crystals along the rotational axis. The beamline allowed for a translation range of ± 2.5 mm along the Y-direction (vertical) and greater than ± 7.5 mm along the X-direction (horizontal). The close proximity of an upstream microcollimator limited the range of rotation about the axis (Z) to ± 35°. The smallest beam size available was 55 μm x 5 μm (X-Y, FWHM), with Y varied between 5 to 50 μm based on crystal size and morphology to maximize the sample-beam interaction cross-section.

Data was collected remotely using the Blu-Ice package[66]. Individual single crystals were manually centered and 30° rotation wedges with 1° oscillation at 0.1s exposure per frame were collected at 10-20 % transmission (full photon flux 4 to 5.6×10^{12} photons per second at 12.5 keV) with a 200 mm detector distance. A drop off in diffraction resolution was observed by the 20-25th frame due to cumulative radiation damage. Data from 15-30 crystals was collected from each chip with the final number of crystals merged for each protein reported in **Table 2**. Diffraction data from multiple crystals was processed in *xia2*[67] (multiplexing mode) running the *CCP4*[68] and *DIALS*[69] packages to perform indexing, merging, and scaling. Structures were solved with *Phaser*[70], part of the *PHENIX* package[71], using PDB entries 1VED, 1RQW, 8CAT, 1SCR, and 6XR3 as templates for phasing via molecular replacement for lysozyme, thaumatin, concanavalin-A, catalase and NSP5 respectively. Iterative refinement was performed with *phenix.refine*[72] alternating with molecular modeling performed with *Coot*[73]. Final data processing and structure refinement statistics are provided in **Table 2**.

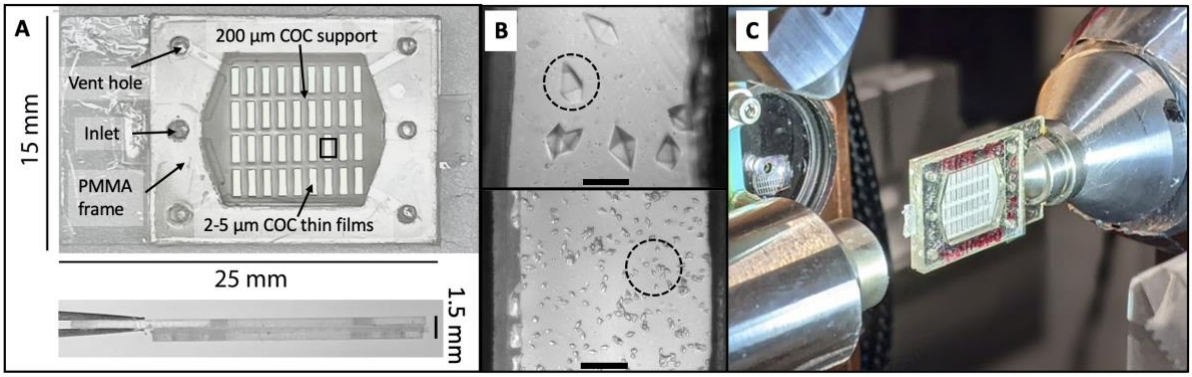

Figure 3: (A) A macroscopic view of the assembled polymer microfluidic chip with a 4 x 9 array of rectangular X-ray windows in the COC supports, to which COC thin films are attached. Features for sample introduction are highlighted in the outermost layer of the chip, the PMMA frame. (B) Optical microscopy images of tetragonal thaumatin crystals grown directly on-chip using micro-batch crystallization as observed through the optically transparent X-ray windows in the chip. The top and bottom figures correspond to crystallization without and with seeding to control crystal size and density. The scale bar is 100 µm. (C) The chip magnetically mounted on the SMB goniometer at SSRL using a chip holder pin base. Experiments were performed at room temperature without the need for any external humidification.

3.3 Results and discussion

3.3.1 Microfluidic chip fabrication and device performance

The goal of this work was to develop robust, user-friendly, low-background microfluidic chips to support room-temperature serial crystallography experiments at synchrotrons or XFEL facilities. A modular fabrication process was designed and used to construct large-area polymer chips that could deliver hundreds to thousands of hydrated protein microcrystals to the X-ray beam. An exemplary chip design (overall dimensions 25 mm x 15 mm) with a 4 x 9 array of rectangular X-ray windows (0.5 mm x 1.75 mm) is shown in **Figure 3A**. The X-ray imaging regions of the chip were made of COC, a thermoplastic material with excellent water barrier properties, optical transmissivity, chemical compatibility with acids, bases and alcohols[74], and low X-ray attenuation[59]. Microfluidic chips based on this material have been reported previously, with

designs using either injection molding to make mm-thick devices, or hot embossing to produce few-hundred μm-thick devices.[48,49,51,53,59] The characterization of small or weakly-diffracting microcrystals in these devices can prove challenging due to significant background from thick enclosing and flow layers, limiting the diffraction resolution attained. Therefore, a key focus of our design was to minimize the X-ray cross section thickness to maximize signal to noise from crystals. This was achieved by using a layered assembly process to produce physically robust and easy-to-handle chips with a total thickness of ~1.5 mm but an effective cross section thickness of only 30-60 μm in the X-ray window regions.

The chip consisted of two sides (**Figure 1**, layers 2-4) mirror symmetric in construction, bonded using a tunable pressure-sensitive adhesive spacer layer that defined the flow layer thickness (layer 1, 25-48 μm in this work). Windows in the 200 μm hot-embossed COC support had ultra-thin 2-5 μm COC films attached that served as the low-background X-ray interaction regions. The outermost 0.5-1 mm thick PMMA frame attached to the COC support imparted rigidity and included inlet, outlet, and vent holes for introduction of crystallization cocktails or crystal slurries into the chip by micro-pipetting. A major advantage of this approach was the straightforward incorporation of tunable-background, wrinkle-free thin films in an enclosed flow-chip design. Solvent bonding eliminated the need to handle fragile films, as is typically required for alternatives like the single/few-layer graphene (<1-3 nm, expensive and laborious to produce)[42,45,52], freestanding commercially-available Mylar (2.5-3.5 μm)[38,40] or Kapton (3-8 μm)[34] films used as enclosing layers in open-format fixed-target chips. The modular construction of the chip allows rapid modifications to the chip design, e.g., the sample area available for rastering, sample volume, and thickness of enclosing and films, depending on sample and experimental requirements. Sample fabrication and assembly of 12 chips took approximately 1 hour, but parallel

processing could further reduce the fabrication time. For applications that do not require ultra-thin supports (<5 μm), the reactive-ion etch step could be omitted after hot-embossing COC sheets to retain ~20-30 μm residual thin films over X-ray windows. This decreases the number of fabrication steps and manufacturing time, but at the cost of proportionally higher background scatter. Hydrophilic oxygen plasma surface treatment provided facile loading of aqueous solutions into the chip as shown in **Figure S3.** The advancing contact angle of atmospheric plasma treated COC films was ~ 22° for freshly treated films and increased to ~ 60° over a period of 4 weeks as shown in **Figure S2**. Thus, fully assembled chips could be stored for at least one month before use without significantly impacting solution loading.

To identify the timescales over which diffraction measurements could be carried out on our chips without external humidification, measurements of water evaporative loss through thin COC films were performed using a modified wet-cup method. **Figure 4** shows the steady-state water vapor transmission rate (WVTR) through COC films as a function of film thickness. The WVTR measured was inversely proportional to the film thickness, as expected for diffusive transport. Film thicknesses ranging from 2.5 to 140 μm were included to serve as a guideline for users to choose barrier properties as required for their application, keeping in mind that scatter background would scale linearly with film thickness. For the 2-5 μm films used in this work, a WVTR of ~ 2 $\frac{mg}{cm^2\ day}$ translated to a low evaporative loss of 0.5-1 wt.% per hour, ensuring that crystals would remain hydrated without external humidity control for several hours during diffraction measurements. To extend sample stability to several weeks, we stored the chips in individually sealed wells with saturated salt slurries of K_2SO_4 (RH set point ~97.3% at 25 °C[75]) or with the precipitant solution, to reduce the relative humidity gradient against which the chips were equilibrating. We found that under these conditions, chips with crystals could be stored over a

period of 2-4 weeks without visible or measurable loss of crystallinity despite the small sample volume in the chip (<10 μL). In comparison, previous microfluidic chips used thick (>50-200 μm) sealing layers of COC, Kapton or Mylar and were stable for weeks in ambient conditions. Thin support films (~2.5-3.5 μm Mylar or 3-8 μm Kapton) have been used previously as enclosing layers with microgrids, but these approaches are seldom designed or characterized for long term stability, requiring sample preparation at the beamline[34,38,40].

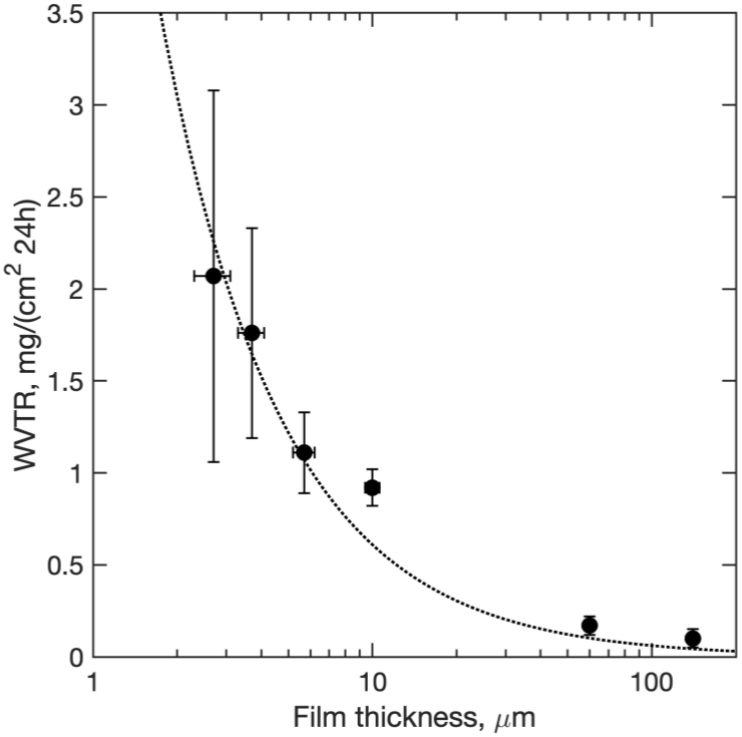

Figure 4: Steady-state water vapor transmission rates (WVTR) through COC films measured using a modified wet-cup method at 23°C, against a ΔRH gradient of approximately 80 percent. COC films in the thickness range of 2-5 μm that were used in this work as sample enclosing layers (layer 2) have a low WVTR of ~2 $\frac{\text{mg}}{\text{cm}^2\ 24\text{hr}}$ or ~0.5-1% sample wt. loss per hour of storage in ambient room temperature conditions without external humidity control. The fitted line corresponds to a water vapor permeability (WVP) of $\sim 10^{-14} - 10^{-13}\ \frac{\text{g m}}{\text{m}^2\ \text{s Pa}}$.

3.3.2 On-chip protein crystallization

To test the utility of the chips for in situ crystal growth and long-term storage, vapor diffusion and micro-batch crystallization trials were conducted for five different proteins by adapting existing conditions from the literature[62–65]. **Table 1** summarizes the crystallization conditions used and compares observations of crystal size, morphology, densities, and time-to-crystallization between on-chip and on-crystallization plate methods (hanging drop vapor diffusion or micro-batch under oil methods were used for comparison as appropriate). For most of the conditions tested, similar crystal sizes and morphologies were obtained on and off chip without the need to modify established crystallization conditions. On average, slightly lower nucleation rates and slower crystallization kinetics were observed on chip leading to larger crystals with sparser densities. Compared to the large droplet solution geometry in plate-based methods, solution in a microfluidic chip is confined to the micro-scale in one or more dimensions. In the near-2D geometry of our chip, a large interfacial contact area between the solution and the polymer surface is expected to affect crystal nucleation. The slower crystallization kinetics are due to the smaller evaporation rate in the chips and that mass transport is primarily driven by molecular diffusion as buoyancy driven convection is suppressed in this geometry.

The 30-200 μm crystal sizes obtained were ideal for proof-of-principle SOX measurements due to the comparable minimum beam size (5 x 55 μm) at the 12-1 microfocus beamline at SSRL. Seeding can be used to control the nucleation rates to produce a high density of smaller 10-20 μm microcrystals. **Figure 3B** shows fully hydrated, randomly oriented tetragonal thaumatin crystals grown on chip using micro-batch crystallization (without and with seeding, top and bottom respectively) and stored for three days. **Figure S4** shows exemplary images of the other protein crystals measured in this work. It is worth noting that the thin spacer film (25-48 μm) not only

reduced the sample volume requirements (4-8 μL) but also restricted crystal growth in the Z-direction to span the "set" spacer thickness. This minimized scatter contribution from the crystallization solution surrounding the microcrystals. Preferential alignment of 200-300 μm long plate-like crystals of concanavalin-A and NSP5 was observed microscopically. The concanavalin-A crystals appeared to grow to span the entire spacer thickness ~50 μm whereas individual NSP5 plates in the crystal clusters were ~10-15 μm thick. Lysozyme and catalase crystals, which were cuboid in appearance, did not have any visible preferential alignment.

Table 1: A summary of crystallization conditions used in this work and a comparison of crystal size, morphology, density, and time to first crystals, obtained from on-chip crystallization and comparable crystallization in 24-well crystallization plates. For on-chip crystallization, ~8 μL of solution was loaded into the chip and the chip was stored either sealed (micro-batch) or unsealed (vapor diffusion) in an enclosed environment with the precipitant solution in the reservoir. Similar droplet volumes were used for crystallization in a 24-well plate format using micro-batch under oil (paraffin) or hanging drop vapor diffusion methods for comparison, as appropriate. Crystal density (n= # of crystals/mm^2) was measured using optical microscopy and qualitatively described as low for $n \leq 10$, medium for $10 < n < 100$, and high for $n \geq 100$.

Protein	**Protein solution**	**Precipitant solution**	**Incubation Temperature**	**Crystallization method**	**Crystal size, morphology, density, crystallization time**	
					On-chip	**24-well Crystallization plate**
Lysozyme	30 mg/mL in 20 mM Sodium Acetate buffer, pH 4.6	1M Sodium Chloride, 0.1M Sodium Acetate buffer, pH 4.6	4°C	Micro-batch	25-35 μm, cuboid, high, ~2-3 hours.	25-35 μm, cuboid, high, ~2-3 hours.

	50 mg/mL in DI water	2M Sodium Chloride, 0.1M Sodium Acetate buffer, pH 4.6	21°C	Micro-batch	60-100 μm, cuboid, low, 12-24 hours.	30-70 μm, cuboid, medium, 2-4 hours.
Thaumatin	25 mg/ml in DI water	1M L-Sodium Potassium Tartrate, 0.1M ADA buffer, pH 6.5	4°C	Micro-batch	~25 μm, tetragonal bipyramidal, low, ~12 hours. Crystals grow to 70-100 μm in size over 2-3 days.	~20 μm, tetragonal bipyramidal, high, ~12 hours.
			21°C	Micro-batch	50-100 μm, tetragonal bipyramidal, low, 3-4 days.	Did not crystallize
			21°C	Vapor diffusion	50-100 μm, tetragonal bipyramidal, low, ~24 hours.	50-150 μm, tetragonal bipyramidal, low, ~24 hours.
			21°C	Micro-batch (with seeding using 1° seed stock 1:5:5 seed: protein: precipitant)	15-20 μm, tetragonal bipyramidal, high, ~24 hours.	15-20 μm, tetragonal bipyramidal, high, ~24 hours
Concanavalin -A (Type VI)	70 mg/mL in 20 mM Tris buffer, pH 8.0	2.8M Ammonium Sulfate in 0.1M Tris buffer, pH 8.5	21°C	Micro-batch	150-300 μm, round base rhombic tetrahedron, low, ~12 hours.	30-60 μm, cubic, high, 0-2 hours initially; equilibrates to 150-300 μm, round base rhombic tetrahedron, low, over the next 3-7 days.

Bovine Liver Catalase	40 mg/mL in 50 mM Sodium Phosphate buffer, pH 6.8	22.5% PEG 4000 in 0.1M Tris buffer, pH 8.5	21°C	Micro-batch	70-120 μm, prism shaped, low, <12 hours	70-120 μm, prism shaped, low, 2-4 hours
			21°C	Vapor diffusion	30-100 μm, prism shaped, medium, 0-4 hours	30-100 μm, prism shaped, medium, 0-2 hours
NSP5	5mg/ml in 20 mM Tris pH 7.8, 150 mM NaCl, 0.5 mM TCEP, 1 mM EDTA	100 mM Bis-Tris pH 6.5, 17.5% w/v PEG 3350, 175 mM; Li_2SO_4; 10% 1:100 2' seeds	21°C	Vapor diffusion, with seeding	300 um, large thin plate clusters, low, ~12 hours	150-200 μm large single plates or plate clusters, low, ~12 hours

3.3.3 X-ray scatter background measurements

To quantify and compare the X-ray scatter background contributions from different materials in the beam interaction cross section, background measurements of ambient air scattering (5 mm path length), chips with different COC films thicknesses, and buffer-filled chips (0.1 M Na Acetate buffer, 1M NaCl) with two different spacer thicknesses were carried out. Radial averages of the scattered intensity for air and buffer filled chips (**Figure 5**) are dominated at low angles by air-scatter background. Contributions to background scattering from the enclosing amorphous COC films represent an increase of approximately 20 percent over ambient air scattering at the peak of the COC-associated scattering at approximately 1.1 $Å^{-1}$, corresponding to 5.8 Å in real space (seen as a broad "halo"). This is in agreement with previous observations of increased scattering ~ 5-6 Å for different COC grades[52,59] and indicates there is some degree of systematic packing between adjacent polymer backbone strands[76]. COC also contributes a broad, featureless scattering signal

at low resolution (>6 Å). At higher angles, the enclosed buffer layer was the most significant background contribution with buffer filled chips exhibiting a "water ring" at 1.8 $Å^{-1}$ corresponding to 3.4 Å in real space. This contribution can be decreased by using a thinner spacer layer as demonstrated by the yellow curve in **Figure 5,** corresponding to a chip with a 25 µm spacer layer.

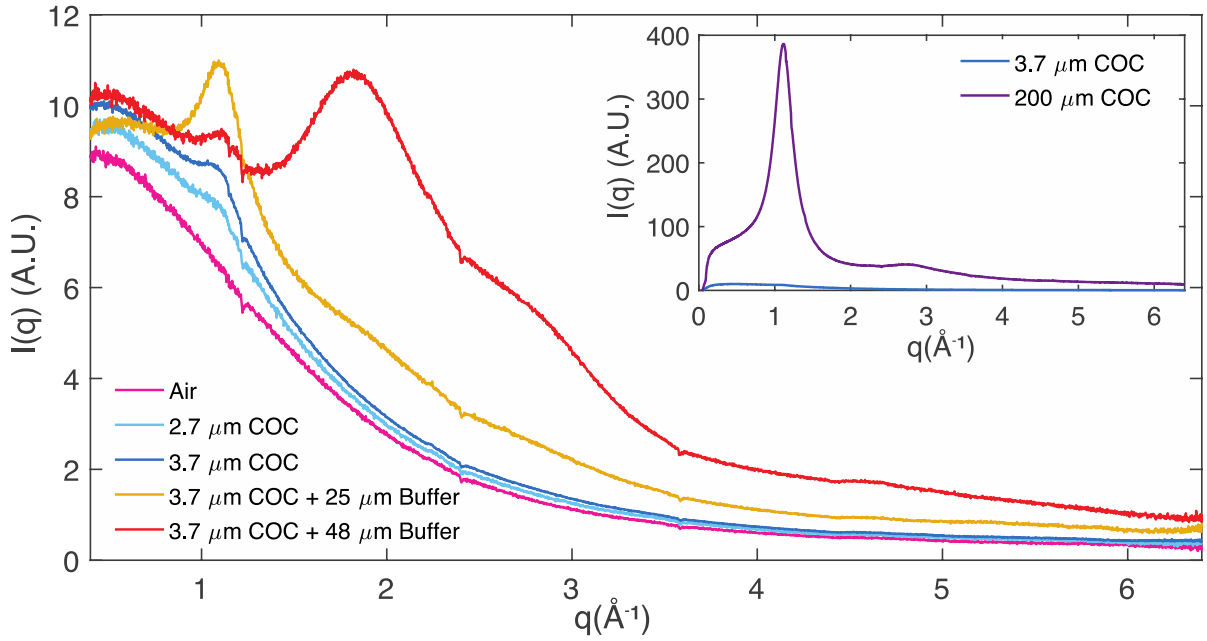

Figure 5: Radial averages of scattering associated with crystal-free chips (or instrument-associated air scattering) to quantify background scattering contributions. Air (cyan, blue) and buffer-filled (red, yellow) chips with nominal 2.7 µm (cyan) or 3.7 µm (yellow, blue, red) COC enclosing films and 50 µm (red) or 25 µm (yellow) spacer layers are shown. Note: The data represented by the yellow curve, collected during a separate beamtime using a different batch of COC material from Polysciences Inc., shows a slightly different scatter profile at low q. Inset: Comparison of scattering intensity from the 200 µm COC support frame material and a 3.7 µm enclosing film.

Because of the inherent flexibility of the enclosing thin COC films, some variability (10-20 percent) in the buffer or flow layer thickness is expected. This explains why the scattering signal (around 1.8 $Å^{-1}$) for the 25- and 48-µm spacer samples does not scale linearly. Minor changes in peak intensities at ~ 0.3 and ~ 1.1 $Å^{-1}$ were also observed between the 25 and 48 µm spacer

samples, that cannot be explained sufficiently by COC film thickness variation between different batches (< 0.2 μm). Since the two samples were characterized during different beamtimes using different batches of COC from Polysciences, Inc., we suspect minor batch to batch compositional variation in the supplied COC material and subsequent spin-coating solution preparation and processing steps (filtration, postbake) could influence the degree of short-range chain packing, resulting in slightly different amorphous scatter signal at low q. Regardless, both the enclosing film thickness and the flow spacer thickness are parameters that can be changed to control background scatter to match sample requirements. While a direct background comparison with other microfluidic chips from literature is made challenging due to differences in material attenuation properties, film and flow layer thicknesses, and beam characteristics, the inset in **Figure 5** shows the drastic reduction in background that results from using thin films over X-ray windows (~3.7 μm per side) vs. shooting through thick supports (~200 μm per side) that are on the order of film thicknesses sometimes used as capping layers in microfluidic chips.

3.3.4 In situ X-ray diffraction at room temperature

Figure 3C shows the COC microfluidic chip mounted on a slotted magnetic pin base and attached to the goniometer for room-temperature data collection at the 12-1 beamline at SSRL. The device's large measurable area and facile mounting allowed rapid collection of data in a semi-serial mode where 30° rotation wedges were collected on a series of manually centered crystals, eliminating the need for mounting of individual crystals. Individual wedges were collected in 15- 20 seconds. The average data collection time for each chip was between 30 min and one hour, where the limiting step was manual centering of the crystals. Minimal settling or crystal movement was observed for most in situ grown crystals where the crystal size was well matched to the spacer

layer thickness due to contact with the COC films. Some movement was observed when the crystal size was well below the spacer thickness (~50 μm spacer vs. 10-20 μm lysozyme crystals).

Data from 5 to 16 individual crystals were merged to constitute complete data sets for the measured proteins. Data collection and refinement statistics for each protein are shown in **Table 2**. The lysozyme, thaumatin, and concanavalin-A crystals generated high resolution datasets, diffracting to 1.5 Å, 1.45 Å, and 1.30 Å respectively, with high multiplicity and excellent merging statistics including overall $CC_{1/2}$ of 0.999, 0.999, and 0.993 respectively. The catalase dataset diffracted to a slightly lower resolution of 2.27 Å ($CC_{1/2}$ 0.997) but is comparable in quality to other room temperature structures reported for the protein[77]. Random crystal orientation for lysozyme, thaumatin and catalase was confirmed by a high degree of completeness, both in the total dataset and in the highest resolution shell. Concanavalin-A had only slightly less favorable completeness statistics because of its lower symmetry space group and apparent preferentially orientated crystal growth to span the spacer thickness **(Figure S4F)**.

In cases where in situ growth limited crystal size to the full spacer thickness, background scattering around the water ring (1.8 $Å^{-1}$) was lower due to displacement of excess crystallization solution from the X-ray cross section (**Figure S5**). Moreover, when contact between crystals and the enclosing COC films was high, mother liquor background could also be reduced by physically removing excess buffer from the chip, leaving film-supported crystals surrounded by a minimal amount of mother liquor as observed in the case of catalase (**Figure S6**). The differences in the unit cell dimensions between the fully hydrated and excess solvent removed or partially "dehydrated" crystals were within the measurement error with ~0.1 Å larger *a*- and *b*- unit cell dimensions for the fully hydrated crystals. The merging statistics for both these datasets is reported in **Table S1**.

Plate-like or plate-cluster morphologies for the larger, thinner NSP5 crystals, however, proved more challenging as the chip geometry limited possible crystal orientations. **(Figure S4C).** This made collection of an adequately redundant data set with sufficient completeness in all resolution shells difficult. Some of the crystals in the NSP5 dataset diffracted up to 2.3 Å which is comparable to other room temperature data sets for the protein that use similar crystallization conditions, PDB entries 6WQF (single crystal, 2.3 Å) and 7JVZ (SFX, 2.5 Å). But ultimately, a lower resolution cut-off of 2.7 Å was used for the final structure refinement due to constraints imposed by the crystal morphology and the low symmetry space group (C2), although only one chip with this sample was measured. We expect that additional samples and tuning of on chip crystal density and crystal size would improve these results. Overall, each of the solved structures were in excellent agreement with the PDB references used for molecular replacement except for a previously unreported carboxymethylation on the Cys376 residue observed in our catalase structure. The RMSD values ranged from 0.121-0.416 Å, which includes minor movements of sidechains and loops and are shown in **Table S2**. Representative $2mF_o$-DF_c electron density maps of the concanavalin-A and catalase actives sites are shown in **Figure 6**.

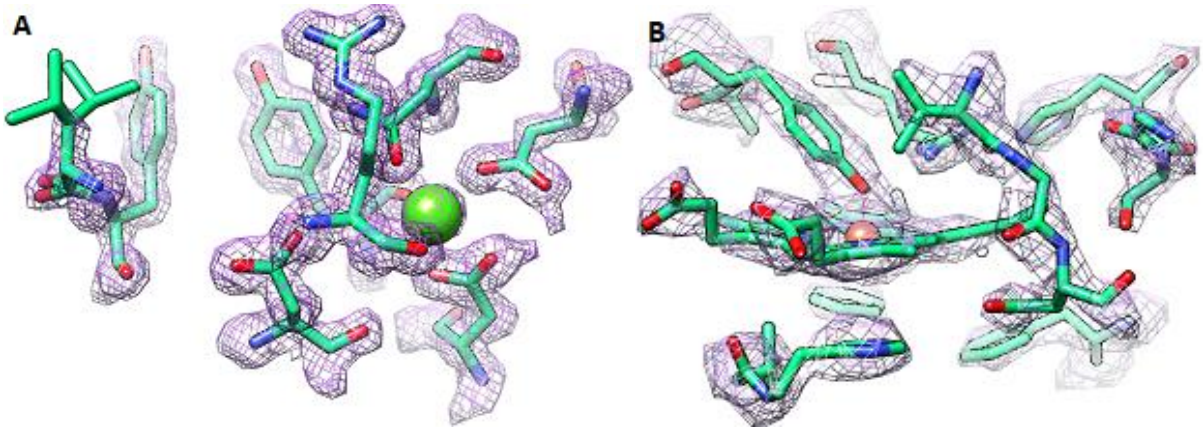

Figure 6: Active sites of two structures determined from on-chip crystallization and synchrotron data collection. The $2mF_o$-DF_c density maps at 1.5σ are show in purple mesh. (A) The saccharide binding site and calcium coordination site of concanavalin A. (B) The heme active site of catalase bound to a proximal tyrosine residue.

To study the effects of long-term storage on chip, data was also collected on lysozyme crystallized under similar conditions but stored in a humidified environment at 21 °C for 17 days ("aged"). These crystals showed minimal signs of dehydration based on unit cell shrinkage, and diffracted to similar resolutions, as much as 1.5 Å for the aged samples compared to 1.87 Å for freshly prepared crystals (stored for 3 days on chip). This difference in resolution can be attributed to slight differences in crystal dimensions and normal variation in crystal quality, especially given that each of these datasets was obtained from multiple crystals which diffracted to differing resolutions. Thus, long term storage effects such as evaporative dehydration did not degrade crystal quality. The RMSD between the two structures was 0.094 Å, demonstrating that the two structures were identical. A detailed comparison of crystallographic statistics for the aged and fresh lysozyme sample is included in **Table 2.**

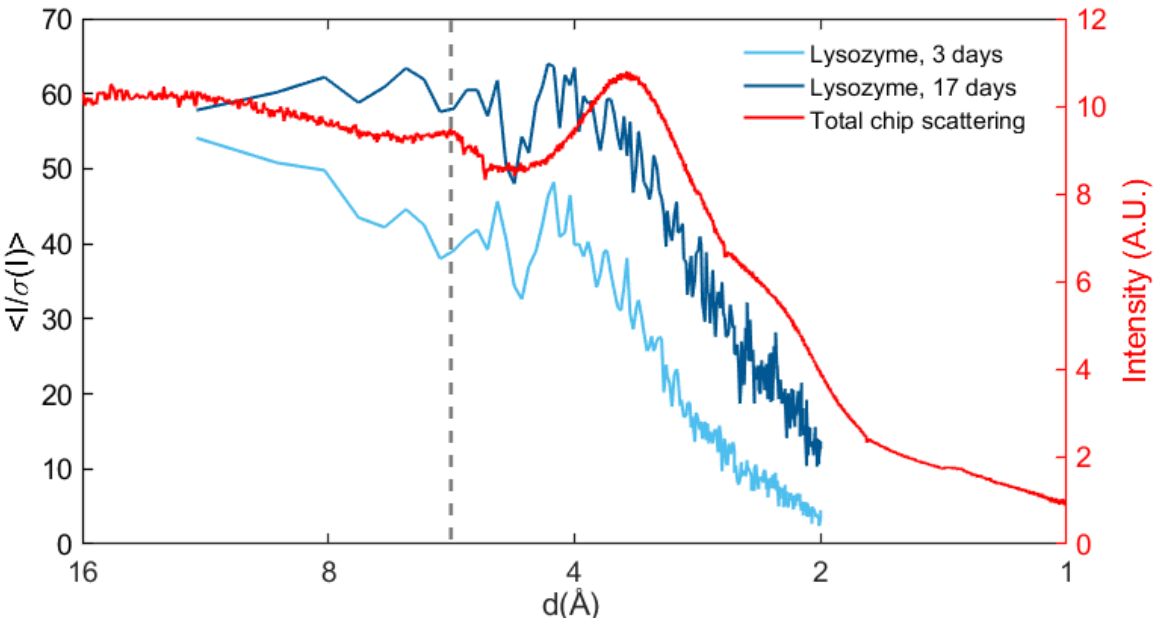

Figure 7: A comparison between the $I/\sigma(I)$ for the two lysozyme structures solved in this work and the total scattering background from the chip. The fresh sample shown in light blue (~30 µm crystals) diffracted to 1.87 Å and the aged sample shown in dark blue (~70 µm crystals) diffracted to 1.5 Å confirming that long term storage of crystals on the chip does not affect crystal integrity. A small dip in signal to noise is observed around scattering peak for COC around 5.8 Å (dashed line). The larger dip around 5 Å corresponds to the location of a gap in the detector panel (masked out during analysis) and is confirmed by a decrease in the number of reflections in this resolution bin.

To assess the effect of both the polymer thin film and the mother liquor surrounding the crystals on the structures, we made a comparison between the $I/\sigma(I)$ vs resolution and the measured chip background (purely buffer-filled) vs resolution for both fresh and aged lysozyme, as shown in **Figure 7.** Both samples appear to have no features in $I/\sigma(I)$ that correlate with background scattering and no deleterious effects of the COC scatter peak at 5.8 Å are apparent. While there is a small drop in $I/\sigma(I)$ around the peak of COC scattering, in both cases it is within the level of noise in the data.

Table 2: Crystallographic statistics obtained from Lysozyme, Thaumatin and Concanavalin-A, Catalase and NSP5 crystals grown in the microfluidic chip. Values in parentheses correspond to the highest resolution shell.

Protein	**Lysozyme (fresh)**	**Lysozyme (aged)**	**Thaumatin**	**Concanavalin-A**	**Catalase**	**NSP5**
Number of crystals used	7	6	16	12	7	11
Average crystal size (Largest dimension)	~30-35 µm	~70 µm	~ 100 µm	~ 200 µm	~ 90-100 µm	~ 200 µm
Resolution range ($\dot{A}$)	56.05 - 1.87 (1.94 - 1.87)	35.25 - 1.5 (1.55 - 1.5)	58.61 - 1.45 (1.48 - 1.45)	51.18 - 1.30 (1.35 - 1.30)	52.8 - 2.274 (2.355 - 2.274)	31.64 - 2.7 (2.797 - 2.7)
Unit cell dimensions	$a = b$ = 79.26 $\dot{A}$, c = 37.94 $\dot{A}$, $\alpha = \beta = \gamma$ = 90°	$a = b$ = 78.82 $\dot{A}$, c = 38.207 $\dot{A}$, $\alpha = \beta = \gamma$ = 90°	$a = b$ = 58.60 $\dot{A}$, c = 151.44 $\dot{A}$, $\alpha = \beta = \gamma$ = 90°	a = 63.20 $\dot{A}$, b = 87.22 $\dot{A}$, c = 89.12 $\dot{A}$, $\alpha = \beta = \gamma$ = 90°	$a = b$ = 141.77 $\dot{A}$, c =103.47 $\dot{A}$, $\alpha = \beta$ = 90°, γ = 120°	a = 114.29 $\dot{A}$, b = 54.81 $\dot{A}$, c =45.33 $\dot{A}$, $\alpha = \gamma$ = 90°, β = 101.45°
Space group	$P4_32_12$	$P4_32_12$	$P4_12_12$	I222	$P3_221$	C121
Data processing statistics						
Total reflections	120310 (12080)	331623 (33168)	1392515 (65410)	786259 (24955)	1040538 (97971)	49766 (5027)
Unique reflections	10449 (1003)	19849 (1949)	47884 (2332)	60428 (5732)	55166 (5256)	7530 (747)
Multiplicity	11.5 (12.0)	16.7 (17.0)	29.1 (28.0)	13.0 (4.4)	18.9 (18.6)	6.6 (6.7)
Completeness (%)	99.82 (98.91)	99.97 (99.95)	100.0 (100.0)	98.8 (89.5)	99.56 (95.89)	96.30 (93.18)
Mean $I/\sigma(I)$	11.47 (2.02)	16.80 (1.59)	15.4 (0.9)	17.6 (0.6)	10.64 (1.05)	8.24 (1.78)
R_{merge}	0.159 (1.63)	0.09752 (1.953)	0.146 (3.606)	0.072 (2.107)	0.218 (2.587)	0.248 (2.01)

R_{meas}	0.167 (1.703)	0.1007 (2.013)	0.149 (3.671)	0.075 (2.384)	0.224 (2.658)	0.2691 (2.183)
R_{pim}	0.048 (0.481)	0.02467 (0.4847)	0.027 (0.677)	0.019 (1.055)	0.051 (0.606)	0.097 (0.795)
$CC_{1/2}$	0.994 (0.602)	0.999 (0.773)	0.999 (0.647)	0.993 (0.159)	0.997 (0.576)	0.968 (0.267)
Wilson B-factor	28.48	22.45	19.9	17.8	48.65	55.59
Refinement statistics						
R_{work} (%)	15.61	15.02	15.2	14.6	16.2	18.0
R_{free} (%)	17.9	17.13	16.0	16.5	20.1	21.8
RMS (bonds, Å)	0.005	0.008	0.022	0.004	0.003	0.003
RMS (angles, °)	0.59	0.84	1.59	0.83	0.58	0.53
Ramachandran						
favored (%)	99.21	99.21	98.0	97.8	95.85	96.04
allowed (%)	0.79	0.79	2.0	2.2	3.94	3.96
outliers (%)	0	0	0	0	0.20	0
Average B-factor						
macromolecule	33.30	28.13	21.9	22.7	56.46	59.64
ligands	-	-	-	14.6	55.17	-
solvent	36.39	36.13	38.6	34.6	46.48	49.38

3.4 Conclusion

In summary, this work demonstrates the development of robust, easy-to-use polymer microfluidic chips that can be used for routine and reliable room temperature diffraction measurements on fully hydrated protein microcrystals. Our large area, optically transparent chips are compatible with *in*

situ crystallization, sample monitoring, crystal storage and transport, and diffraction measurements directly on the chip, eliminating the need to handle small or fragile crystals. The chips are stable over several weeks in a humidified environment, and for several hours in ambient conditions removing the stress of on-the-fly sample preparation. The modular device construction allows design flexibility to tune sample or flow layer thickness, enclosing film thickness, chip volume, or rastering area to match sample and experimental requirements. In this work, the chips were designed to be directly compatible with the standard goniometer setup at SSRL. High resolution structures (1.3-2.7 Å) for five different proteins (including one "non-model" protein, NSP5) were collected on chip using SOX. Looking forward, we envision these low-cost chips could be made available to users, to allow crystallization and sample screening well ahead of beam-time, followed by streamlined plug-and-play experiments with minimal sample handling or mounting requirements. The platform can be expanded to add functionalities to study not just static structures but dynamics by leveraging microfluidic capabilities to allow ligand introduction, electric field application, temperature-jumps, or pump-probe time-resolved experiments.

3.4.1 Outlook: XFEL measurements

We are currently expanding this work and are applying the design and fabrication principles to produce and demonstrate chips that are tailored for XFEL SFX applications. The diffraction before destruction principle of operation at XFEL sources demands fresh sample at *every* beam shot. Based on the crystal symmetry and the data analysis techniques used[78,79], hundreds to tens of thousands of crystals must be delivered to the beam in random orientations. Since XFEL beamtime is limited and precious, our goal is to develop a "shelf-stable", plug-and-play microfluidic chip for XFEL sample introduction that maintains crystal hydration for up to 24 hours without the need for external humidity control, while still contributing minimally to background. This would address

some of the limitations of existing approaches like the need for on-the-fly sample preparation (open-format chips) and high background (microfluidic chips) to enable routine, high-resolution SFX with minimal downtime. Validation of the first XFEL chip prototypes in preliminary experiments is promising. The current design allows collection of ~10^4 useful, low background shots per chip when continuously rastering through the thick and thin regions of the chip support with minimal alignment requirements due to the diffuse scattering of the amorphous target material. Our ongoing efforts focus on (1) maximizing the X-ray window regions on the chip to increase the fraction of area useful for sample characterization (beyond current limit of 50 % due to thick supports), (2) controlling crystal nucleation and crystal densities on the chip leveraging surface chemistry modifications, and (3) demonstrating the use of this platform for more non-model proteins of interest.

3.5 Acknowledgements and Funding Information

This work was performed, in part, under the auspices of the U.S. DOE by LLNL under Contract DE-AC52-07NA27344. This work was also supported by National Science Foundation (NSF) BioXFEL STC Grant 1231306, NIH grants R01GM117342 (NIGMS) and U19 AI144184 (NIAID). Use of the Stanford Synchrotron Radiation Lightsource, SLAC National Accelerator Laboratory, is supported by the U.S. Department of Energy, Office of Science, Office of Basic Energy Sciences under Contract No. DE-AC02-76SF00515. The SSRL Structural Molecular Biology Program is supported by the DOE Office of Biological and Environmental Research, and by the National Institutes of Health, National Institute of General Medical Sciences (P30GM133894). The contents of this publication are solely the responsibility of the authors and do not necessarily represent the official views of NIGMS or NIH. Use of the LCLS, SLAC

National Accelerator Lab, is supported by the U.S. DOE, Office of Science, under contract no. DE-AC02-76SF00515.

The PGEX-6p-1-NSP5 plasmid was kindly provided by R. Hilgenfeld (University of Lübeck, Germany).

3.6 References

1. Hope, H. Cryocrystallography of biological macromolecules: a generally applicable method. *Acta Crystallogr. B* **44**, 22–26 (1988).
2. Moreno, A. Advanced Methods of Protein Crystallization. in *Protein Crystallography* (eds. Wlodawer, A., Dauter, Z. & Jaskolski, M.) vol. 1607 51–76 (Springer New York, 2017).
3. Skarina, T., Xu, X., Evdokimova, E. & Savchenko, A. High-Throughput Crystallization Screening. in *Structural Genomics and Drug Discovery* (ed. Anderson, W. F.) vol. 1140 159–168 (Springer New York, 2014).
4. Cusack, S. *et al.* Small is beautiful: protein micro-crystallography. *Nat. Struct. Biol.* **5**, 634–637 (1998).
5. Smith, J. L., Fischetti, R. F. & Yamamoto, M. Micro-crystallography comes of age. *Curr. Opin. Struct. Biol.* **22**, 602–612 (2012).
6. Chapman, H. N. *et al.* Femtosecond X-ray protein nanocrystallography. *Nature* **470**, 73–77 (2011).
7. Schlichting, I. & Miao, J. Emerging opportunities in structural biology with X-ray free-electron lasers. *Curr. Opin. Struct. Biol.* **22**, 613–626 (2012).
8. Hirata, K. *et al.* Determination of damage-free crystal structure of an X-ray–sensitive protein using an XFEL. *Nat. Methods* **11**, 734–736 (2014).
9. Fischer, M. Macromolecular room temperature crystallography. *Q. Rev. Biophys.* **54**, e1 (2021).
10. Schmidt, M. Mix and Inject: Reaction Initiation by Diffusion for Time-Resolved Macromolecular Crystallography. *Adv. Condens. Matter Phys.* **2013**, 1–10 (2013).
11. Tenboer, J. *et al.* Time-resolved serial crystallography captures high-resolution intermediates of photoactive yellow protein. *Science* **346**, 1242–1246 (2014).
12. Pawate, A. S. *et al.* Towards time-resolved serial crystallography in a microfluidic device. *Acta Crystallogr. Sect. F Struct. Biol. Commun.* **71**, 823–830 (2015).
13. Orville, A. M. Recent results in time resolved serial femtosecond crystallography at XFELs. *Curr. Opin. Struct. Biol.* **65**, 193–208 (2020).
14. Pearson, A. R. & Mehrabi, P. Serial synchrotron crystallography for time-resolved structural biology. *Curr. Opin. Struct. Biol.* **65**, 168–174 (2020).
15. Boutet, S. *et al.* High-Resolution Protein Structure Determination by Serial Femtosecond Crystallography. *Science* **337**, 362–364 (2012).
16. Liu, W., Ishchenko, A. & Cherezov, V. Preparation of microcrystals in lipidic cubic phase for serial femtosecond crystallography. *Nat. Protoc.* **9**, 2123–2134 (2014).
17. Wierman, J. L. *et al.* Fixed-target serial oscillation crystallography at room temperature. *IUCrJ* **6**, 305–316 (2019).

18. Lyubimov, A. Y. *et al.* Capture and X-ray diffraction studies of protein microcrystals in a microfluidic trap array. *Acta Crystallogr. D Biol. Crystallogr.* **71**, 928–940 (2015).
19. Martiel, I., Müller-Werkmeister, H. M. & Cohen, A. E. Strategies for sample delivery for femtosecond crystallography. *Acta Crystallogr. Sect. Struct. Biol.* **75**, 160–177 (2019).
20. Cheng, R. Towards an Optimal Sample Delivery Method for Serial Crystallography at XFEL. *Crystals* **10**, 215 (2020).
21. DePonte, D. P. *et al.* Gas dynamic virtual nozzle for generation of microscopic droplet streams. *J. Phys. Appl. Phys.* **41**, 195505 (2008).
22. Weierstall, U. *et al.* Lipidic cubic phase injector facilitates membrane protein serial femtosecond crystallography. *Nat. Commun.* **5**, 3309 (2014).
23. Sierra, R. G. *et al.* Concentric-flow electrokinetic injector enables serial crystallography of ribosome and photosystem II. *Nat. Methods* **13**, 59–62 (2016).
24. Oberthuer, D. *et al.* Double-flow focused liquid injector for efficient serial femtosecond crystallography. *Sci. Rep.* **7**, 44628 (2017).
25. Fuller, F. D. *et al.* Drop-on-demand sample delivery for studying biocatalysts in action at X-ray free-electron lasers. *Nat. Methods* **14**, 443–449 (2017).
26. Beyerlein, K. R. *et al.* Mix-and-diffuse serial synchrotron crystallography. *IUCrJ* **4**, 769–777 (2017).
27. Zarrine-Afsar, A. *et al.* Crystallography on a chip. *Acta Crystallogr. D Biol. Crystallogr.* **68**, 321–323 (2012).
28. Frank, M. *et al.* Femtosecond X-ray diffraction from two-dimensional protein crystals. *IUCrJ* **1**, 95–100 (2014).
29. Hunter, M. S. *et al.* Fixed-target protein serial microcrystallography with an x-ray free electron laser. *Sci. Rep.* **4**, 6026 (2015).
30. Feld, G. K. *et al.* Low- *Z* polymer sample supports for fixed-target serial femtosecond X-ray crystallography. *J. Appl. Crystallogr.* **48**, 1072–1079 (2015).
31. Cohen, A. E. *et al.* Goniometer-based femtosecond crystallography with X-ray free electron lasers. *Proc. Natl. Acad. Sci.* **111**, 17122–17127 (2014).
32. Halsted, T. P. *et al.* An unprecedented dioxygen species revealed by serial femtosecond rotation crystallography in copper nitrite reductase. *IUCrJ* **5**, 22–31 (2018).
33. Baxter, E. L. *et al.* High-density grids for efficient data collection from multiple crystals. *Acta Crystallogr. Sect. Struct. Biol.* **72**, 2–11 (2016).
34. Murray, T. D. *et al.* A high-transparency, micro-patternable chip for X-ray diffraction analysis of microcrystals under native growth conditions. *Acta Crystallogr. D Biol. Crystallogr.* **71**, 1987–1997 (2015).
35. Roedig, P. *et al.* A micro-patterned silicon chip as sample holder for macromolecular crystallography experiments with minimal background scattering. *Sci. Rep.* **5**, 10451 (2015).
36. Coquelle, N. *et al.* Raster-scanning serial protein crystallography using micro- and nano-focused synchrotron beams. *Acta Crystallogr. D Biol. Crystallogr.* **71**, 1184–1196 (2015).
37. Axford, D., Aller, P., Sanchez-Weatherby, J. & Sandy, J. Applications of thin-film sandwich crystallization platforms. *Acta Crystallogr. Sect. F Struct. Biol. Commun.* **72**, 313–319 (2016).
38. Oghbaey, S. *et al.* Fixed target combined with spectral mapping: approaching 100% hit rates for serial crystallography. *Acta Crystallogr. Sect. Struct. Biol.* **72**, 944–955 (2016).
39. Roedig, P. *et al.* High-speed fixed-target serial virus crystallography. *Nat. Methods* **14**, 805–810 (2017).

40. Doak, R. B. *et al.* Crystallography on a chip – without the chip: sheet-on-sheet sandwich. *Acta Crystallogr. Sect. Struct. Biol.* **74**, 1000–1007 (2018).
41. Ren, Z. *et al.* Crystal-on-crystal chips for *in situ* serial diffraction at room temperature. *Lab. Chip* **18**, 2246–2256 (2018).
42. Seuring, C. *et al.* Femtosecond X-ray coherent diffraction of aligned amyloid fibrils on low background graphene. *Nat. Commun.* **9**, 1836 (2018).
43. Lee, D. *et al.* Nylon mesh-based sample holder for fixed-target serial femtosecond crystallography. *Sci. Rep.* **9**, 6971 (2019).
44. Karpik, A., Martiel, I., Kristiansen, P. M. & Padeste, C. Fabrication of ultrathin suspended polymer membranes as supports for serial protein crystallography. *Micro Nano Eng.* **7**, 100053 (2020).
45. Shelby, M. L. *et al.* A fixed-target platform for serial femtosecond crystallography in a hydrated environment. *IUCrJ* **7**, 30–41 (2020).
46. Shelby, M. *et al.* Crystallization of ApoA1 and ApoE4 Nanolipoprotein Particles and Initial XFEL-Based Structural Studies. *Crystals* **10**, 886 (2020).
47. Hansen, C. L., Classen, S., Berger, J. M. & Quake, S. R. A Microfluidic Device for Kinetic Optimization of Protein Crystallization and *In Situ* Structure Determination. *J. Am. Chem. Soc.* **128**, 3142–3143 (2006).
48. Ng, J. D., Clark, P. J., Stevens, R. C. & Kuhn, P. *In situ* X-ray analysis of protein crystals in low-birefringent and X-ray transmissive plastic microchannels. *Acta Crystallogr. D Biol. Crystallogr.* **64**, 189–197 (2008).
49. Dhouib, K. *et al.* Microfluidic chips for the crystallization of biomacromolecules by counter-diffusion and on-chip crystal X-ray analysis. *Lab. Chip* **9**, 1412 (2009).
50. Jena, R. K., Yue, C. Y., Lam, Y. C., Tang, P. S. & Gupta, A. Comparison of different molds (epoxy, polymer and silicon) for microfabrication by hot embossing technique. *Sens. Actuators B Chem.* **163**, 233–241 (2012).
51. Pinker, F. *et al.* ChipX: A Novel Microfluidic Chip for Counter-Diffusion Crystallization of Biomolecules and in Situ Crystal Analysis at Room Temperature. *Cryst. Growth Des.* **13**, 3333–3340 (2013).
52. Sui, S. *et al.* Graphene-based microfluidics for serial crystallography. *Lab. Chip* **16**, 3082–3096 (2016).
53. de Wijn, R. *et al.* A simple and versatile microfluidic device for efficient biomacromolecule crystallization and structural analysis by serial crystallography. *IUCrJ* **6**, 454–464 (2019).
54. Popov, A. M., Dorovatovskii, P. V., Mamichev, D. A., Marchenkova, M. A. & Nikolaeva, A. Yu. Development of a Microfluidic Chip for Protein Crystallization by the Microbatch Method. *Crystallogr. Rep.* **64**, 282–286 (2019).
55. Zhao, F.-Z. *et al.* A novel sample delivery system based on circular motion for *in situ* serial synchrotron crystallography. *Lab. Chip* **20**, 3888–3898 (2020).
56. Maeki, M. *et al.* Room-temperature crystallography using a microfluidic protein crystal array device and its application to protein–ligand complex structure analysis. *Chem. Sci.* **11**, 9072–9087 (2020).
57. Junius, N. *et al.* A microfluidic device for both on-chip dialysis protein crystallization and *in situ* X-ray diffraction. *Lab. Chip* **20**, 296–310 (2020).
58. Gavira, J. A. *et al.* Attaining atomic resolution from *in situ* data collection at room temperature using counter-diffusion-based low-cost microchips. *Acta Crystallogr. Sect. Struct. Biol.* **76**, 751–758 (2020).

59. Guha, S., Perry, S. L., Pawate, A. S. & Kenis, P. J. A. Fabrication of X-ray compatible microfluidic platforms for protein crystallization. *Sens. Actuators B Chem.* **174**, 1–9 (2012).
60. Keller, N. *et al.* Tacky cyclic olefin copolymer: a biocompatible bonding technique for the fabrication of microfluidic channels in COC. *Lab. Chip* **16**, 1561–1564 (2016).
61. Su, Y. *et al.* Impermeable barrier films and protective coatings based on reduced graphene oxide. *Nat. Commun.* **5**, 4843 (2014).
62. Zhang, L. *et al.* Crystal structure of SARS-CoV-2 main protease provides a basis for design of improved α-ketoamide inhibitors. *Science* **368**, 409–412 (2020).
63. Asherie, N., Ginsberg, C., Greenbaum, A., Blass, S. & Knafo, S. Effects of Protein Purity and Precipitant Stereochemistry on the Crystallization of Thaumatin †. *Cryst. Growth Des.* **8**, 4200–4207 (2008).
64. Pham, T. *et al.* Well-ordered self-assembled monolayer surfaces can be used to enhance the growth of protein crystals. *Colloids Surf. B Biointerfaces* **34**, 191–196 (2004).
65. Foroughi, L. M., Kang, Y.-N. & Matzger, A. J. Polymer-Induced Heteronucleation for Protein Single Crystal Growth: Structural Elucidation of Bovine Liver Catalase and Concanavalin A Forms. *Cryst. Growth Des.* **11**, 1294–1298 (2011).
66. McPhillips, T. M. *et al. Blu-Ice* and the *Distributed Control System* : software for data acquisition and instrument control at macromolecular crystallography beamlines. *J. Synchrotron Radiat.* **9**, 401–406 (2002).
67. Winter, G. *xia2* : an expert system for macromolecular crystallography data reduction. *J. Appl. Crystallogr.* **43**, 186–190 (2010).
68. Winn, M. D. *et al.* Overview of the *CCP* 4 suite and current developments. *Acta Crystallogr. D Biol. Crystallogr.* **67**, 235–242 (2011).
69. Winter, G. *et al. DIALS* : implementation and evaluation of a new integration package. *Acta Crystallogr. Sect. Struct. Biol.* **74**, 85–97 (2018).
70. McCoy, A. J. *et al. Phaser* crystallographic software. *J. Appl. Crystallogr.* **40**, 658–674 (2007).
71. Adams, P. D. *et al. PHENIX* : a comprehensive Python-based system for macromolecular structure solution. *Acta Crystallogr. D Biol. Crystallogr.* **66**, 213–221 (2010).
72. Afonine, P. V. *et al.* Towards automated crystallographic structure refinement with *phenix.refine*. *Acta Crystallogr. D Biol. Crystallogr.* **68**, 352–367 (2012).
73. Emsley, P. & Cowtan, K. *Coot* : model-building tools for molecular graphics. *Acta Crystallogr. D Biol. Crystallogr.* **60**, 2126–2132 (2004).
74. *PACKAGING WITH TOPAS® COC*. 7–8 https://topas.com/sites/default/files/Packaging-28.04.20_0.pdf.
75. Greenspan, L. Humidity fixed points of binary saturated aqueous solutions. *J. Res. Natl. Bur. Stand. Sect. Phys. Chem.* **81A**, 89 (1977).
76. Miller, R. L. & Boyer, R. F. Regularities in x-ray scattering patterns from amorphous polymers. *J. Polym. Sci. Polym. Phys. Ed.* **22**, 2043–2050 (1984).
77. Ko, T.-P., Day, J., Malkin, A. J. & McPherson, A. Structure of orthorhombic crystals of beef liver catalase. *Acta Crystallogr. D Biol. Crystallogr.* **55**, 1383–1394 (1999).
78. White, T. A. *et al. CrystFEL* : a software suite for snapshot serial crystallography. *J. Appl. Crystallogr.* **45**, 335–341 (2012).
79. Uervirojnangkoorn, M. *et al.* Enabling X-ray free electron laser crystallography for challenging biological systems from a limited number of crystals. *eLife* **4**, e05421 (2015).

3.7 Supporting Information

Section S1: Detailed protocol for the fabrication of cyclic olefin copolymer (COC) microfluidic chips.

A) Fabrication of a primary silicon mold

A primary silicon mold was fabricated by Ravata Solutions (Davis, CA, USA). Briefly, a 16-µm thick layer of a negative photoresist NR78-8000P (Futurrex Inc., Franklin, NJ, USA) was spun on a 150 mm silicon wafer (#590, University Wafer Inc., Boston, MA, USA) at 800 rpm for 40 seconds followed by a soft bake at 150 ºC for 1 minute. An EVG 620 contact aligner was used to expose the photoresist-coated wafer through a transparency photomask (CADArt Services, Brandon, OR, USA) at 260 mJ/cm^2 followed by a post-exposure bake at 110 ºC for 2.5 minutes. The wafer was developed in a TMAH-based developer for 1 minute. Plasmatherm ICP Deep Silicon Etcher was used to selectively etch 300-µm deep features in the silicon wafer. The photoresist was stripped using a DMSO-based stripper. The silicon mold surface was activated using a 30-minute UV-ozone treatment in a Jelight 42 UV-O Cleaner to generate surface hydroxyl groups. Vapor phase silanization was carried out in a vacuum desiccator with some modification of the protocol described by Bhushan et. al. [1] to deposit a passivating self-assembled layer of 1H,1H,2H,2H-perfluorodecyltrichlorosilane (FDTS, #SIH5841.0, Gelest Inc., Morrisville, PA, USA) on the surface of the silicon mold to allow for easy detachment of the secondary PDMS mold.

B) Fabrication of a secondary Sylgard 184 (PDMS) mold

The two-part Sylgard 184 silicone elastomer kit (PDMS) was mixed in a weight ratio of 5:1 monomer to curing agent and degassed in a vacuum desiccator for 30 minutes. Heavy-duty aluminum foil was used to create a walled reservoir around the silanized silicon mold. The

degassed PDMS mixture was poured into the reservoir and placed in a pressure chamber at 30 psi for 5 minutes to displace or dissolve any air bubbles entrapped in the micropatterned features. The reservoir-mold was subsequently placed on a level surface in a laboratory oven at 120 ºC for 1 hour to cure the PDMS mixture. Once cooled, a scalpel was used to carefully cut and detach the cured-PMDS mold (~5-inch diameter) from the silicon primary. The smooth side of the PDMS secondary mold and a new 150-mm silicon wafer were oxygen-plasma treated for 60 s at 50 W, 0.79 Torr, 25 sccm O_2 using a Plasma Equipment Technical Services (PETS) RIE system and immediately brought into contact and placed on a hot plate at 120 ºC for 1 hour to bond the two surfaces together. The patterned PDMS mold surface was passivated with a self-assembled monolayer of FDTS as described above.

C) Hot-embossing through-holes in COC sheets

A 500-nm sacrificial layer of water-soluble poly vinyl alcohol (PVA, #363170, Millipore Sigma, St. Louis, MO, USA) was spin-coated onto a UVO-treated silicon wafer by dispensing 3-4 mL of 9 wt.% PVA solution in MilliQ water at 2000 rpm for 60 seconds. The wafer was softbaked at 100 ºC for 10 minutes. A 240-µm thick sheet of cyclic olefin copolymer (Europlex 0F304, Roehm America LLC, Sanford, ME, USA) was adhered to the PVA-coated wafer using an intermediate "glue" layer of spin-coated 15 wt.% COC 8007 dissolved in sec-butylbenzene. The water-soluble PVA layer served a dual purpose as an adhesion promoting layer and sacrificial layer to allow controlled detachment of the COC sheet when required.

Hot embossing was performed with a EVG501 semi-automated wafer bonding system. The PDMS secondary mold was placed on the bottom platen with the COC/PVA coated Si wafer resting on top of the mold features. The temperature was first ramped up to 120 ºC and then 12 kN of force was applied for 15 min under high vacuum (7.5E-6 Torr). The assembly was allowed to cool below

the glass transition temperature (Tg = 78ºC) of COC under pressure before raising the piston and demoulding the embossed film. The residual 20-30 µm COC layer was etched using oxygen plasma treatment in the PETS RIE instrument (500 W, 330 mTorr, 25 sccm O_2, 30 minutes). The wafer was immersed in a water bath to dissolve the PVA layer and release the 200-micron thick COC supports with through-holes.

D) Laser cutting

A double-sided pressure sensitive adhesive layer (3M F9460PC) was attached to 0.5- or 1-mm sheets of poly methyl methacrylate (PMMA, Clarex optical grade cast acrylic, Astra Products, Copiague, NY, USA) and laser cut using a Trotec Speedy 400 CO_2 laser cutter to make rigid frames with inlet and outlet ports. Similarly, a 25-µm or 48-µm spacer film (AR 92734 and AR 92712 respectively, Adhesives Research Inc., Glen Rock, PA, USA) was laser cut to make the sample flow layer.

E) Solvent bonding and chip assembly

COC thin films of desired thicknesses 2-5 µm were spin-coated onto a UV-ozone treated silicon wafer and softbaked as described above. Hot-embossed COC supports were placed on a stack of filter papers soaked with a solution of 35:65 vol.% cyclohexane: acetone for 30-60 seconds and dried with a nitrogen gun to turn the surfaces "tacky" as described by Keller et al. [2]. The solvent treated side was brought into contact with the spin-coated film (on a silicon wafer) and manually pressed to bond the two together. The PMMA frames (with adhesive) were adhered to the respective top and bottom side COC supports by aligning inlet/outlet features in the two layers. The edges of the assembly were scored with a scalpel and released gently by immersion in a water bath. The COC thin film has very low adhesion to the silicon wafer and a PVA sacrificial layer was not found necessary for detachment. The COC thin film surface was hydrophilized using

atmospheric plasma treatment for 3 minutes on the high setting in a Harrick PDC-32G Basic Plasma Cleaner before being using in the chip assembly. The top and bottom sides of the chip were bonded using the pressure-sensitive adhesive flow layer by aligning the micropatterned windows to create an enclosed microfluidic chip. A contact dwell time of 24-72 hours was required to ensure strong adhesion between all the layers before using the chip.

Section S2: COC grade 8007 spin curves.

10-20 wt.% COC pellets (Grade 8007, T_g = 78 ºC; #24750, Polysciences Inc., Warrington, PA, USA) were dissolved in sec-butylbenzene (b.p. 174 ºC; TCI Chemicals, Portland, OR, USA) overnight on a hot plate at 150 ºC. A Millex-SV 5.0 µm syringe filter was used to filter the solution prior to spin-coating. 3-5 mL of solution was dispensed on a 5-inch UV-ozone treated silicon wafer and spun at a speed of 1000-4000 rpm. The wafers were softbaked at 100 ºC for 10 minutes prior to use. The spin curves are shown in **Figure S1**.

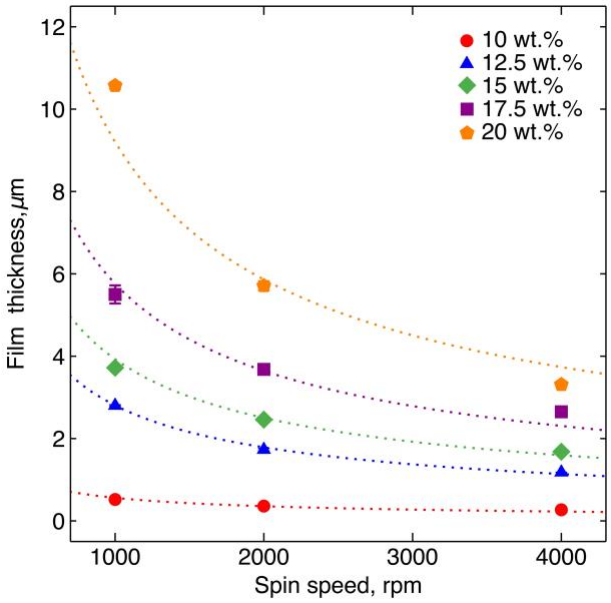

Figure S1: Spin curves showing COC film thickness as a function of spin speeds for different concentrations of COC 8007 dissolved in sec-butylbenzene. The dotted lines are fitted curves capturing the inverse relationship between dry film thickness and spin speed using equation $T = \frac{G}{\omega^{\alpha}}$, where T is the film thickness, ω is the spin speed and G and α are fitted parameters. An α value of 0.65 accurately captured the trends for all concentrations except for the solution with the highest viscosity (20 wt.% COC).

Section S3: Contact angle measurements of oxygen-plasma treated COC films.

A Ramé-Hart goniometer was used to measure the advancing and receding contact angles for COC thin films attached to both a silicon wafer and a COC support frame. After measuring the native surface contact angle, the films were atmospheric-plasma treated for 3 minutes using a Harrick PDC-32G Basic Plasma Cleaner to render them hydrophilic. Weekly measurements were taken on samples stored under ambient conditions over a period of four weeks. The average and standard deviation values reported are from n=5 independent measurements. The receding contact angles after plasma treatment (not shown) were consistently less than 10-20° over the duration of the study.

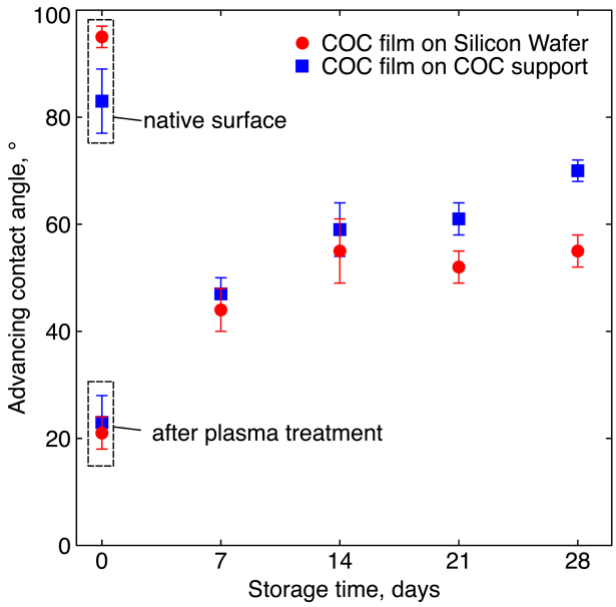

Figure S2: Contact angle measurements for COC 8007 thin films show a large decrease in the advancing contact angle from ~ $83 - 95°$ for the native COC surface to ~ $22°$ after atmospheric plasma treatment. Upon storage in ambient conditions, reorganization of surface groups at the COC-air interface results in a fast recovery to ~$47°$ and ~$59°$ after 1 and 2 weeks respectively, beyond which the increase is significantly slower.

Section S4: Sample loading into the microfluidic chip.

Hydrophilic surface treatment of the COC films prior to chip assembly enabled facile loading of aqueous solutions into the chip using a standard 10-µL micropipette. Assembled chips could be stored under ambient conditions for up to 2-4 weeks prior to use while still retaining sufficient wetting properties. While filling the chip with crystallization solution, it was important to ensure that the micropipette tip created a good seal when placed at the inlet to ensure the solution filled the flow/spacer layer instead of pooling at the inlet. A quick, one-step dispense was used to fill the chip in order to maintain the solution "front" such that the entire chip was filled without entrapping any air bubbles at the center where the spacer was unsupported.

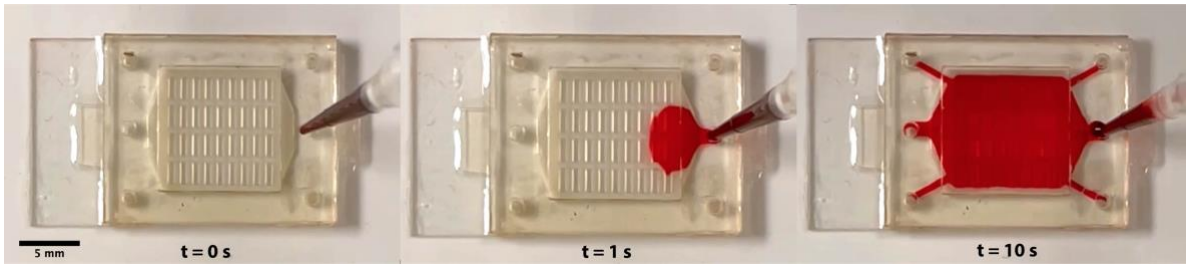

Figure S3: Snapshots of the COC microfluidic chip being loaded with ~8-10 µL of red dye solution over a 10-second period. The corner vents in the spacer layer (48 µm) allowed the wide flow chamber to fill uniformly with minimal bubble entrapment.

Section S5: Microscopy images of all protein crystals used in this work, grown on-chip.

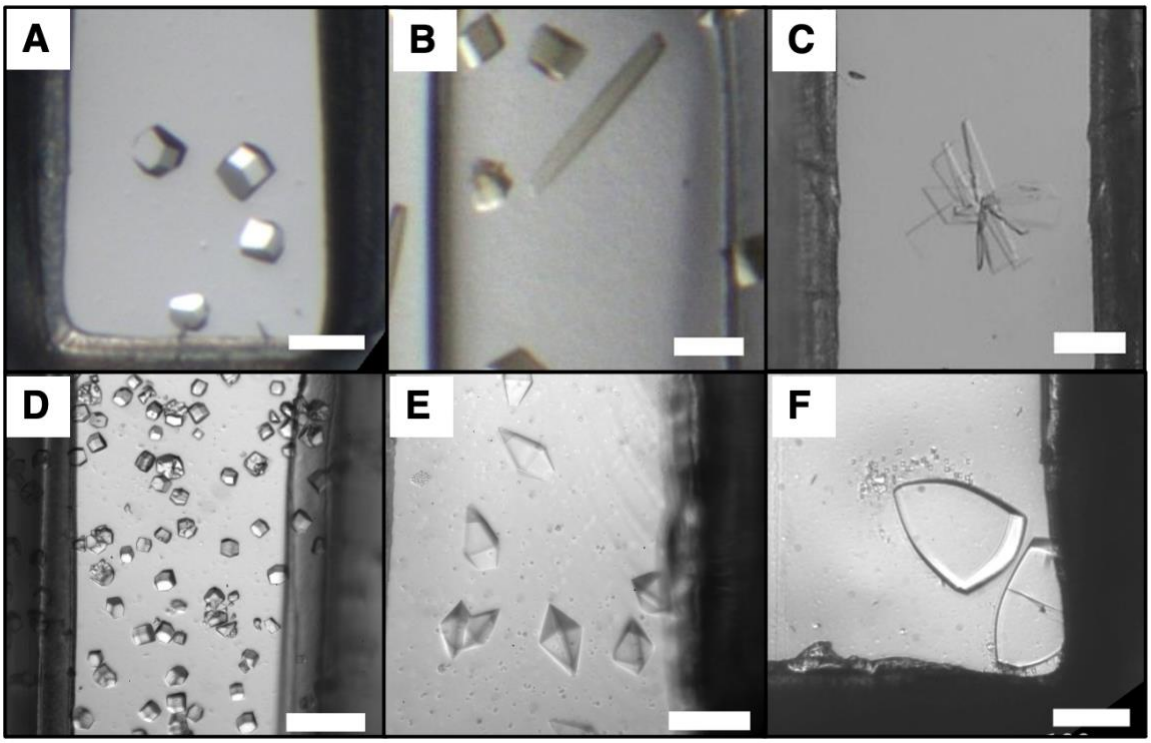

Figure S4: Optical microscopy images of all protein crystals used in this work, grown on-chip using micro-batch or vapor diffusion crystallization using conditions described in Table 1. (A) Lysozyme "aged", (B) catalase, (C) NSP5, (D) lysozyme "fresh", (E) thaumatin, (F) concanavalin-A. The scale bar is 200 µm.

Section S6: A comparison of merging statistics between fully hydrated and partially hydrated (excess buffer removed) catalase crystals.

A comparison of merging statistics between fully hydrated catalase crystals and ones with surrounding buffer removed did not show any significant changes in the unit cell parameters (~ 0.1 Å contraction). Slight improvements in the statistics for the second dataset can be explained by the fact that more crystals were included in the analysis.

Table S1: A comparison of merging statistics between fully hydrated catalase crystals and crystals with surrounding buffer removed.

Protein	**Catalase (in solution)**	**Catalase (solution removed)**
Resolution range ($\dot{A}$)	71.01 – 2.46	79.30 – 2.28
	(2.50 - 2.46)	(2.32 – 2.28)
Unit cell dimensions	$a = b$ = 141.88 $\dot{A}$,	$a = b$ = 141.751 $\dot{A}$,
	c = 103.523 $\dot{A}$,	c = 103.461 $\dot{A}$,
	$\alpha = \beta$ = 90°, γ = 120°	$\alpha = \beta$ = 90°, γ = 120°
Space group	$P3_221$	$P3_221$
Data processing statistics		
Total reflections	203188 (8841)	790087 (38202)
Unique reflections	43769 (2111)	55195 (2684)
Multiplicity	4.6 (4.2)	14.3 (14.2)
Completeness (%)	98.9 (96.3)	100.0 (98.6)
Mean $I/\sigma(I)$	7.2 (0.8)	9.0 (0.8)
R_{merge}	0.218 (2.168)	0.192 (2.387)
R_{meas}	0.244 (2.453)	0.199 (2.476)
R_{pim}	0.106 (1.119)	0.052 (0.651)
$CC_{1/2}$	0.949 (0.212)	0.997 (0.584)
Wilson B-factor	41.36	44.16

Section S7: A comparison between structures obtained in this work and the respective PDB references used as templates for phasing via molecular replacement.

PyMOL (*align* command) was used to perform secondary structure-based alignment of the structure solved in this work and the respective PDB reference used for phasing via molecular replacement. The alignment returned a root mean squared deviation (RMSD) value that quantitates the average deviation (in Å) of each atom in a structure from the corresponding atom in the reference structure.

Table S2: Root mean square deviation (RMSD, Å) between structures obtained in this work and the respective PDB references used as templates for phasing via molecular replacement.

Structure (this work)	PDB reference	RMSD, Å
Lysozyme (fresh)	1VED	0.249
Lysozyme (aged)	1VED	0.238
Thaumatin	1RQW	0.118
Catalase	8CAT	0.313
Concanavalin-A	1SCR	0.121
NSP5	6CR3	0.416

Section S8: Effects of excess mother liquor exclusion on background scatter

On-chip crystal growth offers several opportunities to reduce the mother liquor derived background scattering of a chip-based measurement. Under certain conditions where growth of relatively large single crystals is favorable, the spacer layer thickness may limit crystal size, leading to crystal growth that spans the chip fluid layer and excludes excess mother liquor from the beam path as demonstrated for concanvalin-A (**Figure S5**). Interactions with the enclosing films may also allow for physical removal of the mother liquor while leaving crystals in place, reducing mother liquor derived background scattering as demonstrated for catalase (**Figure S6**).

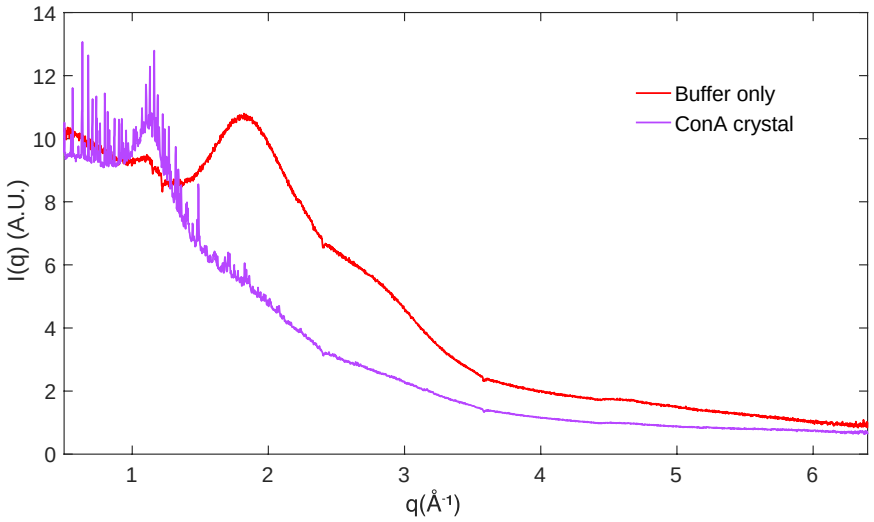

Figure S5: Radial averages of scattering from chip-spanning crystals of concanavalin-A (ConA, Purple, average of three frames where the beam is perpendicular to the chip plane), compared to a buffer filled chip. Both are measured in chips with 3.7 µm COC enclosing films and 48 µm spacer layers. On-chip crystal growth in this case excludes the majority of buffer from the beam path, leading to a significantly diminished water solvent ring at ~q = 1.8 Å^{-1}.

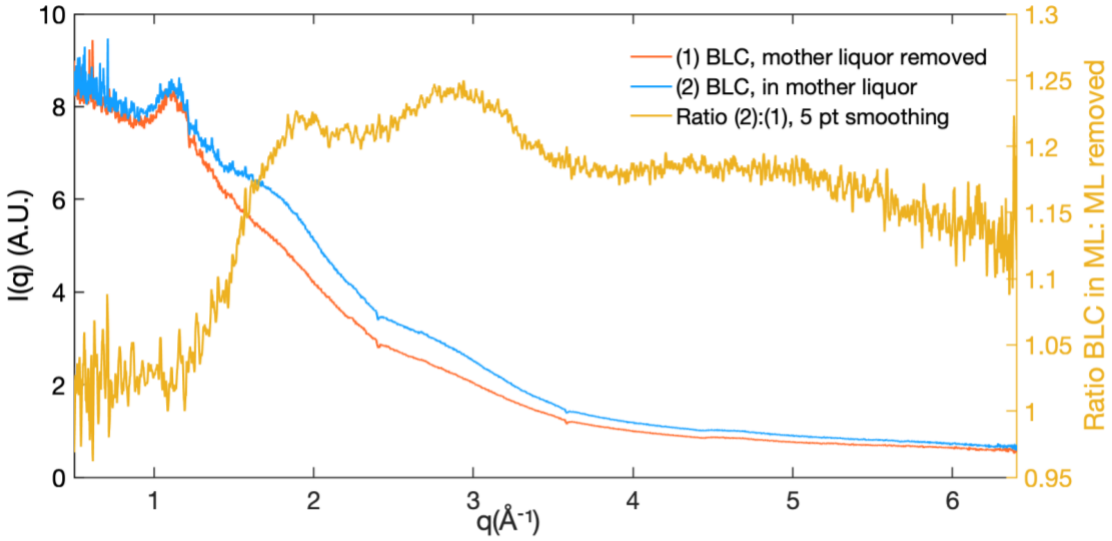

Figure S6: Radial averages of scattering from comparably sized bovine liver catalase (BLC) crystals in two hydration environments (average of three frames where the beam is perpendicular to the chip plane): one surrounded by mother liquor (Blue) and one with mother liquor removed (orange). Mother liquor removal slightly decreases the contribution of the water solvent ring at ~q = 1.8 Å^{-1}. Both are measured in chips with 3.7 µm COC enclosing films and 48 µm spacer layers. The right axis shows the ratio of the radial intensity before mother liquor removal to the intensity after mother liquor removal with five-point smoothing (yellow).

SI References

1. Bhushan, B., Hansford, D. & Lee, K. K. Surface modification of silicon and polydimethylsiloxane surfaces with vapor-phase-deposited ultrathin fluorosilane films for biomedical nanodevices. *J. Vac. Sci. Technol. Vac. Surf. Films* **24**, 1197–1202 (2006).
2. Keller, N. *et al.* Tacky cyclic olefin copolymer: a biocompatible bonding technique for the fabrication of microfluidic channels in COC. *Lab. Chip* **16**, 1561–1564 (2016).

3.8 Appendix II

3.8.1 On-chip patterning of COC films for controlling crystal locations and densities on-chip

Project background

Both specific interactions like ligand binding, and non-specific interactions like hydrophilicity/hydrophobicity, electrostatics can be tuned to influence protein organization at an interface and affect protein crystallization kinetics[1–4]. The goal of this work was to study whether these interactions could be used to promote crystal nucleation and growth in desired locations on our COC polymer microfluidic chip to maximize sample hit rate during raster scanning for high-throughput serial data collection. Our initial focus was on studying the effect of surface charge on site-selective crystallization of model proteins using previously established crystallization conditions.[5,6,3]

COC can be patterned readily using photo-induced polymerization of acryl monomers to produce cross-linked polymer brushes that are covalently attached to carbon atoms on the polymer surface.[7–9] In this work, acrylic acid monomers were chosen to produce poly-acrylic acid (PAA) brushes (isoelectric point, IEP ~ 3) resulting in a net negative surface charge over the pH range typically investigated in crystallization screens (3.5-10). Two different approaches were taken to produce net positively charged surfaces. The first approach involved using acid-amine coupling reactions to derivatize the carboxyl groups in PAA into cationic tertiary amines. This was achieved

by first activating the carboxyl groups using reactive 1-ethyl-3-(3-dimethylaminopropyl)carbodiimide (EDC) and N-hydroxysuccinimide (NHS) to produce dry-stable COC-PAA-NHS esters, followed by a reaction with N,N-dimethylethylenediamine (DMEN), an asymmetric diamine with a reactive primary amine and an unreactive cationic tertiary amine, to produce positively charged polymer brushes (IEP ~ 8.7).[10] The second approach involved incubation of PAA-grafted COC surfaces with a branched 25k MW polyelectrolyte polyethyleneimine (PEI) which has primary (34%), secondary (40%) and tertiary (26%) amines (composition from Sigma Aldrich product specifications, #408727) with pKa values of 4.5, 6.7 and 11.6 respectively.[11,12] Surface crystallization tests with two model basic proteins, lysozyme (14.3 kDa, IEP~10-11[13]) and thaumatin (22 kDa, IEP~11-12[14]), and one model acidic protein, concanavalin-A (26.5 kDa monomer, exists as a tetramer > pH 7, IEP~ 4.5-5.5[15,16]) were performed using micro-batch crystallization in a surface-modified COC well plate fabricated in-house.

Materials and Methods

Photochemical modification

A modified version of the protocol described in Rohr, T. et al[7] was used for the UV-photografting reaction. 2-5 µm COC 8007 films spin-coated on UV-ozone treated silicon wafers were used as substrates for photochemical modification. Direct modification of COC thin films attached to microfabricated COC-PMMA supports frames on the microfluidic chips (Chapter 3 Figure 1, layers 2-4) was possible but required substrate cooling during the reaction to avoid damaging the thin films from the heat released during the polymerization reaction (COC Tg ~ 78 °C). This was achieved by adding a few drops of milliQ water to the back side of the microfabricated assembly and freezing it to crease a heat sink. A grafting solution was prepared by mixing acrylic acid

monomers, 5 wt.% benzophenone in methanol, and milliQ water in a 3:3:4 volume ratio. After vigorous mixing until the solution was clear, the solution was degassed under house vacuum and filtered through a 0.22 µm PTFE syringe filter. To functionalize the COC films, the grafting solution was applied to the surface and covered with a quartz photomask with the chrome patterned side down to minimize deflection of the UV light. A sample holder was machined in-house to control the spacing between the photomask and the COC surface to be ~100 µm as shown in **figure A1(a)**. After sample assembly, the holder was placed under the UV light (UVP Blak-Ray B-100A, 100 W, 365 nm longwave UV) inside a black box. The distance of the sample holder from the UV lamp bulb was held constant at 7.0 inches (intensity ~ 10 mW/cm^2) and the irradiation time was adjusted based on the desired feature size and brush thickness. Smaller feature sizes and thicker brushes needed longer irradiation time. After the reaction, the COC films were rinsed using ethanol to remove unpolymerized acrylic acid monomers and dried using a nitrogen stream to produce patterned COC-PAA films as shown in **figure A1(b)**. A schematic of the reaction is shown in **figure A2(a).**

Subsequent chemical functionalization

A modified version of the protocol described in Risse, F. et al[10] was used in for the DMEN derivatization reaction. The carboxyl groups on the COC-PAA films or chips were activated by incubating the patterned surface with a freshly prepared solution of 250 mM NHS: 500 mM EDC in 100 mM MES buffer, 100 mM NaCl pH 5.5 on top for 30 minutes. The resulting surface was immediately rinsed using milliQ water rise and dried using a nitrogen stream to produce dry-stable COC-PAA-NHS esters. Derivatization using DMEN was performed by incubating the NHS-ester activated COC-PAA surfaces with 0.85 M DMEN in 100 mM MES buffer, 100 mM NaCl pH 6.5 for 10 or 30 minutes. The resulting surface was rinsed using milliQ water and dried using a nitrogen

stream to produce COC-DMEN surfaces. A schematic of the reaction is shown in **Figure A2(b).** PEI modified surfaces were produced by incubating COC-PAA surfaces with 1.3 mg/mL PEI dissolved in milliQ water overnight, followed by rinsing and drying.

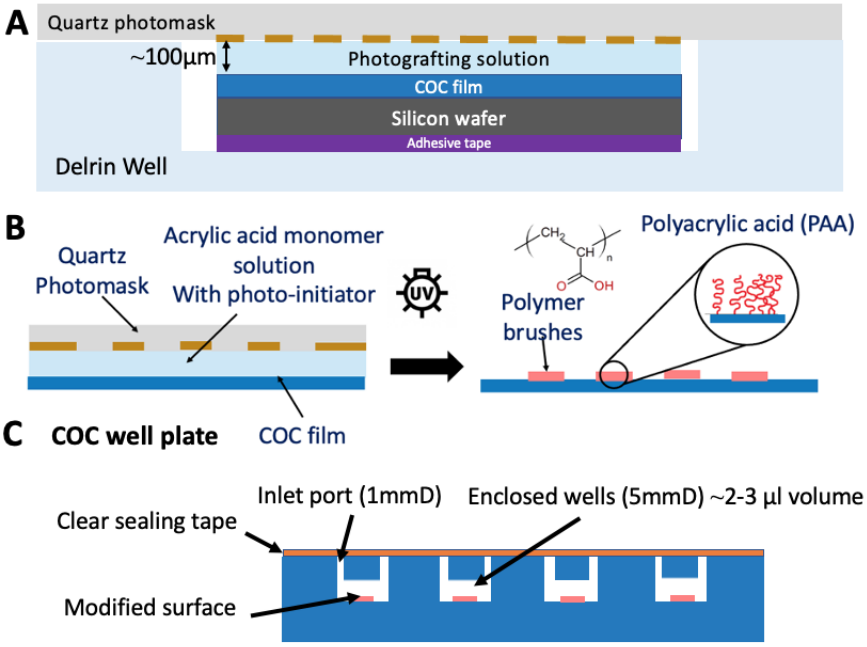

Figure A1: A schematic of the (a) sample holder setup for UV-photografting of COC thin films on silicon wafers, (b) patterned COC-PAA surface, (c) COC well plate used for micro-batch crystallization of proteins on functionalized surfaces.

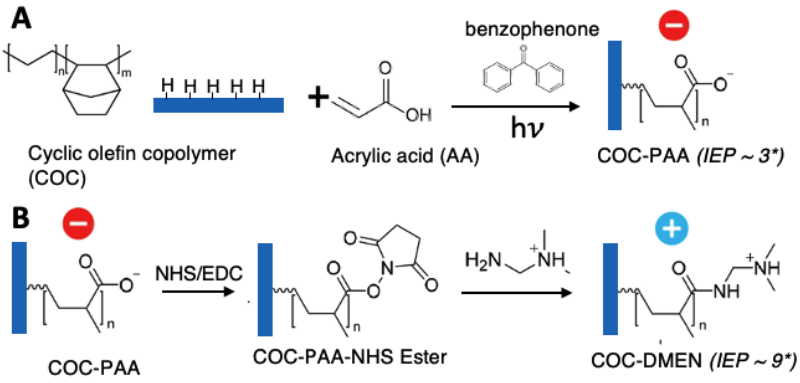

Figure A2: A schematic of the (a) UV-photografting reaction between COC and acrylic acid monomers to produce covalently grafted, branched PAA brushes, (b) subsequent derivatization to produce cationic tertiary amines using NHS/EDC coupling chemistry and reaction with DMEN. *IEP based on surface potential measurements in 1 mM KCl.[7]

Surface characterization

COC thin films with and without surface modifications were transferred to a transparent 240 µm thick COC sheet prior to attenuated total reflection Fourier transform infrared spectrometry (ATR-FTIR). Spectra were recorded using a Thermo Nicolet 6700 FTIR spectrometer at 4 cm^{-1} resolution using a ZnSe crystal with an incidence angle of 45°. OMNIC software (Thermo Fisher Scientific) was used for data acquisition. A Dektak 150 stylus profilometer was used to determine the dry grafted brush thickness.

Protein crystallization on the modified surface

A COC well plate was fabricated using functionalized thin films transferred to a thick COC sheet, additional layers cut using a Cricut cutting plotter, assembled using solvent bonding or pressure sensitive adhesive tapes, **figure A1(c)**. The protein crystallization solution was introduced into the wells using inlet holes, after which the holes were sealed using Hampton crystal clear tape to mimic micro-batch crystallization conditions (**Table A1).** Optical microscopy was used monitored the well plates for crystals daily. In almost all cases crystals were observed within one week of setup.

Table A1: Micro-batch crystallization conditions used in this work. Protein and precipitant solutions were mixed 1:1, gently mixed by pipetting, and introduced into the well plate.

Protein	Protein solution	Precipitant solution
Lysozyme	30 mg/mL in 20 mM sodium acetate buffer, pH 4.6	1 M sodium chloride, 0.1 M sodium acetate buffer, pH 4.6
Thaumatin	25 mg/ml in milliQ water	1 M L-sodium potassium tartrate, 0.1 M ADA buffer, pH 6.5
Concanavalin-A (Type VI)	30 mg/mL in 20 mM tris buffer, pH 8.0	2.8 M ammonium sulfate, 0.1 M tris buffer, pH 7.5

Results and discussion

Surface characterization

Figure A3 shows the ATR-FTIR spectra for bare COC, and the different surface-modified films used in this work. For unmodified COC (red curve), the observed IR bands ~1460 cm^{-1} (C-H bending) and ~2860, 2940 cm^{-1} (C-H stretch) are in good agreement with previous reports.[9] The other spectra were collected on COC films grafted with 200 ± 50 nm thick PAA brushes (irradiation time = 10 minutes, ~10 mW/cm^2) with or without subsequent derivatization. The observed carboxyl C=O stretch band ~1712 cm^{-1} in the blue COC-PAA curve confirms the presence of carboxylic acid groups. The green COC-PAA-NHS ester curve has a similar peak at ~1712 cm^{-1}. The increase in the carbonyl peak intensity and the appearance of a shoulder ~1655 cm^{-1} could be attributed to the carbonyl in the amide groups in the NHS moiety. DMEN derivatization of the PAA-NHS ester resulted in the disappearance of the carboxyl C=O stretch peak (~1712 cm^{-1}), an increase in the ~1655 cm^{-1} band peak (amide C=O stretch), and the appearance of N-H bending (1565 cm^{-1}) and stretching bands (3400 cm^{-1}, 3280 cm^{-1}), the intensity of which depended on the DMEN reaction time (10 vs. 30 minutes). The deposition of polyelectrolyte PEI on COC-PAA also resulted in the disappearance of the carboxyl C=O stretch peak (~1712 cm^{-1}) and the appearance of amide C=O stretch, N-H bend, and N-H stretch bands, but the peak intensities differed from COC-DMEN surfaces which could be attributed to the different polymer composition of PEI.

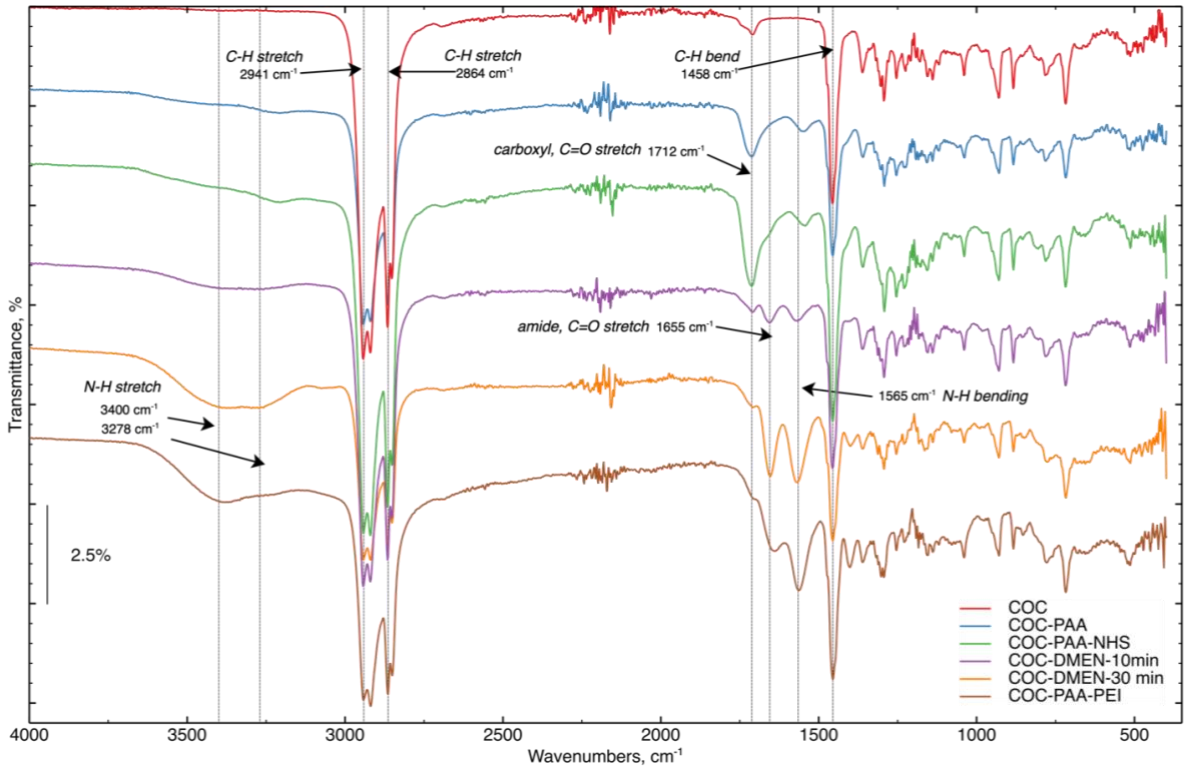

Figure A3: ATR-FTIR spectra for bare COC and modified COC surfaces used in this work.

Protein crystallization

Figure A4 shows a COC surface with 100 µm square pattern of PAA brushes (~200 nm, dry thickness) before protein crystallization. Our crystallization experiments on surface modified COC chips showed that even in high ionic strength crystallization solutions, where counterions are expected to screen surface charge significantly, short range electrostatics interactions at the charged polymer surfaces influenced protein crystallization.

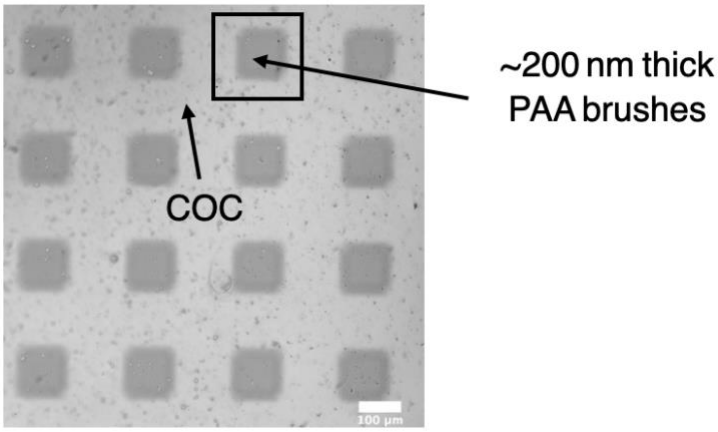

Figure A4: A COC thin film spin-coated on a silicon wafer with a 100 µm square pattern of PAA brushes covalently grafted on the surface using UV-photografting.

Lysozyme: **Figure A5** shows the effect of surface charge on crystallization of lysozyme over a period of ~6 days. Attractive electrostatic interactions are expected between positively charged lysozyme and the negatively charged PAA surfaces at the crystallization pH of 4.6. The extent of negative surface charge was found to affect both the kinetics of crystallization as well as the density of crystals in the surface modified patches. The fastest crystallization and the highest tetragonal crystal density were observed with COC-PAA. A similar crystal morphology was observed with COC-PAA-NHS, albeit with slower crystallization kinetics due to the lower negative surface charge (a significant fraction of the carboxylic acid groups was converted to NHS-esters). In case of DMEN modified surfaces a different rod-like crystal morphology was observed, likely due to differences in protein contacts with the surface and within the crystal lattice. A higher positive surface character led to slower crystallization kinetics (DMEN-10 vs DMEN-30). In case of COC-PAA-PEI surfaces, no crystallization was observed over the duration of this experiment (~1 week). Bulk crystallization was observed after 2-3 weeks both in bare-COC and COC-PAA-PEI wells (not shown). The difference in crystal morphology between the PAA and DMEN surfaces is shown in **figure A6**.

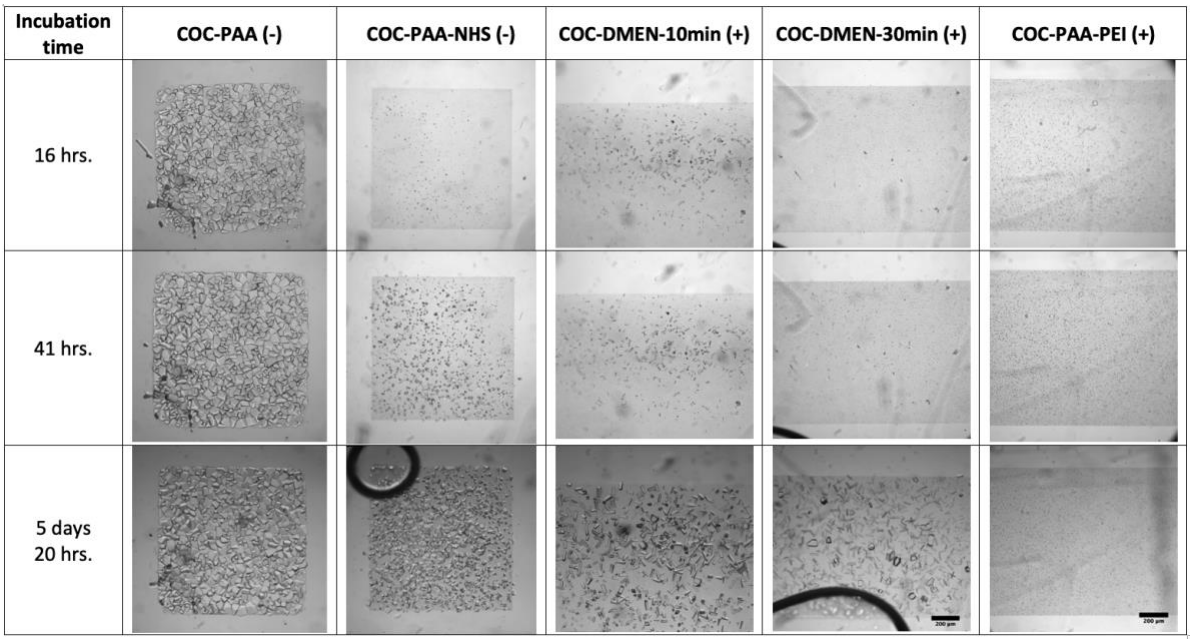

Figure A5: The effect of polymer brush surface charge on crystallization of lysozyme.

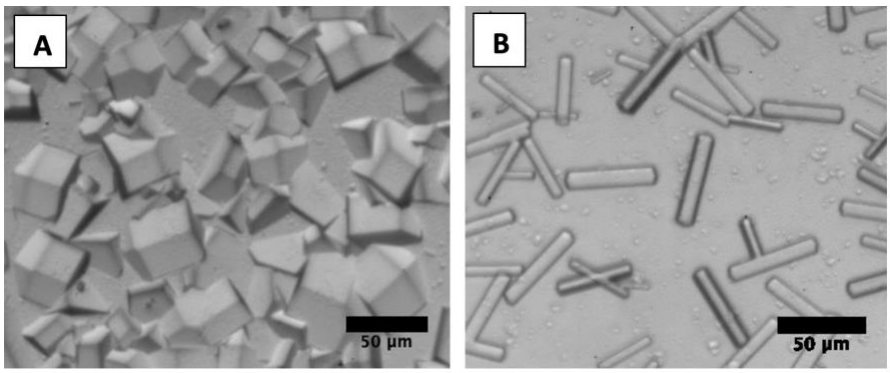

Figure A6: Cuboid and rod-like lysozyme crystal morphology on (a) COC-PAA surfaces and (b) COC-DMEN surfaces respectively.

Thaumatin: **Figure A7** shows the effect of surface charge on crystallization of thaumatin over a period of 2 days. At the crystallization pH of 6.5, thaumatin is expected to have a net positive charge like lysozyme. While no site-specificity in crystallization was observed with this protein, the polymer brush surfaces appeared to influence crystal nucleation density, with higher degree of positive charge correlating with higher density of microcrystals. A lack of surface specificity in

crystallization for this protein could be explained by the fact that this model protein required the presence of tartrate ions in the precipitant solution to crystallize. Alternative precipitants reported in the literature like ammonium sulfate did not produce any crystals in our trials.

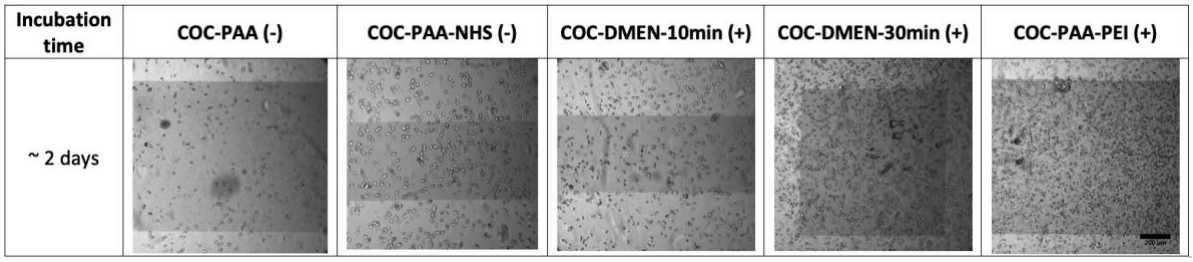

Figure A7: The effect of polymer brush surface charge on crystallization of thaumatin.

Concanavalin-A (Con-A): **Figure A8** shows the effect of surface charge on crystallization of con-A. At the crystallization pH of 7.5, con-A is expected to have a net negative charge. Attractive interactions are expected with the positively charged surfaces. However in this case as well site-specific crystallization was observed with COC-PAA, whereas the reverse was observed with COC-DMEN-30min where crystals were found to grow in the "bare-COC" regions as opposed to the square polymer brush regions.

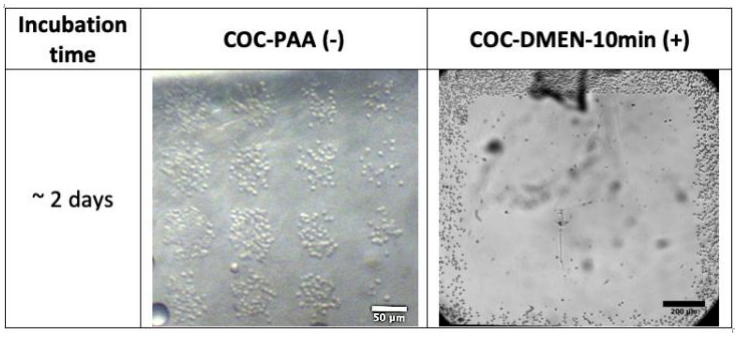

Figure A8: The effect of polymer brush surface charge on crystallization of con-A.

Outlook

This work shows that surface interactions could be used to guide site-selective crystallization, however surface charge interactions alone could not fully explain the variation in behavior observed between the three proteins studied in this work. Factors like polymer grafting density vs protein size, protein-precipitant interactions, magnitude of surface charge on protein and polymers also affected the bulk vs surface crystallization propensity and should be investigated systematically. High-throughput screens (96/ 396/1536 crystallization conditions) should be used to decouple the effects of pH, precipitant, and surface modifications. The NHS/EDC carboxyl coupling reaction can be used to (a) bind NTA-amine molecules for Ni-NTA affinity-based binding of his-tagged proteins and (b) immobilize avidin protein for specific binding with biotinylated proteins to explore additional methods for site-selective crystallization.

3.8.2 XFEL characterization of polymer microfluidic chips

Project background

The COC polymer microfluidic chips were tested for stability and serial femtosecond crystallography (SFX) data collection at an XFEL beamline. Experiments were conducted at the LCLS MFX beamline in air or in a helium chamber (HERA box) to reduce air scatter background. **Figure A9(a)** shows the COC chip mounted in the HERA box prior to measurements. Due to beam focusing constraints at the facility during our awarded time, majority of the data was collected using a 12 x 12 μm^2 FWHM microfocussed beam at 12 keV (Run18, proposal P163) with an additional short stability test done with a 5 x 5 μm^2 FWHM beam at 9 keV (more typical XFEL experimental parameters, higher X-ray absorption). The X-ray flux was ~2 mJ, and the X-ray transmission (5-100 %T of the full beam intensity) and shot-spacing (50-200 µm) were systematically varied to evaluate chip stability and establish optimal scan parameters to maximize hit-rate and diffraction resolution (minimize damage propagation). Two model protein samples

were studied – (1) randomly distributed 10-20 µm thaumatin crystals grown on-chip using micro-batch crystallization method with seeding to control nucleation density (**figure A9(b)**), and (2) PAA-functionalized and patterned COC films with 50 µm square or slot patterns with site-specifically grown lysozyme crystals (20-50 µm, **figure A9(c)**).

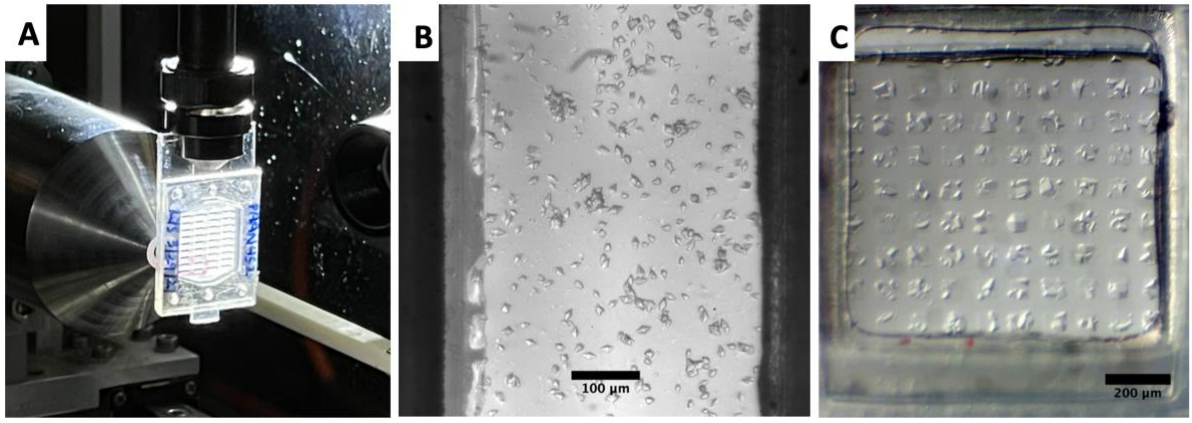

Figure A9: (a) The polymer microfluidic chip mounted in the HERA box at the LCLC MFX beamline. (b) Randomly distributed 10-20 µm thaumatin crystals grown on-chip using crystal seeding. (c) Patterned 20-50 µm lysozyme crystals grown on-chip in a 50/50 µm square grid layout on PAA-functionalized COC films.

Results and discussion

Chip stability

The chip was found to withstand the full XFEL beam intensity at 12 keV even with 100 %T and a 50 µm shot spacing when scanning at 10 Hz with no observable damage to the COC thin films after measurements, as shown in **figure A10(a)**. At the lower X-ray energy (9 keV) with the smaller beam focus, some discoloration of the COC films was observed when the chip was scanned at 10 Hz (with a 120 Hz pulse rate, n_{shots} = 12 per spot) for the two conditions tested 15 %T, 100 µm shot spacing and 30 %T, 50 µm shot spacing, as shown in **figure A10(b)**.

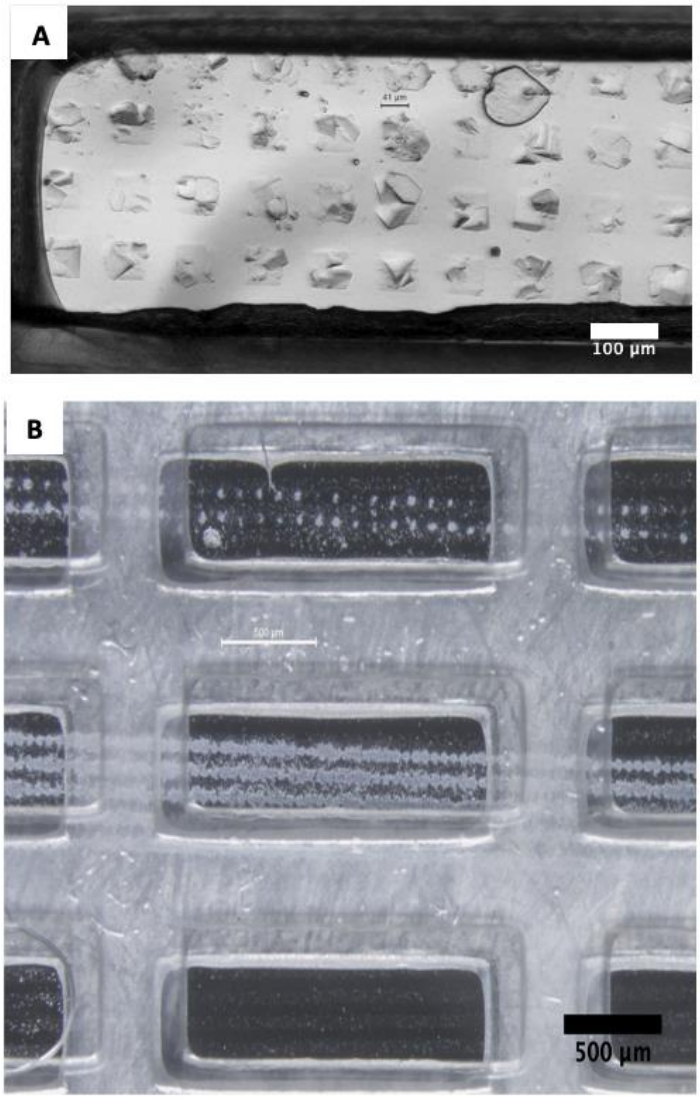

Figure A10: The polymer chip after raster scanning (a) at 12 keV with a 12x12 µm^2 beam at 100 %T, 50 µm shot spacing showing no damage to the COC film. Some crystal debris is observed.; (b) at 9 keV with a 5x5 µm^2 beam at 15 %T, 100 µm shot spacing (top row) and 30 %T, 50 µm shot spacing (middle row) showing some COC film discoloration but no pinhole defects or leaks. The bottom row (not scanned) shows ~10-20 µm lysozyme crystals grown on 50 µm wide PAA-patterned slots on the COC film that spanned the entire chip width.

Data analysis

High resolution data collection was demonstrated with our chips with max and average resolution of 1.1 Å and 2.1 Å respectively for the patterned lysozyme crystals. **Table A2** summarizes the run

wise sample hit rates (hit >=10 Bragg peaks) and indexing rates (% of hits accurately indexed) for data collected (12 keV) on the patterned lysozyme and randomly distributed thaumatin crystals, as a function of X-ray transmission % and shot spacing. Hit rates were consistently high for the two samples studied and varied between 25 to 75% based on the crystal density in the window scanned and the scanning parameters.

Table A2: A summary of hit rates and indexing rates for the two samples, lysozyme (patterned) and thaumatin (random) with different %T and shot spacings. A hit was defined as a diffraction snapshot with >=10 Bragg peaks.

	Runs	**Transmission, %**	**Shot spacing, µm**	**N, events**	**N, hits**	**Hit rate, %**	**N, indexed**	**Indexing rate (of hits), %**
Lysozyme	47	21	50	205	113	55	86	76
	48	30	50	210	124	59	95	77
	46	49	50	180	123	68	77	63
	29,43,44, 45	49	100	150	69	46	34	49
Thaumatin	52,53,54, 55	19	100	256	94	37	67	71
	56,57	19	50	480	117	24	61	52
	60	49	50	240	138	58	80	58
	61	100	50	272	199	73	90	45

Outlook

This work demonstrates that the polymer microfluidic chips developed by our group can withstand the significantly higher beam intensity at XFELs and produce high quality data with low background scatter, enabling easy and robust sample delivery for high-throughput SFX data collection. Future work will focus on testing stability with smaller focus beams (1-3 µm) for data collection from smaller microcrystals of scientifically interesting proteins as well as test the device for compatibility with in-vacuo characterization (for lower background scatter).

Appendix References

1. Falini, G., Fermani, S., Conforti, G. & Ripamonti, A. Protein crystallisation on chemically modified mica surfaces. *Acta Crystallogr. D Biol. Crystallogr.* **58**, 1649–1652 (2002).
2. Tosi, G., Fermani, S., Falini, G., Gavira Gallardo, J. A. & García Ruiz, J. M. Crystallization of proteins on functionalized surfaces. *Acta Crystallogr. D Biol. Crystallogr.* **64**, 1054–1061 (2008).
3. Foroughi, L. M., Kang, Y.-N. & Matzger, A. J. Polymer-Induced Heteronucleation for Protein Single Crystal Growth: Structural Elucidation of Bovine Liver Catalase and Concanavalin A Forms. *Cryst. Growth Des.* **11**, 1294–1298 (2011).
4. Sengupta Ghatak, A. & Ghatak, A. Disordered Nanowrinkle Substrates for Inducing Crystallization over a Wide Range of Concentration of Protein and Precipitant. *Langmuir* **29**, 4373–4380 (2013).
5. Pham, T. *et al.* Well-ordered self-assembled monolayer surfaces can be used to enhance the growth of protein crystals. *Colloids Surf. B Biointerfaces* **34**, 191–196 (2004).
6. Asherie, N., Ginsberg, C., Greenbaum, A., Blass, S. & Knafo, S. Effects of Protein Purity and Precipitant Stereochemistry on the Crystallization of Thaumatin †. *Cryst. Growth Des.* **8**, 4200–4207 (2008).
7. Rohr, T., Ogletree, D. F., Svec, F. & Fréchet, J. M. J. Surface Functionalization of Thermoplastic Polymers for the Fabrication of Microfluidic Devices by Photoinitiated Grafting. *Adv. Funct. Mater.* **13**, 264–270 (2003).
8. Stachowiak, T. B. *et al.* Hydrophilic surface modification of cyclic olefin copolymer microfluidic chips using sequential photografting. *J. Sep. Sci.* **30**, 1088–1093 (2007).
9. Pu, Q., Oyesanya, O., Thompson, B., Liu, S. & Alvarez, J. C. On-Chip Micropatterning of Plastic (Cylic Olefin Copolymer, COC) Microfluidic Channels for the Fabrication of Biomolecule Microarrays Using Photografting Methods. *Langmuir* **23**, 1577–1583 (2007).
10. Risse, F., Gedig, E. T. & Gutmann, J. S. Carbodiimide-mediated immobilization of acidic biomolecules on reversed-charge zwitterionic sensor chip surfaces. *Anal. Bioanal. Chem.* **410**, 4109–4122 (2018).
11. Choosakoonkriang, S., Lobo, B. A., Koe, G. S., Koe, J. G. & Middaugh, C. Russell. Biophysical Characterization of PEI/DNA Complexes. *J. Pharm. Sci.* **92**, 1710–1722 (2003).
12. Demadis, K. D., Paspalaki, M. & Theodorou, J. Controlled Release of Bis(phosphonate) Pharmaceuticals from Cationic Biodegradable Polymeric Matrices. *Ind. Eng. Chem. Res.* **50**, 5873–5876 (2011).
13. Proctor, V. A., Cunningham, F. E. & Fung, D. Y. C. The chemistry of lysozyme and its use as a food preservative and a pharmaceutical. *C R C Crit. Rev. Food Sci. Nutr.* **26**, 359–395 (1988).
14. Wel, H. & Loeve, K. Isolation and Characterization of Thaumatin I and II, the Sweet-Tasting Proteins from Thaumatococcus daniellii Benth. *Eur. J. Biochem.* **31**, 221–225 (1972).
15. Entlicher, G., Koštíř, J. V. & Kocourek, J. Studies on phytohemagglutinins. VIII. Isoelectric point and multiplicity of purified concanavalin A. *Biochim. Biophys. Acta BBA - Protein Struct.* **236**, 795–797 (1971).
16. Carrotta, R. *et al.* Amyloid Fibrils Formation of Concanavalin A at Basic pH. *J. Phys. Chem. B* **115**, 2691–2698 (2011).

CHAPTER 4: HOW WELL CAN YOU TAILOR THE CHARGE OF LIPID VESICLES?

Gilbile, D., Docto D., Kingi D.T., Kurniawan, J., Monahan D., Tang A., and Kuhl, T.L.

Department of Chemical Engineering, University of California at Davis, CA, USA.

Author Contributions

Conceptualization, D.G., J.K., T.L.K.; SFA measurements D.G., T.L.K.; DLS and Zeta Potential measurements D.G., D.D., D.T.K., D.M., A.T.; data evaluation and analysis, D.G., T.L.K.; writing, D.G., T.L.K.; All authors have read and agreed to the published version of the manuscript.

Status: Published in ACS Langmuir on October 13th, 2019.

DOI: https://doi.org/10.1021/acs.langmuir.9b02163

Keywords: Lipids, Membranes, Salts, Electrostatics, Surface charge, Vesicles, Supported lipid bilayers, Zeta potential, Surface force apparatus.

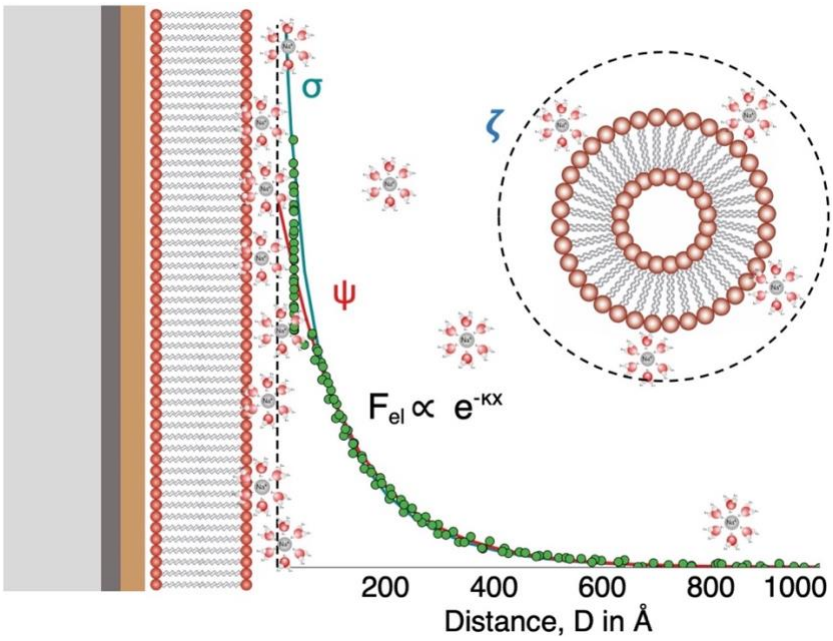

Abstract:

Knowledge and control of surface potential (or charge) is important for tailoring colloidal interactions. In this work we compare widely used zeta potential measurements of charged lipid vesicle surface potential to direct measurements using the surface force apparatus (SFA). Our measurements show good agreement between the two techniques. On varying the fraction of anionic lipids dimyristoylphosphatidylserine (DMPS) or dimyristoylphosphatidylglycerol (DMPG) mixed with zwitterionic dimyristoylphosphatidylcholine (DMPC) from 0 to 100 mol % we observed a near-linear increase in membrane surface charge/potential up to 20 - 30 mol% charged lipids beyond which charge saturation occurred in physiological salt conditions. Similarly, in low salt concentrations a linear increase in charge/potential was found, but only up to ~ 5 - 10 mol% charged lipids beyond which the surface potential/charge leveled off. While a lower degree of ionization is expected due to the lower dielectric constant (ε ~ 4) of the lipid acyl chain environment, increasing intra-membrane electrostatic repulsions between neighboring lipid head groups at higher charge loading contributes to charge suppression. Measured potentials in physiological (high) salt solutions were consistent with predictions using the Gouy-Chapman-Stern-Grahame (GCSG) model of the electrical double layer with Langmuir binding of counterions, but in low salt conditions, the model significantly overestimated the surface charge/potential. The much lower ionization in low salt (maximum fraction dissociated ~ 1 – 2 % of total lipids) instead was consistent with counterion condensation at the bilayer surface which limited the charge/potential that could be obtained. The strong interplay between membrane composition, lipid head group ionization, solution pH and electrolyte concentration complicates exact prediction and tuning of membrane surface charge or potential for applications. However, the theoretical frameworks used in the work can be used as guidelines to understand this interplay

and establish a range of achievable potentials for a system to tune or predict the response to triggers like pH and salt concentration changes.

4.1 Introduction

Biological membranes are largely composed of amphiphilic phospholipids which self-assemble to form a stable bilayer-like structure with a hydrophobic core of acyl-chains and a hydrophilic exterior consisting of lipid head groups bearing different moieties- zwitterionic, glycosylated or anionic.[2,3] Given the complexity of cellular biomembranes, simpler biomimetic systems like lipid monolayers, bilayers and vesicles, are commonly used in biophysical studies of membrane properties and the interaction of membranes with soluble species.[4-6] Vesicle or liposomes are also attractive candidates for use in a variety of applications like drug delivery[7-10], cosmetic formulations[11-13], development of novel analytical or biomedical diagnostic tools[14], and for innovations in food technology because they are biocompatible and biodegradable.[15,16] The interior aqueous environment can be loaded with aqueous, polar material while the enclosing bilayer membrane can retain non-polar species.[7] The size and composition of vesicles are the most commonly varied parameters for modulating vesicle properties to control specific interactions, particle stability, cellular uptake and retention, and their sensitivity to environmental factors or triggers like pH and temperature.[7] The surface charge on lipid vesicles is an important determinant of colloidal stability as modulating electrostatic interactions can help prevent particle agglomeration.[17,18] In a biological context, surface charge on particles is often correlated with toxicity to cells, retention or removal by the reticuloendothelial system (RES), and cellular uptake/permeability.[7,19] It is therefore important to understand how membrane surface charge can be manipulated to suit a particular application.

The most common method used to characterize vesicle charge is by zeta potential measurements.[20] This light scattering-based technique uses electrophoretic mobility of particles (U_E) in an electric field to determine potential (ξ) at the hydrodynamic shear/slip plane using Henry's equation (Eq. 1).

$$U_E = \frac{2\,\varepsilon_0 \varepsilon_r\,\xi\,f(\kappa a)}{3\,\eta} \qquad \text{(Eq. 1)}$$

Henry's equation accounts for solution properties like viscosity (η), dielectric constant (ε) directly, while the like ionic strength (Debye length, κ^{-1}) and particle size (a) are indirectly accounted for using a fitting parameter *f(κa)* which is varied between 1 and 1.5 based on the value of κa.[21,22] Typically, the Hückel approximation, $f(\kappa a)$ = 1, is used for non-polar solvents and for κa < 1. The Smoluchowski approximation, $f(\kappa a)$= 1.5, is used for aqueous solutions with κa >> 1. The location of the hydrodynamic shear or slip plane (also known as the zeta plane) with respect to the particle surface (usually assumed to be between 2 – 20 Å) is often hard to define, making conclusive data interpretation difficult.[22,23] In this work vesicle zeta potential measurements are compared to direct measurements of electrostatic forces between similarly composed supported lipid bilayers using the surface force apparatus (SFA). The SFA has been used extensively to study interactions forces between lipid bilayers composed of neutral, zwitterionic lipids (PC, PE), but little work has been done on charged lipid bilayers.[24-30] Further, a direct comparison of measured potential using the two techniques has not been previously reported.

A variety of studies have been conducted on charged vesicles investigating zeta potential variation. For example, the zeta potential of DSPC:cholesterol vesicles linearly increased with the addition of up to 8 mol% anionic (DOPS) or cationic (DOTAP) lipid groups in 10 mM NaCl (pH 7.4 - 7.7).[20] Similar studies on cholesterol-containing mixed PS:PC vesicles between 6.6 to 17.6 mol%

PS also found a linear potential increase in high salt concentrations (152 mM, pH 5.9), but no potential increase with charged lipid fraction in low salt concentrations (6.6 mM, pH 5.9).[31] A systematic investigation of the effect of monovalent salt over a concentration range of 10 to 90 mM NaCl (pH 7.4) on zeta potential of charged vesicles composed of 20 or 100 mol% DOPG found greater potential values at low salt concentrations and a larger variation in potential with salt concentration when the vesicles contained 20 mol% compared to 100 mol% DOPG.[32] Similarly, the zeta potential of DOPS:DOPC vesicles in ultrapure water saturated at 10 mol% DOPS.[33] In other words, just increasing the concentration of charged lipid in the vesicle did not necessarily result in a higher potential.

In this work, the charge behavior of lipid vesicles and supported bilayers composed of two different anionic lipids DMPS and DMPG mixed with zwitterionic lipid DMPC in monovalent salt solutions was investigated. (**Figure 1**) The fraction of charged lipids (DMPS or DMPG) was varied from 0 to 100 mol% in solutions of different ionic strength and pH. In general, good agreement was found between vesicle zeta potential and direct force spectroscopy measurements using the SFA. In particular, the SFA enables direct measurements of electrostatic forces between lipid bilayers as a function of exact surface separation. This removes ambiguity associated with Henry's equation. For measurements in physiological conditions, the interplay of membrane composition, lipid headgroup pKa, solution ionic strength and pH was reasonably well captured by the Gouy-Chapman-Stern-Grahame (GCSG) model of the electrical double layer when counterion binding was taken into account. In low ionic strength solutions, the GCSG model overestimated surface potential, particularly at high surface charge loading (> 20 mol %). Instead, under low ionic strength the measured membrane potential was accurately predicted by Manning's charge condensation theory which indicates that in dilute salt solutions, there exists a critical surface

charge density beyond which counterion condensation is observed. Beyond this limit, the addition of more charged groups to the surface does not further increase the surface charge. Lastly, some rules of thumb for tuning vesicle charge through composition and solution conditions are provided.

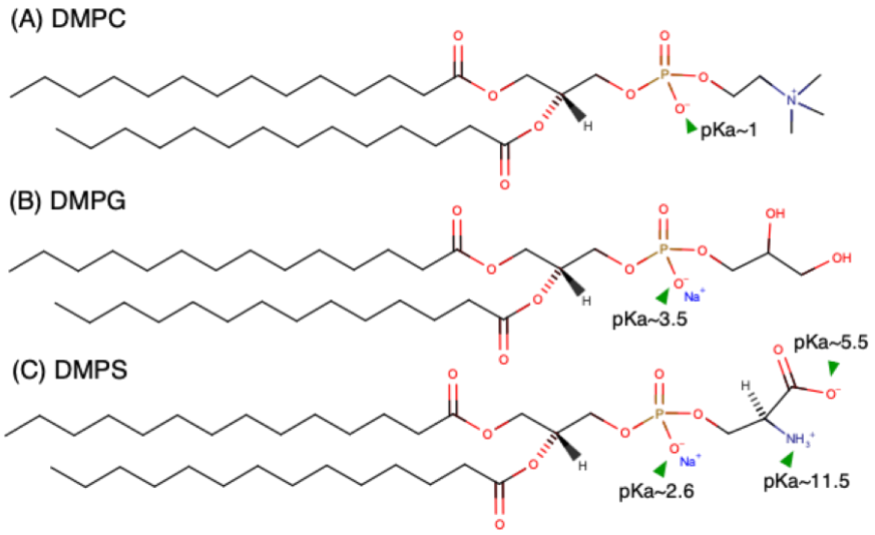

Figure 1: Structure of (A) DMPC, (B) DMPG, and (C) DMPS. Ionization constants (pKa) of different head group moieties are highlighted.[1]

4.2 Materials and Methods

4.2.1 Chemicals

1,2-dimyristoyl-*sn*-glycero-3-phospho-(1'-rac-glycerol) (sodium salt) (DMPG, T_m= 23°C), 1,2-dimyristoyl-*sn*-glycero-3-phospho-L-serine (sodium salt) (DMPS, T_m= 35°C), 1,2-dimyristoyl-*sn*-glycero-3-phosphocholine (DMPC, T_m= 24°C) and 1,2-dipalmitoyl-sn-glycero-3-phosphoethanolamine (DPPE, T_m= 63°C) were purchased in powder form (>99% purity, Avanti Polar Lipids, Inc, Alabaster, AL, USA). Lipid stock solutions of desired concentrations (<5 mg/ml) were prepared by dissolving the powders in 9:1 volume % chloroform: methanol. Sodium nitrate ($NaNO_3$, 99.995% purity, Sigma, St. Louis, MO, USA) was used to prepare monovalent electrolyte solutions used in surface force measurements and low salt zeta potential measurements. Sodium

phosphate dibasic heptahydrate ($Na_2HPO_4.7H_2O$, >99+% purity, ACROS Organics, NJ, USA), sodium phosphate monobasic monohydrate and sodium chloride ($NaH_2PO_4.H_2O$, 99.2% purity, NaCl, 99.9% purity, Fisher Scientific, Waltham, MA, USA) were used to prepare the phosphate buffer for zeta potential measurements. Water used in experiments was purified with a MilliQ Gradient water purification system with a resistivity of 18.0 MΩ·cm.

4.2.2 Vesicle preparation

Appropriate volumes of each lipid stock solution were added to an amber glass vial to obtain the desired lipid composition. A gentle stream of nitrogen gas was used to evaporate the solvent from the lipid mixture while rotating the vial to ensure the lipids coated the walls uniformly. The samples were then fully dried by placing them in a vacuum chamber for a minimum of 4 h to ensure complete removal of solvent. The dried lipid samples were rehydrated with 3 mL of 0.5 mM $NaNO_3$ (to a concentration of 0.4 mg/ml) for measurements in low salt conditions or with a 140 mM phosphate buffer (7.5 mM $Na_2HPO_4.7H_2O$, 2.5 mM $NaH_2PO_4.H_2O$, 130mM NaCl, pH 7.4) for measurements in physiological conditions. The solutions were thoroughly vortexed to dissolve the lipids, sonicated in a water bath sonicator (Cole Palmer Ultrasonic cleaner, Model 8891, 42 kHz) for 10 minutes to form vesicles, and finally, homogenized using a probe-tip sonicator (Ultrasonic Homogenizer, Model 150 V/T, Biologics, Inc.) at 30 % power for 1 minute. After probe-tip sonication, vesicle solutions were filtered using a 0.22 µm syringe filter to remove any titanium particles generated during the sonication process. For samples rehydrated with 140 mM phosphate buffer, the samples were heated to approx. 35 °C and extruded through a vesicle extruder with 100 nm polycarbonate filter 15 times to further ensure sample homogeneity. All vesicle samples were characterized for size and surface potential within 2 hours of preparation.

4.2.3 Dynamic light scattering (DLS) and Zeta potential

A Malvern Zetasizer Nano ZS90 instrument (Southborough, MA, USA) was used to perform dynamic light scattering measurements to characterize the vesicle size distribution and measure the zeta potential. Approximately 1 ml of sample was loaded into the cuvette and allowed equilibrate to 25 °C. A minimum of three size measurements (90° scattering angle) were performed per sample with more than 30 runs per measurement. Zeta potential measurements based on the electrophoretic mobility were performed on the same sample to quantify the surface potential at the hydrodynamic slip plane using the Smoluchowski approximation ($f(\kappa a)$ = 1.5). Potential values were obtained from at least 3 independently prepared samples with at least 3 separate measurements per sample (>30 runs per measurement) for each vesicle composition.

Lipid bilayer/vesicles are highly hydrated systems with water molecules and counterions strongly associated with the membrane interface.[3] In this work, the Stern or stagnant layer thickness (d_s) was assumed to be 5 Å approximately the size of a hydrated Na^+ counterion (~ 4 - 4.7 Å).[34] That is to say, the zeta-potential value at the hydrodynamic slip plane was assumed to correspond to the potential (ψ) at d_s = 5 Å. This selection is supported by x-ray photoelectron spectroscopy (XPS) studies of silica nanoparticle surfaces, which indicated that the Stern layer thickness of a single hydration shell of water was 1.4 ± 0.6 Å and between 6.2 ± 0.4 to 9.1 ± 0.9 Å for Na^+ solutions.[34,35] Similarly, x-ray reflectivity measurements of muscovite mica interface in monovalent electrolyte solutions show electron density peaks between 2 and 6 Å from the interface due to layering of hydronium (H_3O^+) and sodium (Na^+) ions in electrolyte solutions.[36]

4.2.4 Monolayer isotherms and bilayer deposition

A Teflon® Langmuir–Blodgett trough (Type 611, Nima Coventry, UK) was used to measure lipid monolayer surface pressure – area (Π–A) isotherms. The trough experiments were carried out at a

room temperature of 24.5 ± 1.0 °C on a subphase of milliQ water with a pH of 5.7 ± 0.2**. SI figure S1** shows the Π–A isotherms curves for pure DMPC, DMPG, DMPS and lipid mixtures of 10 and 20 mol% charged lipids DMPS or DMPG in DMPC (e.g. 10:90 DMPS: DMPC). The isotherms indicate that while pure DMPC at 35 mN/m is in the fluid state, pure DMPG, pure DMPS and the lipid mixtures were in the gel state. No evidence of phase separation was indicated by the collapse pressure of the mixed monolayers. (**SI figure S2**).

Lipid bilayers were deposited onto mica surfaces using the Langmuir-Blodgett (LB) deposition technique.[37,38] The inner leaflet in all cases was DPPE deposited at 45mN/m because it is known to produce a robust, defect-free, strongly physisorbed, gel-phase monolayer on mica with minimal lipid exchange with the outer leaflet.[39,40] The outer leaflet comprised of 10:90, 20:80 or 100:0 DMPS:DMPC or DMPG:DMPC was deposited at 35mN/m to mimic the surface pressure of vesicles.[41,42] Fluorescence microscopy images of the various bilayer compositions are shown in **SI figure S3**. The transfer ratio was 1.00 ± 0.05 for the DPPE inner leaflet and 0.98 ± 0.08 for the various compositions of the outer leaflet. A transfer ratio of 1 indicates that the deposited lipids maintained their packing area during deposition.[38] Once the complete bilayer was formed on mica-coated SFA discs, the surfaces were kept submerged under water and mounted in the SFA box.

4.2.5 Surface force apparatus (SFA)

The SFA technique has been used extensively to measure the interaction forces between surfaces.[43-46] In brief, the substrates supporting the LB deposited bilayers were atomically smooth mica substrates (with a 55 nm thick back coating of evaporated silver) glued onto cylindrical glass discs. The silver layer on each disk partially transmits light directed normally through the surfaces, which constructively interferes to produce fringes of equal chromatic order (FECO). The SFA uses

multiple-beam interferometry (MBI) to provide a definitive measure of surface separation (± 0.2 nm) and film thickness.[43]

One of the bilayer-coated mica surfaces was mounted on a fixed stage, and the other was mounted on a double-cantilever spring of known stiffness (~ 2.8×10^5 mN/m) which can be displaced vertically. The distance between the surfaces was measured by observing and tracking the position and displacement of FECO peak wavelengths within a spectrometer. A custom-automated SFA Mark- II was used for data collection and surface displacements via a computer-controlled motor system. A sensitive CCD camera (Princeton SPEC-10:2K Roper Scientific, Trenton, NJ) was interfaced with the spectrometer and computer acquisition system to allow automated FECO wavelength tracking. The water in the SFA box was saturated with a small volume of lipid solution (same composition as the outer leaflet) to minimize lipid desorption from the bilayer during the course of the measurements. After the surfaces were mounted, the SFA box was placed in a temperature-controlled room at 25.0 ± 0.1 °C to equilibrate for a minimum of 2h before measurements. The experiments were completed within 24 h of bilayer deposition. The separation distance was calculated by approximating the system as a symmetric 3-layer interferometer and using analytical solutions for the resulting optical interference, as is typical for lipid bilayers deposited on mica.[29,30] The membrane thickness was determined using the FECO wavelength shift from the membrane contact relative to the bare mica substrates after completing the experiment. Three independent SFA experiments were carried out for each of the membrane compositions. Force profiles shown in the results and discussion section are for one set of experimental measurements but were consistent among the three independent experiments.

4.2.6 Membrane thickness determination and D=0

At the end of each experiment, the surfaces were separated, and the apparatus solution was drained, thereby removing the outer leaflets of the bilayers. The SFA box was connected to a vacuum source for a minimum of 2 h to dry the box completely. The hydrophobic inner DPPE layers were brought into contact to determine the thickness change attributable to the two outer leaflets which includes their hydration. Theoretical thicknesses for anhydrous bilayers (without headgroup hydration) were obtained from previous x-ray scattering studies (D_{HH} (Å)) performed on gel phase lipid bilayers.[47-50] Area per molecule values obtained from lipid monolayer pressure-area isotherms (SI figure S1) were in good agreement with values reported from x-ray scattering experiments on DMPC (48.1 $Å^2$) and DMPS (40.8 $Å^2$) in the gel phase. No X-ray scattering bilayer measurements of DMPG in the gel phase were found. As DMPG has a similar transition temperature (T_m) as DMPC, similar area per molecule and D_{HH} (Å) in the fluid phase, the thickness of gel-phase DMPC was used for gel-phase DMPG.[49,50] Zwitterionic lipid bilayers are known to have a 6 - 10 Å thick hydration layer associated with the headgroups (per bilayer).[3,50,51] Based on the measured hydrated bilayer thicknesses form SFA and the anhydrous thicknesses based on the lipid molecular structure, we found that bilayers containing DMPS and DMPG had an average hydration thickness of 9 ± 2 Å and 15 ± 2 Å per bilayer respectively. This difference can be attributed to the fact that the glycerol head group on DMPG has a higher tendency to form hydrogen bonds with neighboring water molecules. The SFA measurements are consistent with inter-bilayer water spacing obtained from osmotic pressure measurements performed on DMPG bilayers.[52] The values for bilayer thickness (from x-ray scattering) and hydrated thickness (from SFA measurements) are summarized in **Table 1**.

Table 1. Anhydrous bilayer thickness (D_{HH} Å) from x-ray scattering experiments.[47,48] Hydrated bilayer thickness from surface force measurements averaged over all compositions, 10:90, 20:80, 100:0 DMPG:DMPC or DMPS:DMPC.

Bilayer composition	Anhydrous bilayer thickness (Å)	Hydrated thickness (Å)
DMPG	40.1	69.9 ± 4.6
DMPS	44.3	62.4 ± 1.6

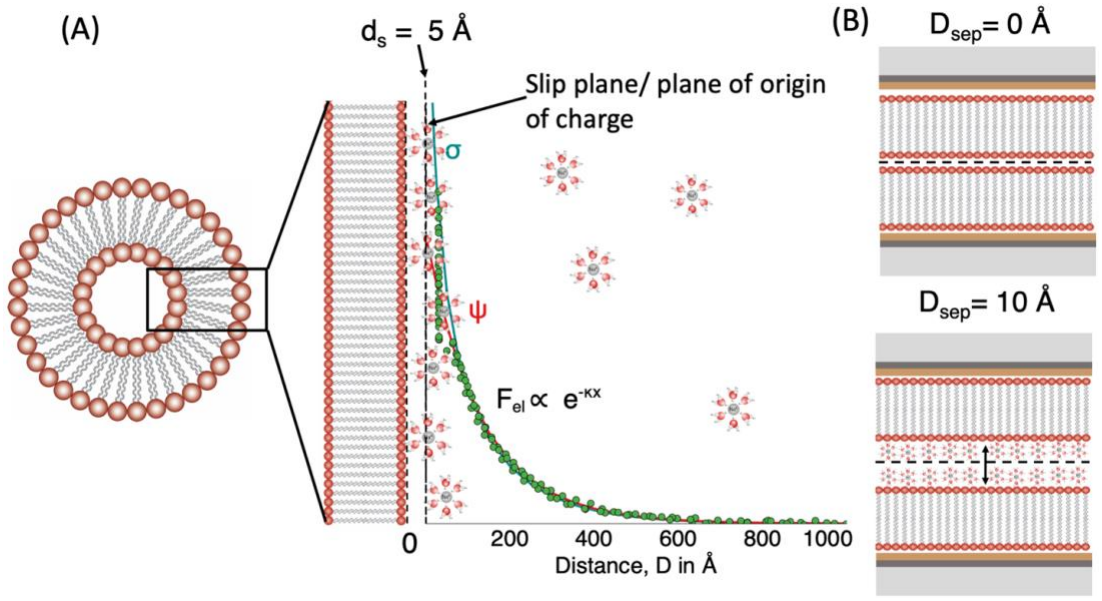

Figure 2: A schematic of the equivalent frame of references used to interpret (A) Zeta potential measurements and (B) SFA measurements.

In this work, D = 0 was defined as the anhydrous contact of the lipid bilayers. The "charge" plane of origin (outer Helmholtz plane, OHP), was assumed to be located 5 Å from each bilayer surface (surface separation distance, D = 10 Å). This plane is equivalent to the assumed hydrodynamic shear or slip plane for the vesicle zeta potential measurements which corresponds to a Stern layer thickness of one hydrated Na^+ counterion diameter (ξ = potential at d_s = 5 Å). A schematic of this frame of reference is shown in **figure 2**. In **SI section S5**, an analysis of surface

charge and potential obtained from assumptions of different charge planes of origin (D = 0, 10, 20 Å for opposing bilayers which is equivalent to d_s = 0, 5, 10 Å respectively for a vesicle) is provided for two different bilayer compositions - 10:90 DMPG:DMPC and 100:0 DMPG:DMPC.

4.2.7 Electrostatic forces (SFA)

At large separation distances, (D > 100 Å), electrostatic repulsion was the only contributor to the measured force between the bilayers. An exponential curve was fit to the data between 100 to 600 Å to determine the Debye length and effective salt concentration of the system. The surface charge density and potential of the lipid bilayers were then calculated using a numerical iterative solution to the nonlinear Poisson Boltzmann equation (NLPB, Eq. 2) using constant charge and constant potential boundary conditions to fit the experimentally measured electrostatic force.

$$\frac{d^2Y}{d\,x^2} = \sinh Y \qquad \text{(Eq. 2)}$$

where $Y = \frac{ze\psi}{kT}$ and and $x = \frac{D}{\kappa^{-1}}$, z the valency of the ion, e is electronic charge, ψ the electrical double-layer potential, k the Boltzmann constant, T is temperature, κ^{-1} is the Debye length and D is the separation distance between the surfaces. The Derjaguin approximation (Eq. 3) was used to convert the NLPB solution which gives double layer electrostatic interaction energy (E) between flat plates to the force (F) between crossed cylinders as used in the SFA normalized by the geometric mean radius of curvature ($R = \sqrt{R_1 R_2}$).

$$E(D) = \frac{F(D)}{2\pi R} \qquad \text{(Eq. 3)}$$

4.2.7.1 Gouy-Chapman-Stern-Grahame (GCSG) model

Following the work of Ohki, S., et. al.[53] and others[54-56], the GCSG model of the electrical double layer was used to predict the surface charge/potential at the charged bilayer surface. The Gouy Chapman (Eq. 4) solution to the NLPB equation gives the diffuse double layer electrostatic potential distribution from a planar surface of uniform surface charge in a symmetric (z:z) electrolyte.

$$\tanh\left(\frac{ze\psi_d}{4kT}\right) = \tanh\left(\frac{ze\psi_0}{4kT}\right)\exp(-\kappa d) \qquad \text{(Eq. 4)}$$

where ψ_0, ψ_d are the electrical double-layer potentials at the surface and at a distance d from the surface. For $\kappa a \gg 1$, the interacting spherical vesicles can be approximated as flat planes. The use of spherical Gouy Chapman solution resulted in a difference in potential value of less than 5 percent. The Grahame equation (Eq. 5), derived from the Guoy Chapman solution, gives the relationship between the surface charge density and potential at the interface.

$$\sigma_0 = (8\varepsilon_r\varepsilon_0 N_A kT([Na^+]_\infty + [H^+]_\infty))^{\frac{1}{2}} \sinh\left(\frac{e\psi_0}{2kT}\right) \qquad \text{(Eq. 5)}$$

where σ_0 is the surface charge density, N_A is Avogadro's number, and $[Na^+]_\infty$ and $[H^+]_\infty$ are the bulk concentration of the counterions. Bilayer charge originates from the dissociation of PS or PG head groups and can be calculated using $\sigma_{max} = \pm \frac{e\,\chi_j}{A_j}$ where χ_j is the mol fraction of charged lipids, and A_j is the area per lipid. Accounting for counterion binding to the head groups at the interface using the Langmuir adsorption model reduces the surface charge to an effective value $\sigma_{0,eff}$:

$$\sigma_{0,eff} = \frac{\sigma_{max}}{1 + \left(\frac{[H^+]_\infty}{K_a} + K_c[Na^+]_\infty\right)\exp(-\frac{e\psi_0}{kT})} \qquad \text{(Eq. 6)}$$

K_c is the binding constant for Na^+ counterions and K_a is the dissociation constant for H^+ ions calculated from the acid dissociation constant for the lipid (pKa). An average area per lipid value of 45 $Å^2$/molecule (corresponding to a surface pressure of 30 - 35 mN/m) was used for these calculations based on isotherms for different bilayers compositions as shown in SI figure S1.

4.2.7.2 Charge Condensation Model

Manning's charge condensation theory is often used in the context of linear polyelectrolytes in dilute electrolyte solutions to explain saturation in surface charge density beyond a maximum value (σ_{crit}). [57] The condensation refers to the collapse of counterions from the diffuse ion atmosphere onto the charged surface to minimize free energy, thereby keeping the system $\leq \sigma_{crit}$. For large spheres in dilute solutions following the criteria $\kappa a \sim O(1)$, counterion condensation occurs above a critical value of surface charge density σ_{crit} given by Eq. (7):

$$\sigma_{crit} = \frac{e\,(1 - \kappa a)\ln(\kappa l_B)}{2\pi z l_B a} \qquad Eq.\,(7)$$

where l_B is Bjerrum length (~ 7.01 Å for water at 298K). For a thick cylinder geometry with $\kappa a \gg 1$, where a is the radius of the cylinder (a ~ 1 cm for SFA discs), the σ_{crit} is the same as that for a large plane given by Eq. (8):

$$\sigma_{crit} = \frac{e\kappa \ln(\kappa l_B)}{2\pi z l_B} \qquad Eq.\,(8)$$

Both the GCSG and charge condensation models have been used to explain measured vesicle zeta potential under different solution conditions.

4.3 Results and Discussion

4.3.1 Dynamic light scattering (DLS) size measurements

The average size of vesicles produced by extrusion in 140 mM phosphate buffer (pH 7.4 ± 0.1) was 156 ± 39 nm and for vesicles produced by probe tip sonication in 0.5 mM $NaNO_3$ (pH 5.7 ± 0.1) was 141 ± 65 nm. The average size of vesicles varied between 127 – 193 nm in 140 mM salt solution and 97 – 182 nm in 0.5 mM salt solution but no clear trends in size with varying membrane composition were observed, summarized in **SI Table S1**. 100 mol% DMPS or DMPG samples were observed to be more prone to aggregation over time and care was taken to carry out size and potential measurement soon after preparation. For some vesicle compositions, up to 10 % of the lipid assemblies were ~20-30 nm in size but the measured zeta potential result was unaffected.

4.3.2 Zeta potential measurements

Figure 3 shows the dependence of zeta potential on the mol% of charged lipid in mixed DMPS:DMPC and DMPG:DMPC vesicles prepared in physiological and in low salt conditions. The error bars indicate one standard deviation. As expected, the zeta potential was negative for vesicles composed of negatively charged lipids. Both DMPG and DMPS, can bear one negative charge per lipid head group for solution pH < 9 -10. In physiological salt condition, a monotonic increase in zeta potential was observed with fraction of charged lipid up to 20 - 30 mol% above which the surface potential saturated at -34 ± 3 mV for 100 mol% DMPS and -32 ± 3 mV for 100 mol% DMPG. In the low salt condition, a more rapid increase in zeta potential was observed but only up to ~ 5-10 mol% charged lipids. Above this concentration the zeta potential saturated at -68 ± 3 mV for 100 mol% DMPS and -69 ± 3 mV for 100 mol% DMPG. **Table 2** gives the fraction of charged lipids dissociated ($\alpha = \sigma_{0,eff}/\sigma_{max}$) and the effective fraction of total lipids dissociated in the membrane for the different membrane compositions. (calculated using the Eq. 4 and 5 assuming zeta potential value corresponded to $\psi_{d=5\,\text{Å}}$). The similarity in surface potential between DMPS and DMPG is somewhat surprising at the low salt condition. Here, the solution

pH is 5.7 ± 0.2 but the difference in pKa of the lipids (3.5 vs. 5.5 does not result in a discernable difference in ionization behavior. The importance of pH, ionic strength and lipid pKa will be further discussed after comparison to direct force measurements of bilayer charge/potential.

Table 2: Zeta potential measurements. Fraction of charged lipids dissociated was calculated by comparison of surface charge with theoretical maximum surface charge for each composition (based on mole fraction of charged species and area per lipid of 45 $Å^2$/molecule). Given the similarity in potential trends for DMPS and DMPG, only dissociation data for DMPS:DMPC mixtures is reported.

140 mM phosphate buffer, pH 7.4				
DMPS: DMPC	Zeta potential ζ, mV	Surface charge σ_0, mC/m^2	Fraction of charged lipids dissociated (Approx.%)	Overall lipids dissociated (%)
1:99	-2 ± 1	-3 ± 3	91	1
5:95	-9 ± 1	-15 ± 2	82	4
10:90	-13 ± 2	-22 ± 3	63	6
20:80	-25 ± 4	-49 ± 10	69	14
30:70	-31 ± 3	-68 ± 11	64	19
100:0	-34 ± 3	-79 ± 15	22	22 ± 4
0.5 mM $NaNO_3$, pH 5.7				
DMPS: DMPC	Zeta potential ζ, mV	Surface charge σ_0, mC/m^2	Fraction of charged lipids dissociated (Approx. %)	Overall lipids Dissociated (%)
0.5: 99.5	-28 ± 2	-1.6 ± 0.1	88	0.4
1:99	-36 ± 3	-2.1 ± 0.2	60	0.6
5:95	-55 ± 5	-3.7 ± 0.4	21	1.0
10:90	-65 ± 3	-4.6 ± 0.2	13	1.3
20:80	-76 ± 2	-6.0 ± 0.3	8	1.7
100:0	-68 ± 3	-5.0 ± 0.4	1.4	1.4 ± 0.2

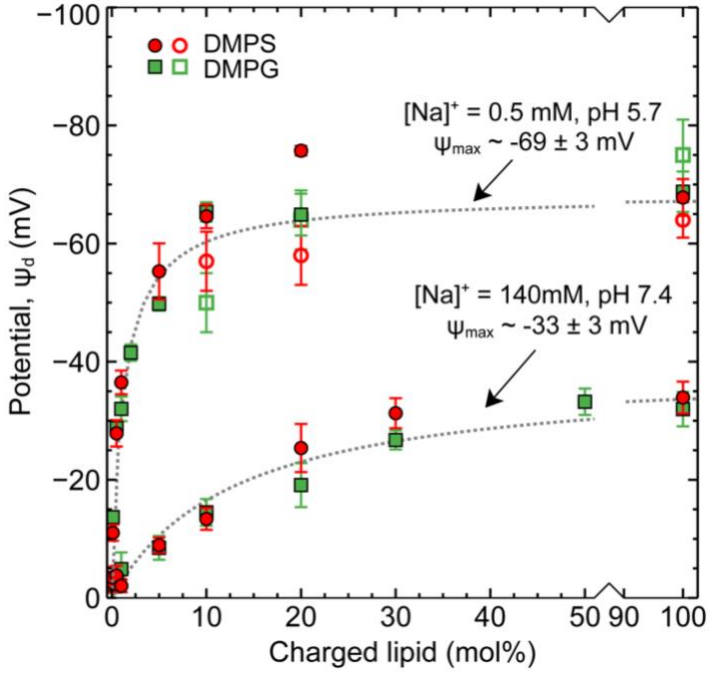

Figure 3: Zeta potential measurements of mixed DMPS:DMPC and DMPG:DMPC vesicles in physiological (140 mM, pH 7.4) and low salt (0.5 mM, pH 5.7) conditions (solid markers). SFA measurements of mixed DMPS:DMPC and DMPG:DMPC lipid bilayers in low salt conditions 0.5 mM, pH 5.7 (hollow markers). Dotted lines are guides to the eye.

4.3.3 Surface force measurements

Surface force measurements were performed in low salt conditions of 0.5 mM $NaNO_3$. At high salt concentrations it is difficult to separate electrostatic for short Debye lengths (~8 Å) from hydration repulsion forces. **Figure 4** shows an exemplar force profile for a pure, 100% DMPG supported bilayer in 0.5 mM $NaNO_3$, pH 5.7 ± 0.2. Similar plots for other membrane compositions are provided in SI figure S4**.** The data is presented on a semi-logarithmic plot to clearly demonstrate the electrostatic force which decays exponentially according to the Debye length. The experimentally measured Debye length across all experiments was consistent with the solution electrolyte concentration, 137 ± 10 Å. At small surface separations (~ 20 – 30 Å compared to the anhydrous bilayer contact D = 0) a strong repulsive force was measured corresponding to physical

contact of opposing, hydrated lipid bilayers. Numerical solutions to the non-linear Poisson Boltzmann equation were used to fit the electrostatic repulsion and determine the surface potential and charge of the membrane. These values are tabulated in **Table 3**. **Figure 3** (open symbols) shows the potential values obtained from surface force measurements for 10:90, 20:80, 100:0 DMPG:DMPC or DMPS:DMPC in 0.5 mM $NaNO_3$ compared to vesicle zeta potential measurements (closed symbols).

Table 3. Surface charge and potential from surface force measurements. Fraction of charged lipids dissociated was calculated as described in Table 2.

Outer leaflet composition (mol%)	σ (mC/m^2)	ψ (mV)	Area per charge (nm^2 per e^-)	Fraction of charged lipids dissociated (Approx.%)	Overall lipids dissociated (%)
10:90 DMPG:DMPC	-2.9 ± 0.6	-50 ± 5	55 ± 10	8	0.8
20:80 DMPG:DMPC	-4.0 ± 0.5	-64 ± 5	40 ± 5	6	1.2
100:0 DMPG:DMPC	-5.3 ± 0.6	-75 ± 6	30 ± 3	1.5	1.5 ± 0.2
10:90 DMPS:DMPC	-3.4 ± 0.6	-57 ± 5	47 ± 7	10	1
20:80 DMPS:DMPC	-3.5 ± 0.5	-58 ± 5	46 ± 6	5	1
100:0 DMPS:DMPC	-4.0 ± 0.3	-64 ± 3	40 ± 3	1.1	1.1 ± 0.1

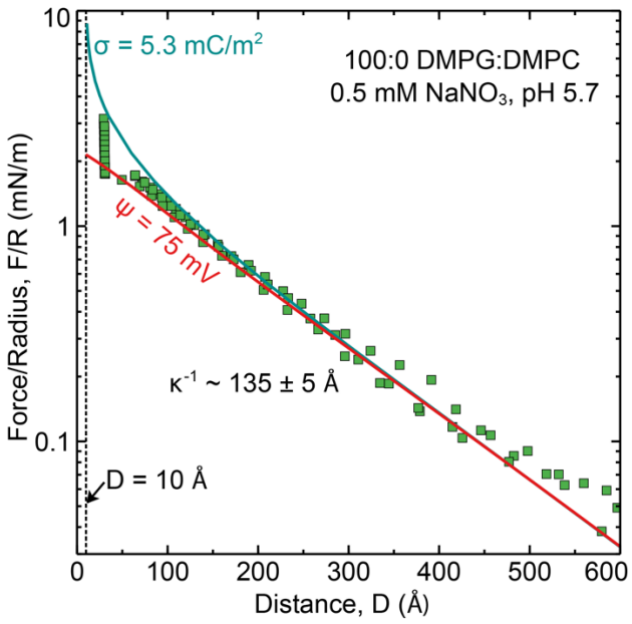

Figure 4: Measured interaction force profile between lipid bilayers composed of 100 mol% DMPG (outer leaflet) deposited on DPPE (inner leaflet) in 0.5mM $NaNO_3$, pH 5. D = 0 was set to be the anhydrous bilayer contact which corresponds to the location of the phosphate head group plane. D = 10 corresponds to a contact of the OHP planes. This is equivalent to d_s = 5 Å from the opposing membranes 2 d_s = 10 Å).

The experimentally determined potentials were consistent between the two techniques and show similar charge saturation behavior. While there were slight differences (typically < 10 mV) observed between potential values obtained for DMPS and DMPG by SFA and vesicle zeta potential measurements, there were no particular trends that could be attributed to differences in ionization constants (pKa) between the two lipids, which suggests that both DMPS and DMPG have a similar ionization behavior in a bilayer. Although one might expect that the electrostatic repulsion would scale with the fraction of charged lipids, this was far from what was observed. In both measurement conditions, two different regimes were observed – a linear regime wherein the potential increased with added charged lipid followed by a constant potential regime where the potential remained independent of the amount of charged lipid in the membrane. These results are in agreement with previous studies by Smith et. al.[20], which investigated zeta potential as a function

of 0 to 8 mol% charged anionic lipid DOPS and cationic lipid DOTAP mixed with DSPC and cholesterol in 10 mM NaCl (pH 7.4 – 7.7). Over this small concentration range a linear dependence between potential and mol% charged lipid was found. Crommelin [31] also observed a near linear dependence (up to -40 mV) with cholesterol-containing mixed PS:PC multilamellar vesicles (6.6, 12.5, and17.6 mol% PS) in 152 mM salt solution. A saturation at 6.6 mol% (potential ~ -60 mV) was found in 6.6 mM salt (pH 5.9). The vesicle composition at which a linear dependence of potential on the fraction of charged lipid changes to a saturation in potential clearly depends on the ionic strength and pH of the experiments. Together, these studies demonstrate that there is a maximum membrane charge/potential attainable for a given solution condition. As shown in Table 2 and 3, in the case of high ionic strength we observe a maximum dissociation fraction of 15-20 % of total lipids on the surface and in low ionic strength solutions a far lower amount 1-2 %. As the fraction of charged lipid in the membrane is increased, intra-membrane repulsion between neighboring "charged" lipid head groups is a significant factor and affects lipid head-group dissociation. In solutions of high ionic strength, the electrostatic repulsion forces decay over a short distance ($1/\kappa$ ~0.8 nm) allowing for higher fractions of added lipids to be dissociated compared to low ionic strength solutions $1/\kappa$ ~ 13.6 nm).

To better understand the interplay of solution conditions and lipid pKa, we first compared our results to predictions of the GCSG model of the electrical double layer. Based on previous studies, a value of 0.6 M^{-1} was chosen for the binding constant K_c between Na^+ and DMPG or DMPS head groups.[53,54] ${K_a}^{-1}$, the binding constant for H^+ with the charged lipid species, was calculated from the pKa of the relevant dissociable group (COO- for DMPS and PO_4^- for DMPG). While the intrinsic pKa value for a given dissociable group is constant, the apparent pKa value depends on local environment including dielectric, ionic strength, local charge and electrostatics

making it hard to determine. The pKa of primary phosphate groups is thought to be ~ 0 - 2, secondary phosphates ~ 6 - 7, carboxyl groups ~ 3 – 5, and primary amines ~ 9 - 11.[1] A lower degree of ionization is expected for charged lipid head groups containing these dissociable moieties, especially when present in a lipid monolayer/bilayer, due to the lower dielectric constant ($\varepsilon \sim 4$) of the acyl chains that make up the hydrophobic core of a lipid bilayer.[58] Estimates of 3.5 and 5.5 pKa were used for DMPG and DMPS respectively based on titrations of gel to fluid bilayer phase transition temperature.[1] The magnitudes of $\frac{[H^+]_0}{K_a}$ and $K_c[Na^+]_0$ in Eq. 6 determine whether and which ion binding effects are significant. Since the interfacial concentration of counterions increases exponentially with surface potential, at higher surface charges, ion binding effects become more prominent. To separate the effects of pH and ionic strength, additional complementary experiments were done on 10:90 and 100:0 DMPS:DMPC vesicles in 0.5 mM, pH 7.4 and 140 mM, pH 5.7. The measured vesicle potentials are included in **Figure 5** which also shows theoretical predictions of potential at the OHP (ψ_{5A}). In the physiological salt solution (low H^+ and high Na^+), Na^+ ion binding is the dominant effect and the GCSG model with a pKa ~ 3.5 explains the measured trends of vesicle zeta potential reasonably well for both measured solution pH conditions 5.7 and 7.4. Film expansion studies and titration experiments on PG lipid monolayers at the air-water interface have also shown a strong dependence of pKa on ionic strength, lipid acyl chain length and area per lipid, with higher apparent pKa values in low salt concentration, for longer acyl chain length and smaller area per lipid.[59] In the low ionic strength solution with solution pH 5.7, an assumption of pKa ~ 3.5 (DMPG) accurately predicts potential up to 2 mol % but significantly overpredicts the potential at high concentration of charged lipid. pKa ~ 5.5 (DMPS) under predicts the potential at low charged lipid concentrations (< 5%) but reasonably fits compositions between 5 - 20 mol %. At 100 mol% DMPS, the deviation between

GCSG predictions and theory is quite significant (> 30 mV). Furthermore, the measured potential is the same at pH 5.7 and 7.4 despite theory predicting otherwise. In order to fit the measured potentials at 100 % charged lipid in pH 5.7 and the potentials obtained in pH 7.4 an unphysical pKa value ~ 7 - 8 would be required for both DMPS and DMPG. In summary counterion binding within the GCSG framework is able to predict the charge behavior at high ionic strength but not in low ionic strength.

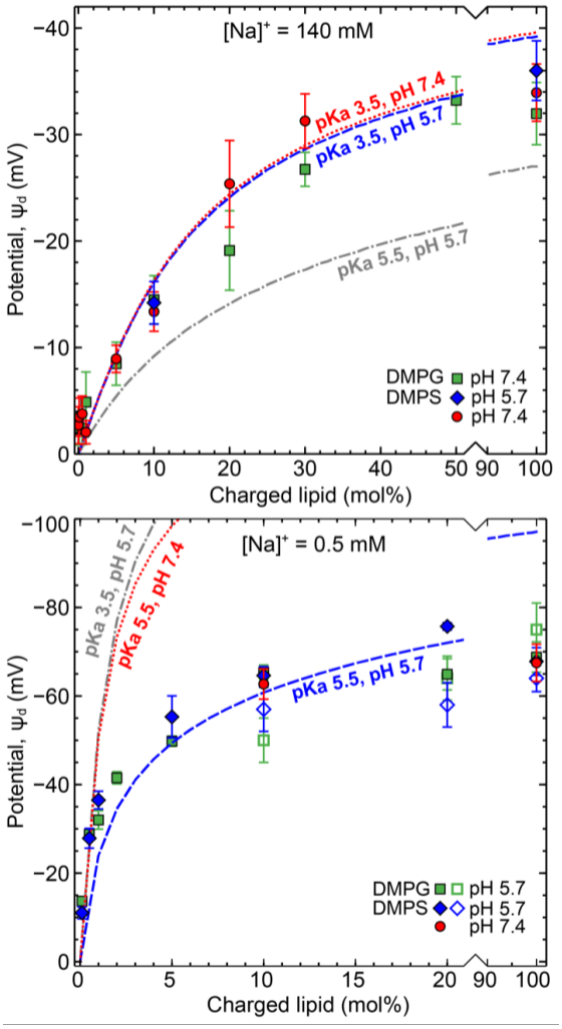

Figure 5: A comparison of predicted potential at the OHP/zeta slip plane (d_s =5 Å or D = 10 Å) from Gouy-Chapman-Stern-Grahame theory after accounting for counterion binding effects with experimental zeta potential results in (A) 140 mM salt and (B) 0.5 mM salt.

At low ionic strength, a charge condensation model is required. Charge condensation phenomenon is often observed with highly charged polyelectrolytes in dilute salt solutions wherein beyond a critical surface charge density, counterions collapse on the charged species to minimize the free energy of the system.[57] For vesicles with an average radius $a \sim 80 \pm 20$ nm the σ_{crit} value for 0.5 mM salt solution is -5.35 < σ_{crit} < -5.99 mC/m^2 and for lipid bilayers deposited on cylindrical SFA discs (a ~1 cm), the σ_{crit} is ~ 6.94 mC/m^2. The experimentally measured maximum surface charge for vesicles and bilayers was around 5 ± 1 mC/m^2 which is in good agreement with charge condensation theory. A similar charge condensation behavior and saturation to a potential of -44 mV (~ 2 mC/m^2) was observed by Lütgebaucks. et. al.[33], in their experiements on 0-100 mol% DOPS:DOPC vesicles in ultrapure water. In complementary sum-frequency generation (SFG) spectroscopy studies[60] of water alignment near mixed anionic and cationic lipid monolayers in 10 mM NaCl, Dreier et. al.[60] detected a linear increase in water alignment with increase in membrane charge at low surface charge densities. Beyond 20 % excess anionic lipid, a saturation in water alignment was observed attributable to charge condensation as also found in our studies.

Eisenberg et. al.[61] investigated the zeta potential of large (1-20 μm), single component multilamellar anionic vesicles composed of pure – PS, PG, PI and PA in monovalent high salt solutions (100 mM, pH 7.5). They also found similar potential values for PS and PG vesicles. The zeta potential for PA vesicles was ~ 10 mV higher and for PI was 15 - 20 mV lower. In comparison to this work, the higher value zeta potential for PA vesicles could be explained by additional dissociation of the phosphate group (pKa$_2$ ~ 8). The lower potentials for PI vesicles are likely due to the bulky, hydrated sugar head group shielding charges more effectively or increasing the stern layer thickness. This reiterates the importance of knowing the lipid head group structure, its correlation with ionization properties and plane of potential measurement. Similarly, different

counterions have different binding affinities to lipid head groups (e.g. for 1:4 DOPG:DOPC vesicles, $Li^+ > Na^+ > K^+ > Rb^+ > Cs^+$)[32], as well as different hydrated ion sizes emphasizing the importance of specific ion effects.[32,61]

Finally, biological membranes are soft, fluid interfaces which can often regulate surface charges by reorganization or counterion penetration and binding to minimize the system free energy. Clearly, there is a strong interplay between membrane composition (lipid type and concentration), phase behavior (represented by area per lipid), electrolyte type, concentration, and solution pH. While values of intrinsic and apparent lipid ionization constants are intended to capture this complex interplay, they are often measured experimentally and therefore dependent on the measurement conditions. This makes it difficult to predict a priori exact surface potential values for a given experimental system. The GCSG model is a good starting point to predict how the interplay of membrane composition and solution conditions can be tailored to obtain a desired surface potential. In general, higher potential values are obtained by decreasing electrolyte concentration though charge condensation limits the surface charge in dilute solutions. A pH-driven response is expected around the apparent pKa of the lipid ($|pH - pKa_{app}| < 1$). Therefore, to maximize surface dissociation, the pH of the electrolyte solution should be at least 2 units greater than the apparent pKa. Increasing the fraction of charged lipid results in an increase in potential but saturates at high charge loadings. Overall, this understanding can be used to guide the choice and concentration of charged lipids, especially for the development of stimulus-responsive systems that have properties dependent on pH, temperature or environmental salt concentrations.

4.4 Conclusion

Zeta potential measurements of lipid vesicle surface charge/potential in monovalent salt solutions were in good agreement with direct measurements of supported bilayer surface charge/potential

using the surface force apparatus. Given the ubiquitous use of the zeta potential technique, these results are significant as they demonstrate that the zeta potential results provide an accurate measure of lipid membrane charge behavior. The charge/potential of the lipid membrane can be controlled by increasing the concentration of charged lipid. However, depending on the ionic strength charge saturation occurs between 5-30 mol%. Intra-membrane repulsion between neighboring lipid head groups at high charge loading results in a decrease in head group dissociation. In terms of theoretical predictions, the membrane potential values obtained in physiological conditions (140 mM, pH 5.7 - 7.4) could be well fit by the Gouy-Chapman-Stern-Grahame model of the electrical double layer with Langmuir counterion binding. In low ionic strength solutions (0.5 mM, pH 5.7 - 7.4), the model overpredicted surface charge/potential. Instead, at low ionic strength Manning's charge condensation theory was much more accurate. The theoretical frameworks used in the work can be used to understand how different factors like lipid head group pKa, pH, ionic strength of the solution and counterion binding constants interplay to yield a specific potential value for the system. Though it is important to note that dissociation constants for lipids (apparent pKa) depend on lipid structure and measurement conditions. Values in literature should therefore only be used as starting point guides while designing responsive systems.

4.5 Acknowledgements and Funding Information

This work was supported by the National Science Foundation Chemistry Division through grant CHE-1413745 and by the National Institute of Health through grant 1R01GM117342-01.

4.6 References

1 Marsh, D. CRC handbook of lipid bilayers. (1990).

2 Singer, S. J. & Nicolson, G. L. The fluid mosaic model of the structure of cell membranes. *Science* **175**, 720-731 (1972).
3 Nagle, J. F. & Tristram-Nagle, S. Lipid bilayer structure. *Current opinion in structural biology* **10**, 474-480 (2000).
4 Bangham, A. D., Hill, M. W. & Miller, N. in *Methods in membrane biology* 1-68 (Springer, 1974).
5 Simons, K. & Vaz, W. L. C. Model Systems, Lipid Rafts, and Cell Membranes. *Annual Review of Biophysics and Biomolecular Structure* **33**, 269-295, doi:10.1146/annurev.biophys.32.110601.141803 (2004).
6 Peetla, C., Stine, A. & Labhasetwar, V. Biophysical interactions with model lipid membranes: applications in drug discovery and drug delivery. *Molecular pharmaceutics* **6**, 1264-1276 (2009).
7 Bozzuto, G. & Molinari, A. Liposomes as nanomedical devices. *International journal of nanomedicine* **10**, 975 (2015).
8 Jesorka, A. & Orwar, O. Liposomes: Technologies and Analytical Applications. *Annual Review of Analytical Chemistry* **1**, 801-832, doi:10.1146/annurev.anchem.1.031207.112747 (2008).
9 Pattni, B. S., Chupin, V. V. & Torchilin, V. P. New developments in liposomal drug delivery. *Chemical reviews* **115**, 10938-10966 (2015).
10 Sercombe, L. *et al.* Advances and challenges of liposome assisted drug delivery. *Frontiers in pharmacology* **6**, 286 (2015).
11 Betz, G., Aeppli, A., Menshutina, N. & Leuenberger, H. In vivo comparison of various liposome formulations for cosmetic application. *International journal of pharmaceutics* **296**, 44-54 (2005).
12 E. Ramón, E. R. *et al.* Liposomes as alternative vehicles for sun filter formulations. *Drug Delivery* **12**, 83-88 (2005).
13 Mu, L. & Sprando, R. L. Application of nanotechnology in cosmetics. *Pharmaceutical research* **27**, 1746-1749 (2010).
14 Phillips, W. T., Goins, B. A. & Bao, A. Radioactive liposomes. *Wiley Interdisciplinary Reviews: Nanomedicine and Nanobiotechnology* **1**, 69-83 (2009).
15 Mozafari, M. R. *et al.* Encapsulation of food ingredients using nanoliposome technology. *International Journal of Food Properties* **11**, 833-844 (2008).
16 Khanniri, E. *et al.* Application of liposomes in some dairy products. *Critical reviews in food science and nutrition* **56**, 484-493 (2016).
17 Du Plessis, J., Ramachandran, C., Weiner, N. & Müller, D. The influence of lipid composition and lamellarity of liposomes on the physical stability of liposomes upon storage. *International journal of pharmaceutics* **127**, 273-278 (1996).
18 Fröhlich, E. The role of surface charge in cellular uptake and cytotoxicity of medical nanoparticles. *International journal of nanomedicine* **7**, 5577 (2012).
19 Miller, C. R., Bondurant, B., McLean, S. D., McGovern, K. A. & O'Brien, D. F. Liposome− cell interactions in vitro: effect of liposome surface charge on the binding and endocytosis of conventional and sterically stabilized liposomes. *Biochemistry* **37**, 12875-12883 (1998).
20 Smith, M. C., Crist, R. M., Clogston, J. D. & McNeil, S. E. Zeta potential: a case study of cationic, anionic, and neutral liposomes. *Analytical and bioanalytical chemistry* **409**, 5779-5787 (2017).

21 Clogston, J. D. & Patri, A. K. in *Characterization of nanoparticles intended for drug delivery* 63-70 (Springer, 2011).
22 Lowry, G. V. *et al.* Guidance to improve the scientific value of zeta-potential measurements in nanoEHS. *Environmental Science: Nano* **3**, 953-965 (2016).
23 Lyklema, J. Molecular interpretation of electrokinetic potentials. *Current Opinion in Colloid & Interface Science* **15**, 125-130 (2010).
24 Marra, J. & Israelachvili, J. Direct measurements of forces between phosphatidylcholine and phosphatidylethanolamine bilayers in aqueous electrolyte solutions. *Biochemistry* **24**, 4608-4618 (1985).
25 Marra, J. Direct measurement of the interaction between phosphatidylglycerol bilayers in aqueous electrolyte solutions. *Biophysical journal* **50**, 815-825 (1986).
26 Leckband, D. E., Helm, C. & Israelachvili, J. Role of calcium in the adhesion and fusion of bilayers. *Biochemistry* **32**, 1127-1140 (1993).
27 Kuhl, T. *et al.* Direct measurement of polyethylene glycol induced depletion attraction between lipid bilayers. *Langmuir* **12**, 3003-3014 (1996).
28 Nichols-Smith, S. & Kuhl, T. Electrostatic interactions between model mitochondrial membranes. *Colloids and Surfaces B: Biointerfaces* **41**, 121-127 (2005).
29 Orozco-Alcaraz, R. & Kuhl, T. L. Interaction forces between DPPC bilayers on glass. *Langmuir* **29**, 337-343 (2012).
30 Kurniawan, J., Yin, N.-N., Liu, G.-y. & Kuhl, T. L. Interaction forces between ternary lipid bilayers containing cholesterol. *Langmuir* **30**, 4997-5004 (2014).
31 Crommelin, D. J. Influence of lipid composition and ionic strength on the physical stability of liposomes. *Journal of pharmaceutical sciences* **73**, 1559-1563 (1984).
32 Maity, P., Saha, B., Kumar, G. S. & Karmakar, S. Binding of monovalent alkali metal ions with negatively charged phospholipid membranes. *Biochimica et Biophysica Acta (BBA)-Biomembranes* **1858**, 706-714 (2016).
33 Lütgebaucks, C., Macias-Romero, C. & Roke, S. Characterization of the interface of binary mixed DOPC: DOPS liposomes in water: The impact of charge condensation. *The Journal of chemical physics* **146**, 044701 (2017).
34 Brown, M. A., Goel, A. & Abbas, Z. Effect of electrolyte concentration on the stern layer thickness at a charged interface. *Angewandte Chemie International Edition* **55**, 3790-3794 (2016).
35 Brown, M. A. *et al.* Determination of surface potential and electrical double-layer structure at the aqueous electrolyte-nanoparticle interface. *Physical Review X* **6**, 011007 (2016).
36 Lee, S. S., Fenter, P., Nagy, K. L. & Sturchio, N. C. Monovalent ion adsorption at the muscovite (001)–solution interface: Relationships among ion coverage and speciation, interfacial water structure, and substrate relaxation. *Langmuir* **28**, 8637-8650 (2012).
37 Blodgett, K. B. Films built by depositing successive monomolecular layers on a solid surface. *Journal of the American Chemical Society* **57**, 1007-1022 (1935).
38 Kurniawan, J., Ventrici de Souza, J. o. F., Dang, A. T., Liu, G.-y. & Kuhl, T. L. Preparation and Characterization of Solid-Supported Lipid Bilayers Formed by Langmuir–Blodgett Deposition: A Tutorial. *Langmuir* **34**, 15622-15639 (2018).
39 Kienle, D. F., De Souza, J. V., Watkins, E. B. & Kuhl, T. L. Thickness and refractive index of DPPC and DPPE monolayers by multiple-beam interferometry. *Analytical and bioanalytical chemistry* **406**, 4725-4733 (2014).

40 Stidder, B., Fragneto, G. & Roser, S. J. Structure and stability of DPPE planar bilayers. *Soft Matter* **3**, 214-222 (2007).
41 Marsh, D. Lateral pressure in membranes. *Biochimica et Biophysica Acta (BBA)-Reviews on Biomembranes* **1286**, 183-223 (1996).
42 Demel, R., Van Kessel, W. G., Zwaal, R., Roelofsen, B. & Van Deenen, L. Relation between various phospholipase actions on human red cell membranes and the interfacial phospholipid pressure in monolayers. *Biochimica et Biophysica Acta (BBA)-Biomembranes* **406**, 97-107 (1975).
43 Israelachvili, J. Thin film studies using multiple-beam interferometry. *Journal of Colloid and Interface Science* **44**, 259-272 (1973).
44 Israelachvili, J. N. & Adams, G. E. Measurement of forces between two mica surfaces in aqueous electrolyte solutions in the range 0–100 nm. *Journal of the Chemical Society, Faraday Transactions 1: Physical Chemistry in Condensed Phases* **74**, 975-1001 (1978).
45 Israelachvili, J. N. & McGuiggan, P. M. Forces between surfaces in liquids. *Science* **241**, 795-800 (1988).
46 Israelachvili, J. Direct measurements of forces between surfaces in liquids at the molecular level. *Proceedings of the National Academy of Sciences of the United States of America* **84**, 4722 (1987).
47 Tristram-Nagle, S., Liu, Y., Legleiter, J. & Nagle, J. F. Structure of gel phase DMPC determined by X-ray diffraction. *Biophysical journal* **83**, 3324-3335 (2002).
48 Petrache, H. I. *et al.* Structure and fluctuations of charged phosphatidylserine bilayers in the absence of salt. *Biophysical journal* **86**, 1574-1586 (2004).
49 Pan, J. *et al.* Molecular structures of fluid phase phosphatidylglycerol bilayers as determined by small angle neutron and X-ray scattering. *Biochimica et Biophysica Acta (BBA)-Biomembranes* **1818**, 2135-2148 (2012).
50 Kučerka, N. *et al.* Structure of fully hydrated fluid phase DMPC and DLPC lipid bilayers using X-ray scattering from oriented multilamellar arrays and from unilamellar vesicles. *Biophysical journal* **88**, 2626-2637 (2005).
51 Disalvo, E. *et al.* Structural and functional properties of hydration and confined water in membrane interfaces. *Biochimica et Biophysica Acta (BBA)-Biomembranes* **1778**, 2655-2670 (2008).
52 Cowley, A. C., Fuller, N., Rand, R. & Parsegian, V. Measurement of repulsive forces between charged phospholipid bilayers. *Biochemistry* **17**, 3163-3168 (1978).
53 Ohki, S. & Kurland, R. Surface potential of phosphatidylserine monolayers II. Divalent and monovalent ion binding. *Biochimica et Biophysica Acta (BBA)-Biomembranes* **645**, 170-176 (1981).
54 Tsui, F. C., Ojcius, D. M. & Hubbell, W. L. The intrinsic pKa values for phosphatidylserine and phosphatidylethanolamine in phosphatidylcholine host bilayers. *Biophysical journal* **49**, 459-468 (1986).
55 Helm, C. A., Laxhuber, L., Lösche, M. & Möhwald, H. Electrostatic interactions in phospholipid membranes I: Influence of monovalent ions. *Colloid and Polymer Science* **264**, 46-55 (1986).
56 Sathappa, M. & Alder, N. N. The ionization properties of cardiolipin and its variants in model bilayers. *Biochimica et Biophysica Acta (BBA)-Biomembranes* **1858**, 1362-1372 (2016).

57 Manning, G. S. Counterion condensation on charged spheres, cylinders, and planes. *The Journal of Physical Chemistry B* **111**, 8554-8559 (2007).
58 Kurniawan, J., Suga, K. & Kuhl, T. L. Interaction forces and membrane charge tunability: oleic acid containing membranes in different pH conditions. *Biochimica et Biophysica Acta (BBA)-Biomembranes* **1859**, 211-217 (2017).
59 Sacre, M. & Tocanne, J. Importance of glycerol and fatty acid residues on the ionic properties of phosphatidylglycerols at the air—water interface. *Chemistry and physics of lipids* **18**, 334-354 (1977).
60 Dreier, L. B. *et al.* Saturation of charge-induced water alignment at model membrane surfaces. *Science advances* **4**, eaap7415 (2018).
61 Eisenberg, M., Gresalfi, T., Riccio, T. & McLaughlin, S. Adsorption of monovalent cations to bilayer membranes containing negative phospholipids. *Biochemistry* **18**, 5213-5223 (1979).

4.7 Supporting Information

Section S1: Lipid monolayer surface pressure-area (Π–A) isotherms.

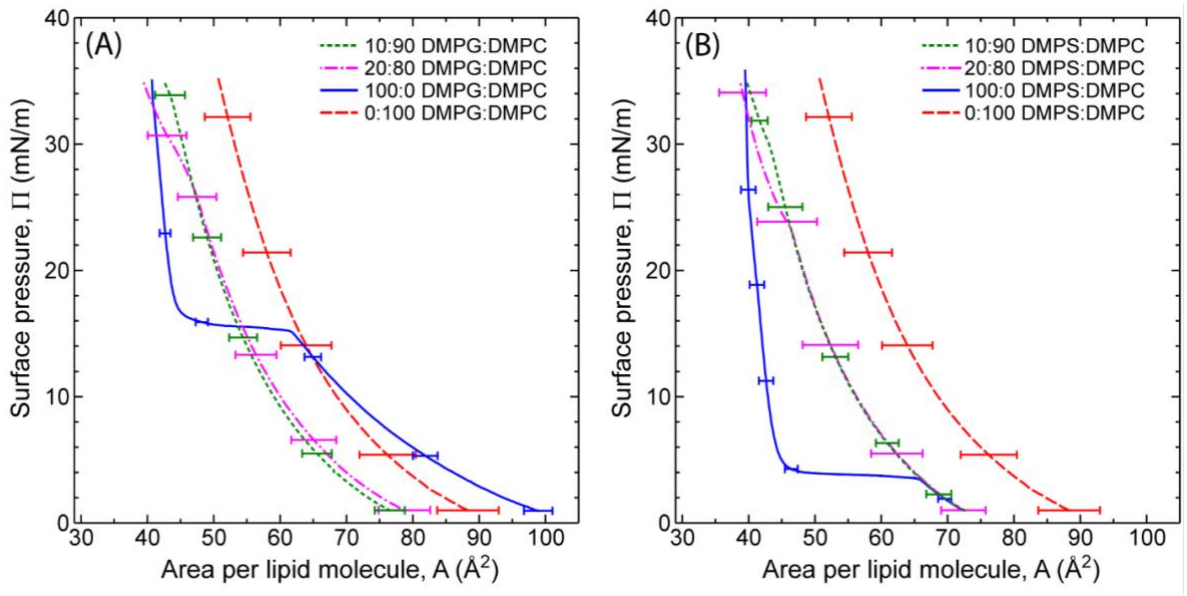

Figure S1: Pressure vs. area (Π–A) isotherm curves for different compositions of (A) DMPG:DMPC and (B) DMPS:DMPC monolayers at the air-water interface, at room temperature (24.5 ± 1.0 °C) on subphase of milliQ water. Selected error bars shown are ±1 standard deviation.

Lipid monolayers were prepared by spreading the desired lipid solution at the air-water interface on a Langmuir Blodgett Trough. The solvent was allowed to evaporate for 10 minutes, after which the lipids were compressed at a constant rate of 20 cm^2/min. To check reproducibility, experiments

were performed with three independent mixtures made from separate stock solutions of lipids. The isotherms shown represent one set of experimental data with selected error bars. **Figure S1** shows the Π–A isotherms for lipid monolayers composed of different lipid mixtures - 10:90, 20:80, 100:0 DMPG:DMPC or DMPS:DMPC at the air-water interface. The isotherms indicate that while pure (single component) DMPC is in the fluid phase, pure DMPS and pure DMPG monolayers are in the gel phase at 35 mN/m. For mixed lipid compositions, the curves indicate that the monolayers are in the fluid phase - gel phase coexistence regime. Upon transfer to a DPPE monolayer-coated mica substrate, these mixed lipid monolayers (outer leaflet) are expected to be in the gel phase. The average molecular area for the compositions used in SFA experiments is between 42 – 45 $Å^2$ per lipid (at 35mN/m).

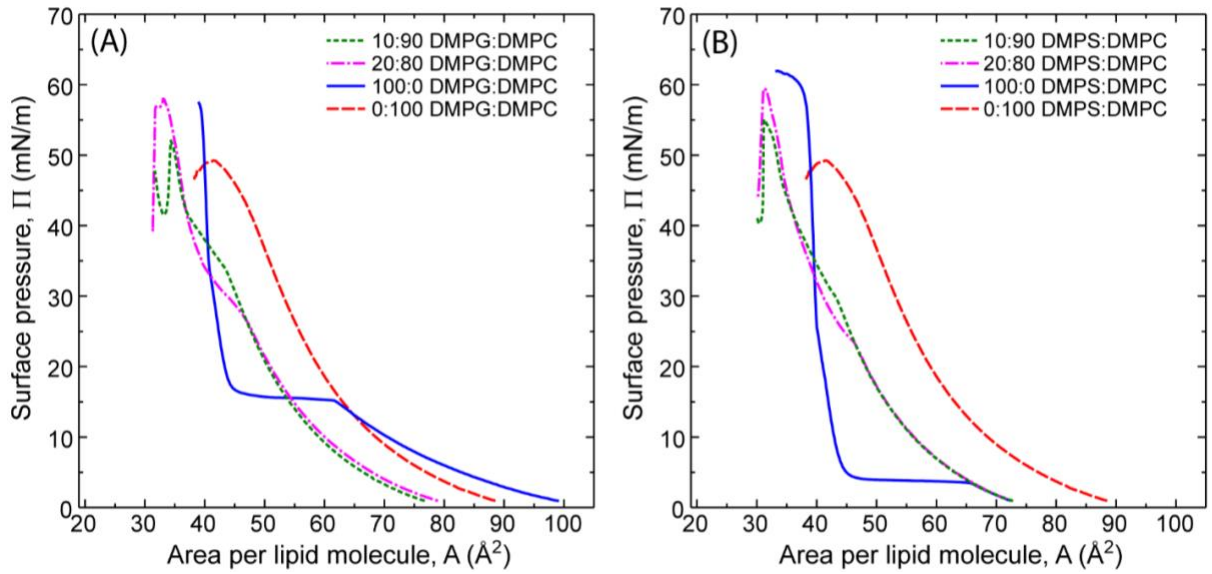

Figure S2: Pressure vs. area (Π–A) isotherm curves to collapse for difference compositions of mixed (A) DMPG: DMPC and (B) DMPS: DMPC monolayers at the air-water interface, at room temperature (24.5 ± 1.0 °C) on a subphase of milliQ water.

Figure S2 shows the Π–A isotherms to collapse for lipid monolayers composed of different lipid mixtures 10:90, 20:80, 100:0 DMPG:DMPC or DMPS:DMPC at the air water interface. The collapse pressure of pure (single component) lipid monolayers was found to be around 48 ± 2

mN/m for DMPC, 60 ± 3 mN/m for DMPS, and 58 ± 3 mN/m for DMPG. For the lipid mixtures containing 10 or 20 mol% DMPS/DMPG, the curves indicate a single collapse peak with collapse pressures between those for pure DMPC and pure DMPS/DMPG indicating that the lipids were well mixed. However, phase separation was observed by fluorescence microscopy as shown in **Figure S3.**

Section S3: Vesicle size measurements (DLS)

Table S1: Size measurements of vesicles in 140 mM phosphate buffer, pH 7.4.

DMPS:DMPC	**Diameter (nm)**
0:100	171 ± 80
0.1:99.9	137 ± 26
0.5:99.5	158 ± 51
1:99	194 ± 27
5:95	165 ± 34
10:90	150 ± 31
20:80	148 ± 32
30:70	141 ± 24
100:0	152 ± 66
DMPG:DMPC	**Diameter (nm)**
0.1:99.9	172 ± 47
0.5:99.5	169 ± 32
1:99	149 ± 26
5:95	152 ± 29
10:90	166 ± 48
20:80	146 ± 35
30:70	144 ± 37
50:50	150 ± 36
100:0	128 ± 39

Table S2: Size measurements of vesicles in 0.5 mM NaNO3, 5.7.

DMPS:DMPC	**diameter (nm)**
0.5:99.5	104 ± 68
1:99	106 ± 67
10:90	97± 57
20:80	160 ± 51
100:0	151 ± 50
DMPG:DMPC	**diameter (nm)**
0.5:99.5	161 ± 97
2:98	173 ± 64
10:90	134 ± 61
100:0	182 ± 71

Section S2: Fluorescence Microscopy of supported lipid bilayers.

Fluorescence microscopy images were acquired using a Nikon Eclipse E600 optical microscope connected to an Andor Zyla sCMOS camera using a 40× magnification water-immersion objective lens. 5 mol% fluorescent dye-labelled Texas Red-DHPE lipid was incorporated into lipid bilayers of different compositions used in this work to help visualize the membrane.

Figure S3 shows fluorescence microscopy images of various compositions of lipid bilayers deposited onto freshly-cleaved mica using the Langmuir Blodgett technique. The inner leaflet of the lipid bilayers was DPPE deposited on mica at 45 mN/m, the outer leaflet (compositions indicated in figure labels, containing 5 mol% fluorescently labelled Texas Red-DHPE) was deposited onto DPPE-coated mica at 35 mN/m. The deposition speed was 1mm/min for both inner and outer leaflets. Texas Red-DHPE is known to partition in to the fluid phase due to the bulky

fluorescent-label bearing lipid head group.[1] Bilayers composed of mixed DMPG:DMPC or DMPS: DMPC outer leaflets shown in figure S3 (A, B, D, E), show both fluorescent and dark regimes in varying proportion suggesting that there was fluid phase and gel phase coexistence. Subsequent fluorescence recovery after photobleaching (FRAP) experiments on these bilayers (not shown) did not show fluorescence recovery, suggesting that these bilayers behave largely like gel-phase systems. From the Π–A isotherms it is clear that pure DMPG and DMPS bilayers are expected to be in the gel phase. This is confirmed by figure S3 (C, F) in which we observe large 50-70μm sized dark patches from which the fluorescently labelled lipid is being excluded to the edges due to steric effects.

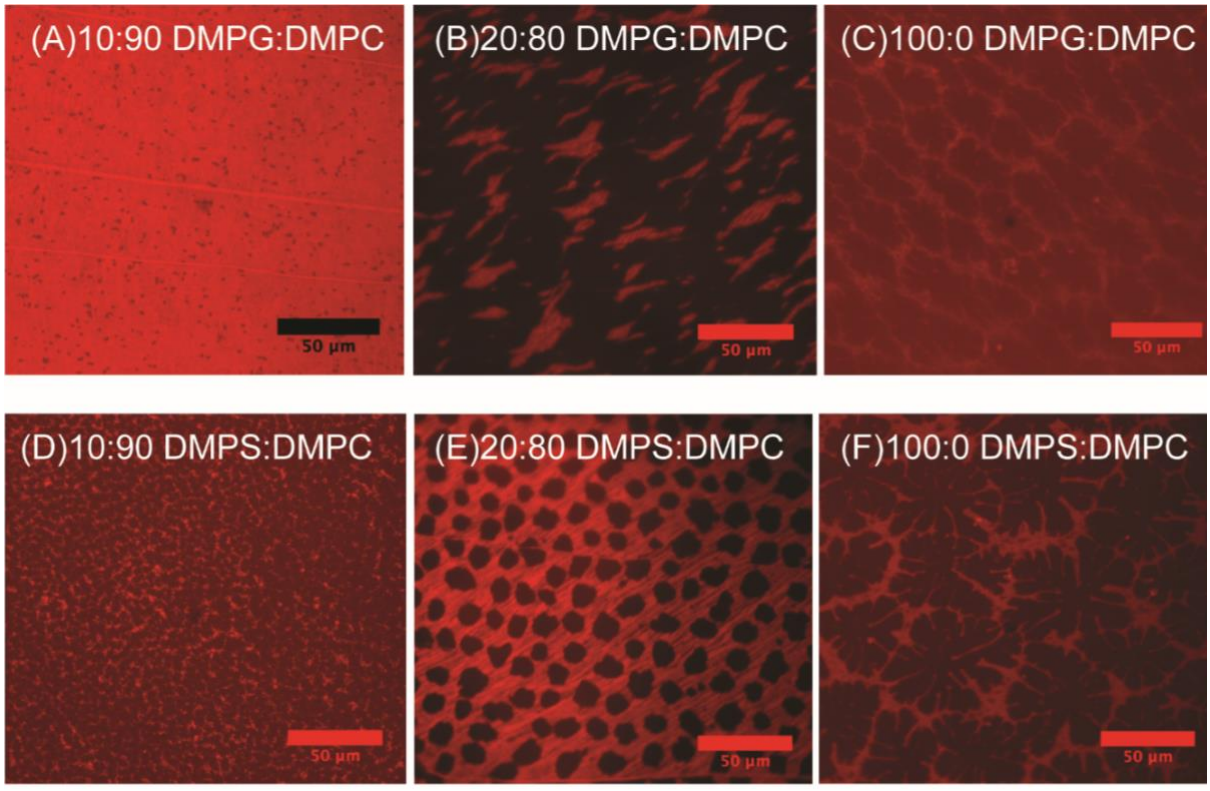

Figure S3: Fluorescence microscopy images of mixed DMPG: DMPC (A-C) and DMPS: DMPC (D-F) supported lipid bilayers on mica. The bilayers contain 5 mol% fluorescently labelled Texas Red-DHPE lipid. Scale bars are 50 μm.

Section S4: SFA force/radius vs. distance profiles for all lipid bilayer compositions.

Figure S4 shows the interaction force profiles for all lipid bilayer compositions (10:90, 20:80, 100:0 DMPG:DMPC or DMPS:DMPC) measured by SFA. Table S1 summarizes the values of surface charge, potential, effective area per dissociated charged lipid, and percentage ionization. Error is one standard deviation based on three independent SFA measurements for each composition.

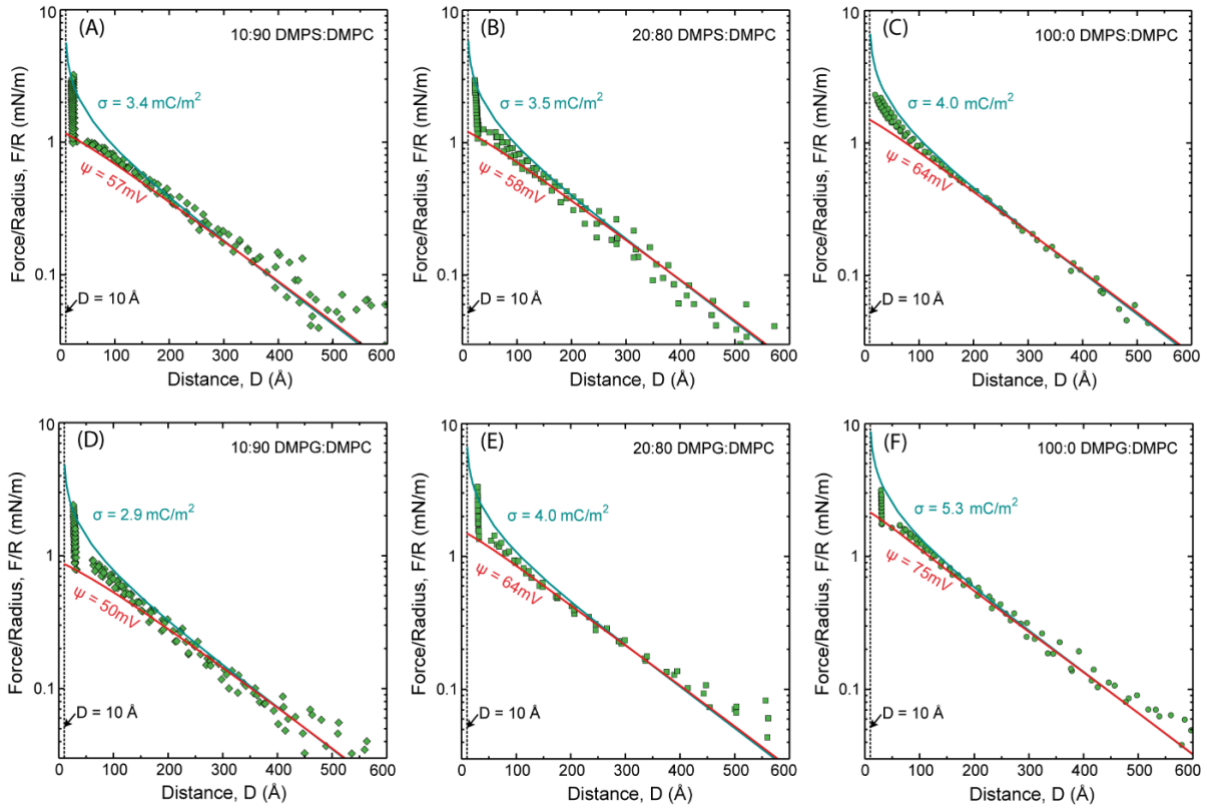

Figure S4: Measured force profiles between lipid bilayers composed of 10:90, 20:80, 100:0 DMPG:DMPC or DMPS:DMPC (outer leaflet) deposited on DPPE (inner leaflet) in 0.5 mM $NaNO_3$, pH 5.7, T= 25.0 °C) on a semi-logarithmic plot. D = 0 Å was defined as anhydrous bilayer contact which corresponds to the location of the phosphate head group plane. The plane of origin of charge was set at D = 10 Å.

Section S5: Plane of origin of charge analysis for SFA experiments.

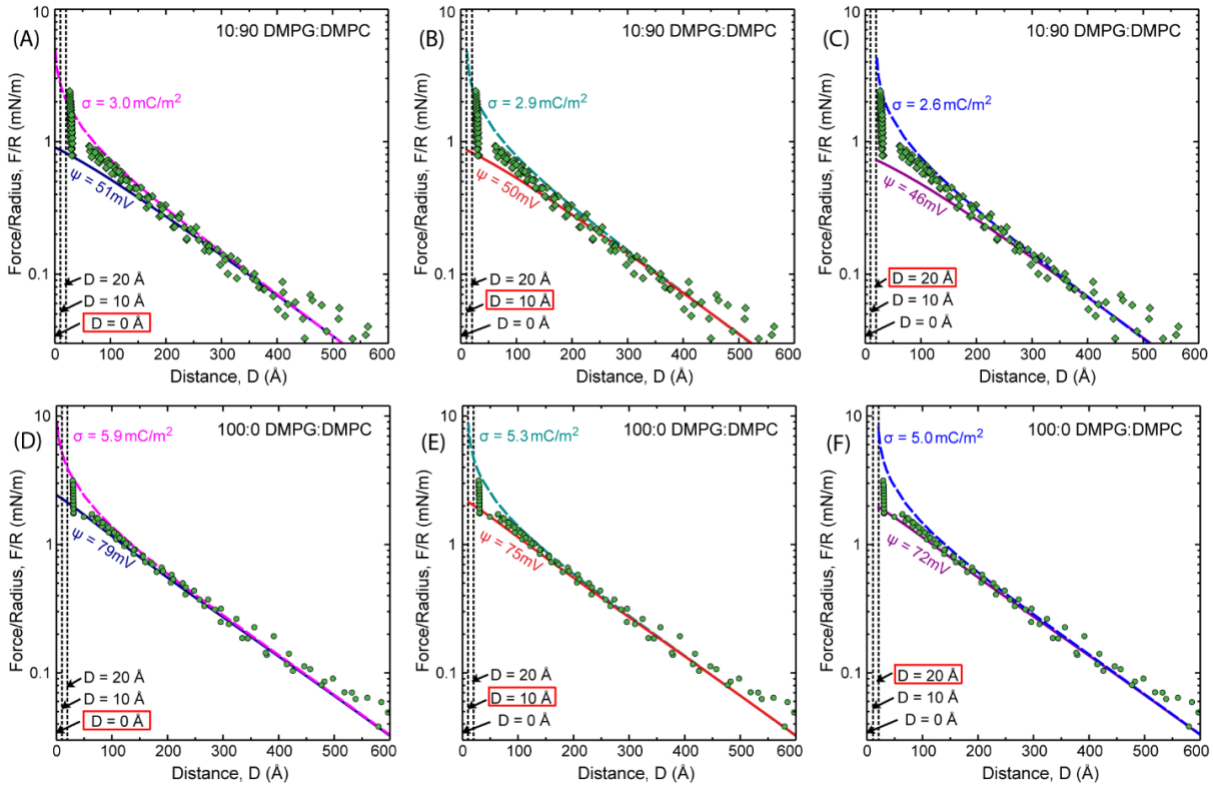

Figure S5: Measured force/radius vs distance profile between lipid bilayers composed of 10:90 DMPG:DMPC (A-C), and 100:0 DMPG:DMPC (D-F) deposited on DPPE (inner leaflet) in 0.5mM $NaNO_3$ (pH 5.7, 25.0 °C) on a semi-logarithmic plot. The assumption for plane of origin of charge is varied between D = 0, 10 and 20 Å (as indicated on the graph) and the surface charge and potential were fit using the non-linear Poisson Boltzmann equation.

The soft, fluid nature of lipid bilayers complicates an exact/absolute definition of charge origin due to membrane undulations, the ability of water molecules and counterions to penetrate and adsorb at the membrane interface, and capacity for lipid membrane reorganization. Through this analysis we have covered the most relevant/possible planes of charge origin. D = 0 Å corresponds to contact between the anhydrous lipid bilayers (without hydration) and is the approximate location of the phosphate head group plane that bears ionizable moieties. A surface separation of D = 10 Å (5 Å away from each surface) corresponds to contact between the two bilayer stern layers (the location of the outer Helmholtz plane from which the diffuse layer originates). D = 20 Å

corresponds approximately with the hydrated bilayer contact around which hydration forces begin to dominate over electrostatic repulsion forces.

Figure S5 shows the range of charge and potential values obtained when the three aforementioned charge planes of origin are used for fitting/interpreting electrostatic forces measured between lipid bilayers using the SFA. The electrostatic forces (or energies) predicted by solutions of the non-linear Poisson Boltzmann equation based on constant charge or constant potential boundary conditions are in good agreement with each other at large surface separations (greater than 200 - 300 Å) but start to deviate at smaller surface separations. The experimentally measured forces lie between the two fits indicating that the surfaces exhibit charge regulation behavior.[2] Different assumptions result in a deviation of ± 0.5 mC/m^2 in charge or ± 5 mV in potential which is comparable to the standard deviation of the experiments. At low salt conditions (0.5 mM salt, κ^{-1} ~135 Å), the different charge plane of origin do not result in significant differences in surface potential values and are consistent with zeta potential measurements.

SI References

1 Skaug, M. J., Longo, M. L. & Faller, R. The impact of Texas Red on lipid bilayer properties. *The Journal of Physical Chemistry B* **115**, 8500-8505 (2011).

2 Grabbe, A. Double layer interactions between silylated silica surfaces. *Langmuir* **9**, 797-801 (1993).